Effect of Nasal High Flow Therapy on Work of Breathing and CO_2 Tension

Using an In Vitro and Mathematical Modelling Approach

Cletus Fiifi Adams

Department of Mechanical Engineering

University of Canterbury

This dissertation is submitted for the degree of

Doctor of Philosophy

University of Canterbury November 2017

This Thesis is Dedicated to the Hearts whose Love Peace and Harmony I AM

Acknowledgements

I thank Dr. Mark Jermy for all the encouragement, insightful suggestions, patience and instruction in contribution to the present work. Your impact on me in terms of professional development has been profound. Whenever possible, I am happy to be your student again. I am thankful to my co-supervisors Dr. Patrick Geoghegan and Dr. Callum Spence for your wonderful support. It is very much appreciated.

I am grateful for the technical support received from Gerry Kirk, Garry Cotton, Eric Cox, Kenneth Brown, Scott Amies, Julian Phillips, Julian Murphy and all other members of the technical staff. Beyond academic work, your input into my personal development, has made a great difference, Gerry Kirk.

I am very grateful to my beloved sister Delfynna Adams and grand mother, Emma Azasu, for all the love and support received from your wonderful hearts. Great thanks to the great friends and colleagues who have made staying in New Zealand enjoyable. You will always be remembered.

I would like to thank University of Canterbury for providing financial assistance (UC Doctoral Scholarship) and a conducive environment for studies. A special thanks to Fisher & Paykel Healthcare for the great support received in regards to this work.

Abstract

A breathing therapy is a technique (invasive or non-invasive) that improves respiration. Nasal high flow (NHF) is a relatively new breathing therapy which involves the delivery of humidified and warmed air via a nasal cannula at a constant flow rate (up to 60 L/min). Conditions alleviated with NHF include sleep apnea, hypercapnic respiratory failure and hypoxemic respiratory failure. The proposed mechanisms of action of NHF include improvement in oxygenation; attenuation of inspiratory resistance; generation of positive airway pressure; and reduction in work of breathing (WOB) (energy expended by the respiratory muscles during breathing). This work was motivated by the scarce data on the effect of NHF on work of breathing and gas exchange. Models of the upper airways of an adult and neonate were 3D printed. A physiologically realistic breathing flow was driven through the models (with a piston pump) along with the recording of tracheal pressure (with and without NHF). Airway resistance (with and without NHF) was defined by the coefficients of a quadratic fit to the tracheal pressure versus breathing flow. This work is the first to estimate airway resistance under NHF conditions in this way. In the adult model, with and without NHF, tracheal pressure during mouth closed breathing was 3 times that of mouth open breathing. Airway resistance increased in an NHF-dependent manner in both breathing directions (inspiration and expiration) and both mouth states of breathing (mouth open and mouth closed). At peak breathing flows of 30 L/min (for the adult model) and 5 L/min (for the neonate model), the neonatal airway resistance was found to be 4 times that of the adult model. The increased pressures generated by mouth closed breathing suggests that the efficacy of NHF at preventing lung collapse (atelectasis) may be improved via closed mouth breathing. A

mathematical model for WOB (based on the Otis equation, which uses the experimentally measured airway resistance) was developed by taking into account reported NHF-induced physiological changes in minute volume and I:E ratio. WOB per minute (rWOB/min) during NHF was greater than without NHF, if minute volume did not change with NHF. A fall in minute volume by 40 % reduced rWOB/min by 90 % (at NHF of 60 L/min) compared to a no NHF condition. NHF can drive part or all of the inspiratory breathing flow across the upper airway and produce a fall in inspiratory rWOB/min. The rWOB/min for mouth closed breathing was 3 times that of mouth open breathing assuming equal fall in minute volume. The adult rWOB/min was found to be 16 times that of the neonate. The effect of NHF on alveolar CO_2 tension was estimated by metering CO_2 at a specific rate into the piston pump chamber and recording tracheal CO_2 tension during breathing, with and without NHF. Apnea was simulated by intermittently stopping the breathing flow for a definite time. End-tidal CO_2 concentration ($EtCO_2$) reduced with NHF and reached a plateau at NHF of 40 L/min. Compared to breathing without NHF, 40 L/min of NHF reduced the maximum end-tidal CO_2 by 18 %, which suggests a lowering of alveolar CO_2 tension and rWOB/min (via attenuation of hyperventilation). It is speculated that NHF may ameliorate the frequency of apnea per hour. A two compartment (lung and dead space) mathematical model of the respiratory system was developed to predict $EtCO_2$ tension during apnea under NHF conditions. The model assumed a sinusoidal breathing flow, constant metabolic CO_2 production, instantaneous gas mixing and flushing of the nasopharynx by 3 % of NHF. Apnea was modelled by making the breathing flow zero over a definite time. The model capnogram and $EtCO_2$ for apnea, spontaneous breathing and NHF matched those of the bench-top experiment. The $EtCO_2$ at NHF of 30 L/min differed from that of experiment by 0.9 % (V/V).

Publications arising from this research

- **Published**
  - S.C Van Hove, J. Storey, **C. Adams**, K. Dey, P. H. Geoghegan, N. Kabaliuk, C.J.T Spence, M.C. Jermy, V. Suresh, and J.E. Cater. "An experimental and numerical investigation of CO_2 distribution in the upper airways during nasal high flow therapy". *Annals of biomedical engineering* 44.10 (2016):3007-3019
- **In preparation**
  - **Cletus F. Adams**, Patrick H. Geoghegan, Callum J. Spence, Mark C. Jermy. ”In vitro modelling of the effect of nasal high flow therapy on tracheal CO_2 tension during episodes of apnea"
  - **Cletus F. Adams**, Patrick H. Geoghegan, Callum J. Spence, Mark C. Jermy. "Model studies on the effect of variation in the breathing flow pattern in COPD patients on end-tidal CO_2 tension"
- **In Review**
  - **Cletus F. Adams**, Patrick H. Geoghegan, Callum J. Spence, Mark C. Jermy. "Effect of nasal high flow therapy on upper airway resistance and work of breathing". *Submitted to Annals of Biomedical Engineering Journal*
- **Conference Proceedings**
  - Marcin Buchajczyk, Patrick Geoghegan, Natalia Kabaliuk, **Cletus Adams**, Mark Jermy, Callum Spence. ”Experimental Investigation of Airway Pressures on Human Airway Models with Compliant Components”. *Australasian Fluid Mechanics Conference*, Dec. 2016.
  - **C.F. Adams**, M.C Jermy, P.H Geoghegan, Callum Spence. "Effect of Nasal High Flow Therapy on Airway Resistance". *Fluids in New Zealand*, Feb. 2017.

- **C.F. Adams**, M.C Jermy, P.H Geoghegan, Callum Spence. "Effect of Nasal High Flow Therapy on CO2 Tension – Physico-mathematical Modelling". *Eigth International Conference on Bioinformatics, Biocomputational Systems and Biotechnology*, Lisbon, Portugal, June 2016.
- **C.F. Adams**, M.C Jermy, P.H Geoghegan, Callum Spence. "Effect of Nasal High Flow Therapy on Work of Breathing and CO_2 Flushing: Physico-mathematical Modelling". *Fluids in New Zealand*, Jan. 2016.
- **C.F. Adams**, M.C Jermy, P.H Geoghegan, Callum Spence. "Effect of Nasal High Flow Therapy on Work of Breathing in Adult Lungs". *Fluids in New Zealand*, Jan. 2015.

Table of contents

List of figures

List of tables

Chapter 1

Introduction

For inspiration to occur, the diaphragm and intercostal muscles contract to create a greater intrathoracic volume thereby reducing the pressure in the lungs relative to the airway opening (mouth or nostril). This pressure gradient drives inspiration and carries oxygen into the lung's blood-gas interface where pulmonary blood absorbs the oxygen and gives up carbon dioxide. The mechanical work done by the diaphragm and intercostal muscles together is called mechanical work of breathing (Otis et al. (1950)). There is also some amount of metabolic energy expended in warming the inspired air to normothermia (37 °C) and humidifying it to 100 % relative humidity (Rouadi et al. (1999)) – this constitutes thermal work of breathing. Though work of breathing constitutes a small percentage of the metabolic energy, the respiratory control center changes breathing pattern to minimize this energy (Fincham and Tehrani (1983)). In this study, mechanical work of breathing will be used synonymously with work of breathing.

Respiratory failure results when respiratory injuries or diseases cause the respiratory system to become ineffective at delivering oxygen to the cells (hypoxemic respiratory failure) or expelling carbon dioxide from the lungs (hypercapnic respiratory failure). Consequently, respiratory assistance such as low flow oxygen therapy (administered gas flow rate is less than inspiratory demand) (Cairo (1999)), humidified nasal high flow therapy (flow matches

inspiratory demand), continuous positive airway pressure (boosting airway pressure to keep airway open) or mechanical ventilation (device provides part or all the energy required for breathing) may be recommended to the patient. Major indications necessitating the use of a mechanical ventilator include acute respiratory failure, exacerbation of chronic obstructive pulmonary disease (COPD), coma and neuromuscular disorder (Esteban et al. (2000)) whilst those for continuous positive airway pressure (CPAP) therapy include post-operative pulmonary complications, atelectasis (collapsed alveoli), obstructive sleep apnea (collapse of airway during sleep) and pneumonia (Ferreyra et al. (2008)).

Nasal high flow (NHF) therapy is a relatively new therapeutic modality involving the administration of humidified and warmed air at constant flows up to 60 L/min for adults (Ward (2013)) and 8 L/min for neonates (Manley et al. (2013); Motojima et al. (2016); Ojha et al. (2013)). NHF is delivered via a nasal cannula with nasal prongs that inserts into the nostril without sealing it. NHF is applied continuously and not synchronized with inhalation or exhalation. Since the commencement of its use in the early 2000s amongst the neonatal population, it has seen a broad application and success even in the adult population. Some medical conditions for which NHF is applied include hypoxemic respiratory failure, obstructive sleep apnoea and acute heart failure (Kernick and Magarey (2010); Nishimura (2015)).

In spite of the reported potential and clinical successes of NHF, its mechanisms of actions are not wholly understood (Dysart et al. (2009)). See section 1.4 for a fuller description of the mechanisms of action of NHF. The reports on clinical trials, bench-top and computational modelling involving NHF over half a decade now have lent a good support to the generation of postive airway pressure (Kubicka et al. (2008); Kumar et al. (2015); Locke et al. (1993); McGinley et al. (2007)) and improvement in oxygenation (Frizzola et al. (2011); Maggiore et al. (2014); Roca et al. (2010)).

The motivation for this thesis has been the absence of quantitative data on the extent to which NHF affects work of breathing coupled with the absence of a predictive tool for

estimating the degree to which CO_2 is cleared from the airway upon the administration of NHF. Accordingly, this thesis aims at examining the physical influence of NHF on the mechanical aspects of breathing followed by a quantitative assessment of these effects on metabolic energy cost. These ends have been achieved via in vitro and mathematical modelling.

1.1 Anatomy and Physiology of the Respiratory System

The ventilatory system of humans has two sections i.e. the upper and lower respiratory tracts. The nasal cavity, nasopharynx, oropharynx, hypopharynx (laryngopharynx) and the trachea constitute the upper airway (Fig. 1.1). The trachea divides into two major branches known as bronchi, which further divides into smaller units called bronchioles (Fig. 1.2). There are about twenty-three generations of division from the trachea up to the sac-like structures known as alveoli (Fig. 1.2) (West (2012)).

The lower respiratory tract is subdivided into three zones namely the conductive zone, transition zone and respiratory zone. The bronchi plus the next fifteen generations of the bronchioles form the conducting zone. The seventeenth generation to the nineteenth generation mark the transition zone, which consist of respiratory bronchioles that possess anatomic features to engage in substantial gaseous exchange. Finally, the last four generations constitute the respiratory zone - the first three being alveolar ducts and the very last generation being alveolar sacs (Fig. 1.2). There are about 300 to 500 million alveoli in the human lungs having a combined surface area in the range of 50 - 100 square meters (approximately equal to one-half the size of a tennis court) (Tsuda et al. (2008); West (2012)). The alveolar wall is replete with a network of pulmonary capillaries (7 - 10 μm in diameter). The blood-gas barrier is approximately 0.3 μm thick (West (2012)). Gaseous exchange across the blood-gas interface is significantly enhanced by the large surface area of the alveoli and the very thin epithelia lining it. A lipoprotein complex, surfactant, secreted by type II cells lining the

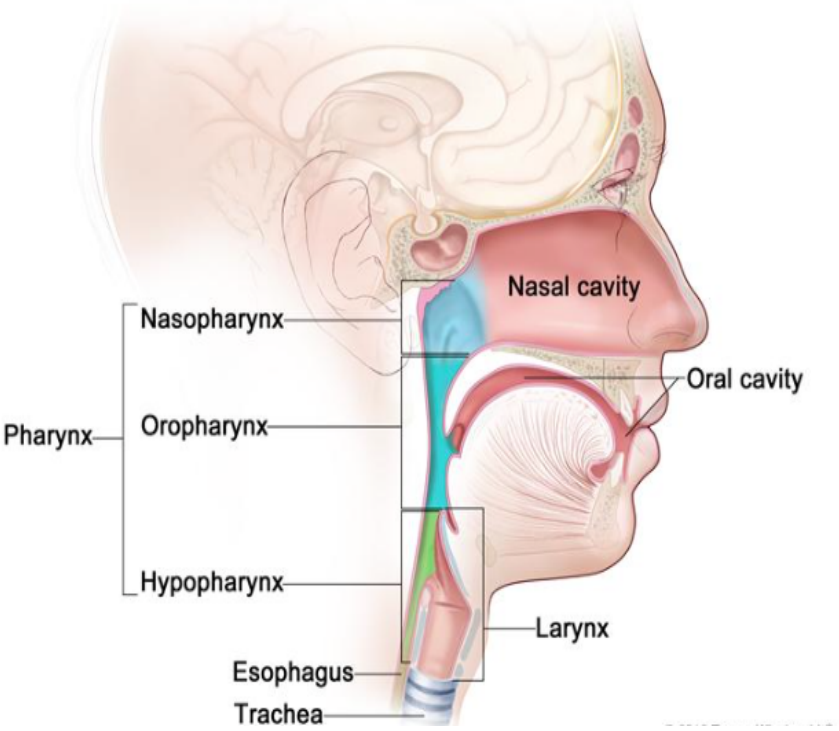

Fig. 1.1 Upper airway (adapted from http://www.pittsburghdentalsleepmedicine.com)

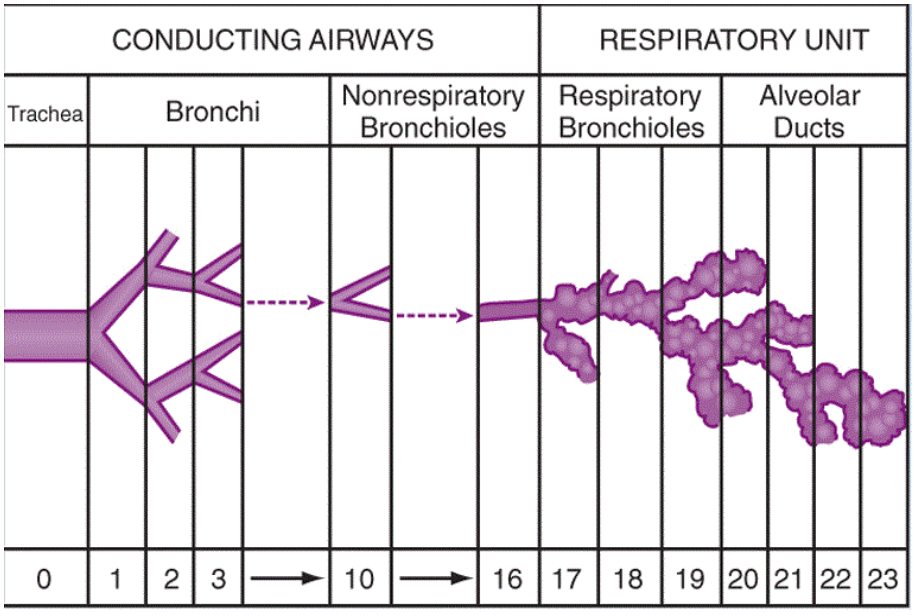

Fig. 1.2 Lower airway generations (adapted from http://users.atw.hu)

alveoli maintains stability of the millions of alveoli by preventing them from completely collapsing. The hydrophilic heads of the lipoprotein complex are radially oriented and bonded to the inner lining of the alveoli, with the hydrophobic tails repelling each other (Johansson et al. (1994); West (2012)). The elastic recoil of the alveoli is opposed by this repulsive force and this serves to reduce respiratory effort as a relatively small amount of work is required to inflate the alveolar sac in this condition. To further enhance efficiency of gaseous exchange, each red blood cell has a residence time of 0.75 seconds and traverses about three alveoli before exiting the capillary network (Johansson et al. (1994)).

Together, the alveoli, conducting airways and associated blood vessels comprise the lungs. The lungs are encased in a thin two-layer membrane (pulmonary pleurae) envelope which forms the pleural space (Fig. 1.3). The right lung is compartmentalized into three lobes whilst the left is made up of two lobes as shown in Fig. 1.3. Total lung capacity, defined as the volume of air that the lungs can be filled with, varies with body size but has an average value of 7 litres for healthy adults (Tobin et al. (1983)).

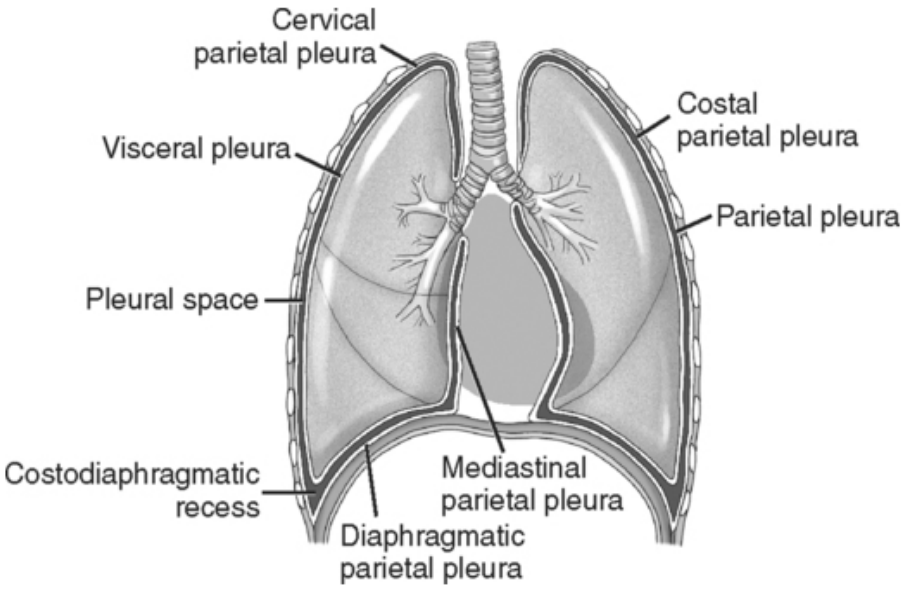

Fig. 1.3 The lungs (adapted from https://basicmedicalkey.com)

There are five other lung volumes namely tidal volume, inspiratory reserve volume, expiratory reserve volume, functional residual capacity and residual volume. Tidal volume

is the volume of air inspired during spontaneous breathing (see Fig. 1.4). The volume of air that can be further inspired after spontaneous inspiration is called inspiratory reserve volume. The volume of air remaining in the lungs after spontaneous expiration defines the functional residual capacity. Following spontaneous expiration, the extra volume of air that can be expired is known as expiratory reserve volume. The volume of air that remains in the lung irrespective of how hard one expires is known as the residual volume (Fig. 1.4). During ventilation, the lungs get periodically inflated and deflated (constituting one cycle) and the number of cycles per minute is known as respiratory rate. The product of respiratory rate and tidal volume defines another parameter known as minute ventilation, which is the total volume of air inspired in a minute. See Fig. 1.4 for the relationships between the lung volumes.

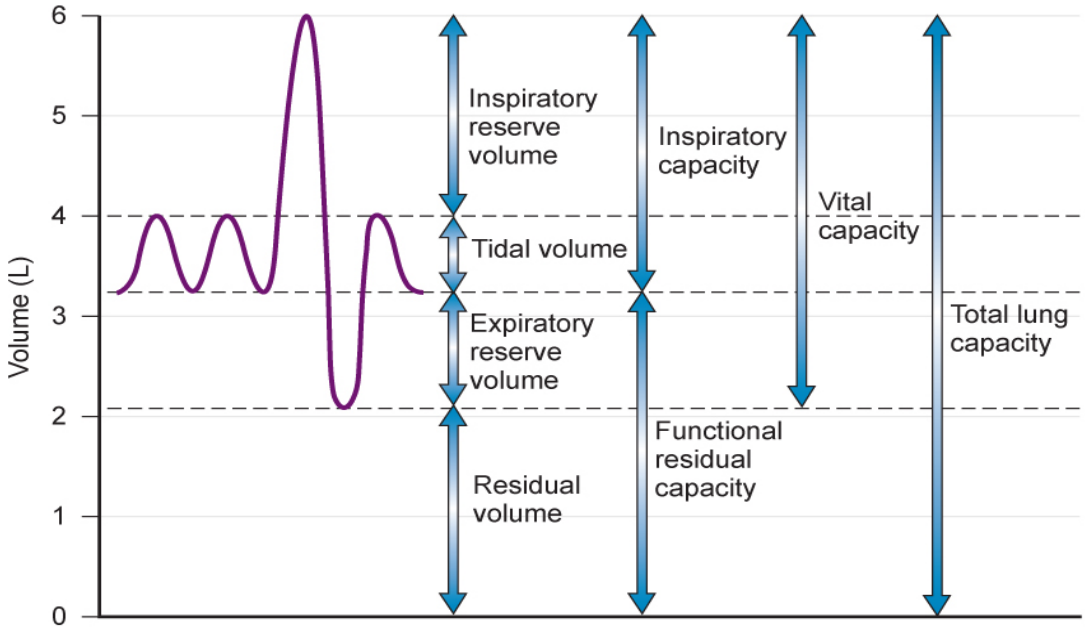

Fig. 1.4 Lung volumes (adapted from http://www.clevelandclinicmeded.com)

1.1.1 Driving forces in breathing

In respiratory physiology, atmospheric pressure is the conventional datum (i.e. zero) and alveolar pressure equals the atmospheric at the end of expiration. The pressure within the

pleural cavity is known as intrapleural pressure and varies with position. For instance, it may have a value of -5 cmH_2O at the apical portions of the lungs and approximately -3 cmH_2O at the basal portions. This disparity originates from the pressure exerted by the weight of the lungs on the basal portions (Galvin et al. (2007); West (2012)). The trans-chest wall pressure is the differential pressure between the pleural cavity and the outer surface of the chest (atmosphere) whilst the transmural pressure is the difference in pressure between alveolar space and the pleural cavity. The intrapleural pressure is driven by intercostal and diaphragmatic muscular effort, which in turn drives inspiration. At the onset of expiration, elastic recoil forces generated by the lungs increase alveolar pressure relative to atmospheric pressure and expels air out of the lungs. Fig. 1.5 shows the variation of intrapleural pressure, alveolar pressure and lung volume during one cycle of breathing (obtained via mathematical modelling, Chapter 8).

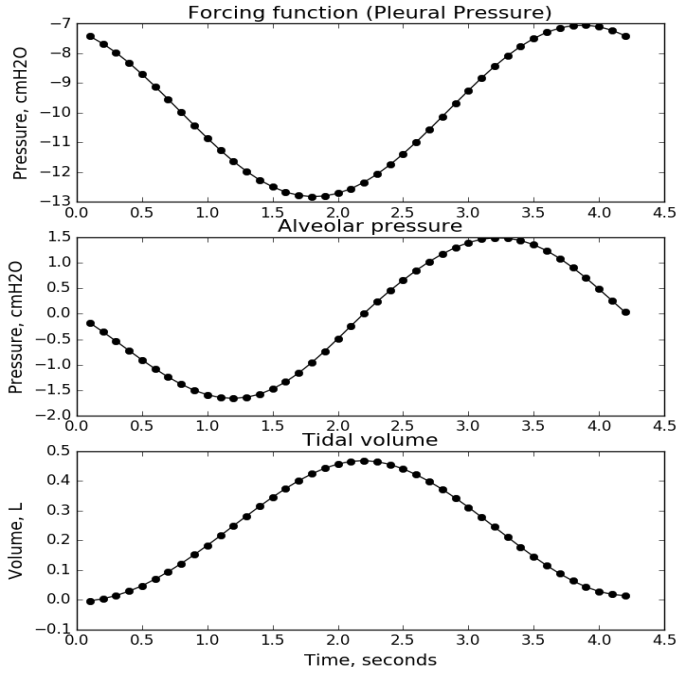

Fig. 1.5 Cycle variation for alveolar pressure, intrapleural pressure and tidal volume

1.2 Respiratory Diseases

Living organisms survive by metabolizing food substances to release energy. Central to the metabolic process is oxygen, which is taken from the organism's surrounding. The process by which air enters and exits the lungs is known as breathing or ventilation. Respiration refers to gaseous exchange via a membrane interface. External respiration refers to gaseous exchange between the air and the blood stream across the alveolar walls whilst internal respiration refers to gaseous exchange between the blood stream and body cells across the interstitial spaces. The respiratory system can be impaired by congenital and acquired diseases, which in some cases markedly reduce its gaseous exchange capability. Disorders of the respiratory system can be classified according to etiology, severity, duration (chronic or acute), affected regions, mode of acquisition, etc. Respiratory disorders can loosely be classified into four categories (Tocris (2017)) namely:

- Obstructive diseases (those that impair expiration) - examples include emphysema, chronic bronchitis, asthma
- Restrictive diseases (those that impair inspiration) - examples include pulmonary fibrosis, pleural effusion, sarcoidosis
- Pulmonary vascular diseases: examples include pulmonary edema, pulmonary embolism
- Infectious and occupational diseases: examples include pneumonia, tuberculosis, asbestosis, byssinosis

The mortality rate and economic impact of COPD and asthma are one motivation for this work. The present work contributes to the global effort of mitigating the mortality rate of COPD and asthma. The pathogenesis, prevalence and mortality rate of COPD and asthma are reviewed in the following subsections.

1.2.1 Pathophysiology of chronic obstructive respiratory disease

Chronic obstructive pulmonary disease (COPD) is the general term used for chronic bronchitis and emphysema. Inflammatory cells in the human body respond to triggering factors such as toxins in tobacco, indoor pollutants, occupational dusts and industrial fumes. Prominent among these cells are neutrophils, macrophages and lymphocytes. When activated by the mentioned risk factors, these cells synthesize a battery of inflammatory mediators such as cytokines, chemokines and chemo-attractants which ensure prolonged inflammation (Brashier and Kodgule (2012)). During chronic bronchitis the airways become swollen, accompanied by hyper-secretion of mucus. Emphysema is simply a loss of lung elasticity due to the break down of the elastic fibers that make up the alveoli. It is engendered when inflammatory mediators and cells like neutrophils stimulate the production of proteolytic enzymes such as elastase, proteinase-3 and perforin whose effect include denaturing of elastic fibers and in some cases expediting apoptosis (self-destruction) of alveolar epithelial cells (Brashier and Kodgule (2012)). The denaturing of the elastic fibers causes increased compliance of alveolar sacs and a subsequent retention of inspired air in the lungs (hyperinflation). Depending on the extent of destruction, the alveolar sacs may completely collapse (atelectasis), and this can reduce the amount of exchanged gas. In the end, accumulation of CO_2 leading to respiratory acidosis may ensue (Juan et al. (1984)).

COPD was the fifth leading cause of death as of 2002 and it has been estimated that it will be the third leading cause of mortality worldwide by 2030 (WHO 2017). In New Zealand, COPD is the fourth leading cause of death, attracting $ 192 million in government expenditure by the close of 2002. The cost of respiratory diseases per year in New Zealand as at 2016 has been estimated to be $ 6.16 billion (Telfar and Zhang 2016). In the United States, the cost of COPD in 2010 was $ 50 billion (Guarascio et al. (2013)).

1.2.2 Pathophysiology of asthma

Asthma is a disease associated with variable and recurring airflow obstruction, hyper-responsiveness and inflammation of the bronchioles (National and Prevention (2007)). Asthma can be triggered by allergens linked to substances such as furs and fecal droppings of pets, pesticides, pollen grains of some plants or ligands in some drugs (Agius et al. (1991)). Other conditions such as exercise, pregnancy and menstruation may also trigger asthma. When asthma is triggered, many inflammatory cells including mast cells, eosinophils and T-lymphocytes are released (Barnes (1989); National and Prevention (2007)). Mast cells are mainly involved in acute asthma aggravations whilst macrophages, eosinophils and T-lymphocytes are noted in chronic asthmatic conditions (Barnes (1996)). When these cells are activated, they stimulate the synthesis of protein bodies known as inflammatory mediators, typically cytokines, histamine, leukotrienes and prostaglandins. These mediators initiate events which lead to the contraction of the smooth muscle lining of the airway, hyper-secretion of mucus, increased microvascular leakage and attraction of other inflammatory cells thereby producing the observable symptoms such as labored breathing, shortness of breath and wheezing (Barnes (1996)).

New Zealand is second only to the United Kingdom in terms of asthma prevalence, with one out of every six adults being asthmatic (Menclova and Webb (2016)). Also, asthma is the most common cause of admission to children in New Zealand (Menclova and Webb (2016)). Historically, New Zealand has experienced two episodes of asthma epidemics occurring in the 1960s and 1980s (Pearce and Hensley (1998)). Although the actual number of deaths is not accessible, the recent mortality rate is still significant with 70 deaths (mostly people of age 65 years and more) occurring in 2006 (Telfar and Zhang 2016). In the United Kingdom, asthma and related lung diseases are responsible for about 6.5 % of all hospital admission with 18.3 million work days lost to asthma related problems from 1995 to 1996 (Chung et al. (2002)). Though developing countries contribute the most to global asthma-related deaths, data on economic burden is scarce. A study has however suggested that asthma drugs

cost between 3.8 % and 25 % of a patient's monthly income in 24 developing countries in Asia and Africa (Aït-Khaled et al. (2007)). The World Health Organization report, 2008, suggested that 235 million people worldwide suffer from asthma with about 80 % of all asthma deaths occurring in low and middle income countries and these numbers are estimated to rise in the coming years.

1.3 Breathing Parameters

Biological systems are mostly non-linear systems and are difficult to model accurately without sufficient experimental insight. The measurable respiratory quantities fundamental to this work include airway resistance, airway pressure, and CO_2 concentration profile. The breathing flow pattern may be an input. From these quantities other pertinent parameters such as breathing period, respiratory rate, minute volume, inspiratory to expiratory time fraction (I:E ratio), work of breathing and power of breathing can be estimated.

1.3.1 Breathing flow patterns

The temporal changes in inspired and expired volume over the breathing period constitutes the breathing flow pattern, which may vary in terms of shape, amplitude and period depending age, disease condition and level of activity (exercising or resting). The breathing flow pattern of a 24 year old male adult (Spence (2011); Van Hove et al. (2016)) is shown in Fig. 1.6. From this data, the respiratory rate, tidal volume and I:E ratio can be computed. The area under the inspiratory breathing flow plot represents tidal volume. The volume of inspired air in a minute (minute volume), can be calculated as the product of respiratory rate and tidal volume.

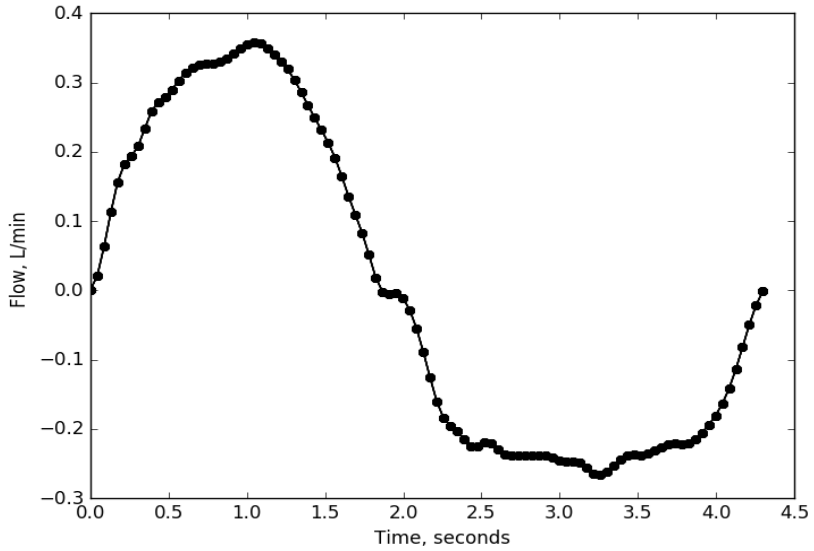

Fig. 1.6 Breathing flow pattern

1.3.2 Airway resistance

Resistance of the airway is a significant parameter that can indicate the difficulty in breathing. It is therefore an important criterion for diagnosing restrictive or obstructive lung diseases and can also be used to evaluate the efficacy of the treatment administered to restrictive or obstructive airway disease patients (DuBois et al. (1956)). A whole body plethysmograph synchronized with a spirometer can be used to acquire breathing flow and alveolar pressure data. The plot of alveolar pressure versus breathing flow yields a non-linear curve (example shown in Fig. 1.7, adapted from Otis et al. (1950)) that can be fitted to a second order polynomial whose coefficients describe the resistance of the airway. The degree of non-linearity of the pressure versus breathing flow curve is often affected by pathological conditions of the extra- and intra- thoracic airway (Verbraak et al. (1991)), thus serving as a good parameter for detection of airway obstruction.

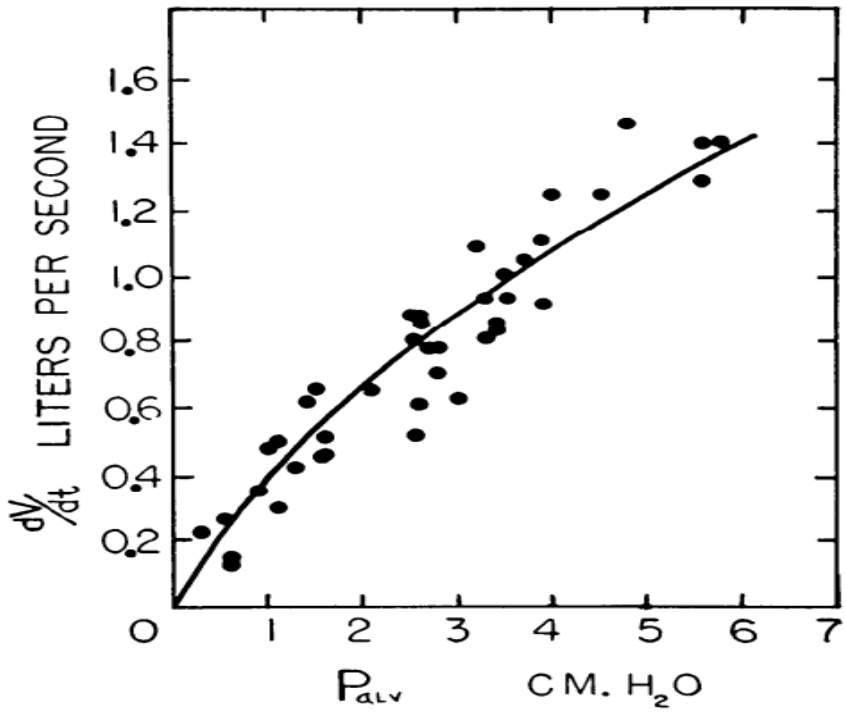

Fig. 1.7 Flow versus alveolar pressure plot for the determination of airway resistance (adapted from Otis et al. (1950))

1.3.3 Work of breathing

The amount of work done by the respiratory muscles in ventilating the lungs is known as mechanical work of breathing. In patients suffering from COPD and asthma, loss of elasticity and increased airway resistance increase work of breathing and produces fatigue which in turn leads to reduced ability to engage in physical exercise (Fleury et al. (1985)). Work of breathing can be used as a metric for evaluating lung performance especially under situations where the patient is recuperating from a diseased state. Clinicians can therefore plan on the possibility of weaning a patient off a respiratory assistive device such as the mechanical ventilator based on work of breathing, amongst other factors (Cabello and Mancebo (2006)). Work of breathing can be estimated using two approaches: firstly, by considering the mechanical work done by the lungs from pressure and volumetric changes during ventilation and secondly, estimation of the amount of oxygen consumed by the respiratory muscles (Brodovsky et al. (1960); Milic-Emili et al. (1999)). Of the two methods, the present study will employ the first approach on the grounds of expediency in collecting clinical data.

1.3.4 Carbon dioxide concentration

The respiratory center, located within the medulla oblongata of the brain performs a homeostatic function to maintain blood acidity within a specific range via cell receptors which are sensitive to variation in blood pH, and CO_2 and O_2 partial pressures (Gray (1951)). It maintains the partial pressure of arterial blood CO_2 in the range of 35 - 45 mmHg (Parot et al. (1980)) by effecting a hormonal response to increase or decrease respiratory rate when CO_2 tension falls out of range. Attendant with some severe forms of COPD is a medical condition known as hypercapnia - a condition where the partial pressure of arterial blood CO_2 is greater than 45 mmHg (Parot et al. (1980)). Higher partial pressure of arterial blood CO_2 may be caused by an increase in CO_2 retention in the lungs often resulting in increased blood acidity (respiratory acidosis) (Dorman et al. (1954)). Respiratory acidosis can cause

poor metabolism leading to fatigue; increased intracranial pressure; lack of alertness; and the patient being comatose.

The CO_2 tension versus time curve, known as a normal capnogram, is shown in Fig. 1.8, adapted from Nagler and Krauss (2009). The normal capnogram has four phases. The starting phase, Phase I (A-B) marks the end of inspiration and commencement of expiration,

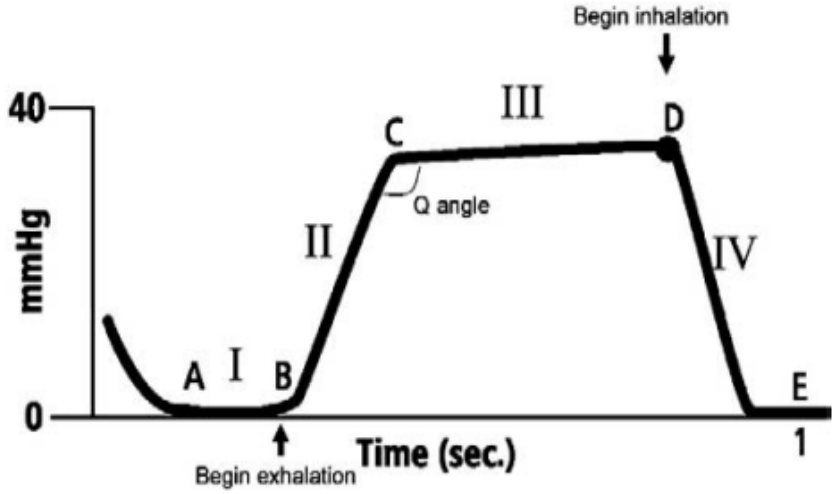

Fig. 1.8 The normal capnogram, adapted from Nagler and Krauss (2009)

during which the dead space air (which has low CO_2 tension) is expelled. This is followed by Phase II (B-C) which involves the fast rise in CO_2 tension as the CO_2-rich alveolar air is expelled. Phase III (CD) indicates an almost complete saturation of the airway with alveolar air and peaks at point D, known as end-tidal CO_2 tension ($EtCO_2$). Inspiration sets in after the $EtCO_2$, where the influx of fresh atmospheric air speedily replaces airway air (Phase IV, D-E)

1.4 Nasal High Flow Therapy

Nasal high flow (NHF) therapy has been used clinically for over a decade (since the early 2000s). It was mainly used in the neonatal population in its early years. More recently, researchers have reported on its efficacy in the management of respiratory failure in chil-

dren and adults. NHF involves the administration of warmed and humidified air at body temperature and saturated pressure i.e. 37 °C and 100 % relative humidity. The purpose of humidification is to prevent changes in the airway squamous epithelium, maintain airway ciliary activity, prevent dehydration and thickening of secretions, and reduce heat loss (Waugh and Granger (2004)). Presently, the maximum therapeutic flow rate is 60 L/min Ward (2013). Dysart et al. (2009) propounded possible mechanisms of action of NHF therapy and these include:

- Improvement in oxygenation
- Attenuation of inspiratory resistance
- Improvement of airway conductance and pulmonary compliance
- Reduction in thermal work of breathing
- Generation of a positive distending pressure

In spite of the reported efficacy of NHF, its mechanisms of action are not altogether understood and evaluation of its effect on breathing parameters have been mostly qualitative. In the next section, a review of the different areas of NHF research is presented along with the research gaps which necessitated the present research work.

1.5 NHF: Application and Research Areas

Clinical research on medical devices serves the health community with new application areas, contraindications of the device, mechanism of action and lastly suggestions for product improvement. Kernick and Magarey (2010) have advised that more insight into the efficacy of NHF can be gained if clinical studies are extended through the entire hospitalization period. A recent review article on NHF by Nishimura (2015) found no reports of contraindications for NHF, and advised on the need to use NHF with circumspection. The author further

suggested that sample size of clinical trials for NHF studies may be increased to raise the statistical and clinical power of findings. The cost of clinical studies is however very costly and for this reason less expensive methods of filling the gaps in literature such as bench-top and computer simulation have been explored in NHF studies, for example the works of Kumar et al. (2015); Mündel et al. (2013); Van Hove et al. (2016) and Spence (2011)

Amongst the proposed mechanisms of actions, the generation of positive airway pressure has received the most attention. Locke et al. (1993) reported on the inadvertent administration of continuous positive airway pressure (CPAP) during the application of high flow oxygen to preterm neonates. As was found for neonates, studies conducted by Groves and Tobin (2007) and Parke et al. (2009) concluded that NHF engendered the same pressure effect in healthy adult population. Recently, Kumar et al. (2015), perhaps for the first time, predicted NHF-induced increase in pharyngeal pressure with a numerical model of the upper airway.

There exists a body of work on the effect of NHF on tidal volume and functional residual capacity (Corley et al. (2011); Mündel et al. (2013); Riera et al. (2013)). Corley et al. (2011) and Riera et al. (2013) used the electrical impedance tomography, which produces cross-sectional images (slices) of tissues noninvasively. They conducted their research amongst a post-cardiac surgery adult population and concluded that NHF gives rise to an increase in functional residual capacity. Riera et al. (2013) concluded that "the application of noninvasive NHF in healthy subjects significantly increases end-expiratory lung impedance (EELI)" - meaning an increment in functional residual capacity. Mündel et al. (2013) using a respiratory impedance plethysmographic band for lung volume measurement concluded that NHF increased tidal volume during wakefulness but reduced it during sleep. Bräunlich et al. (2013) however found a decrease in tidal volume upon administering 30 L/min to 16 awake healthy individuals. The effect of NHF on lung volume therefore varies with wakefulness and disease state.

Another area of research has been the effect of NHF on work breathing. To this end, the work of Saslow et al. (2006) may be regarded as pioneering. In their study, estimates of

intrapleural pressure of neonates (mean age of 26 days and mass of 1118 g) were obtained with esophageal balloon catheter. It was concluded that administration of NHF at flows 3, 4 and 5 L/min to neonates produced work of breathing comparable to the delivery of 6 cmH_2O of CPAP. How the work of breathing during therapy (NHF or CPAP) compared to the work of breathing during spontaneous breathing was not reported. The work of Saslow et al. (2006) was also limited by age group and range of NHF. In a subsequent study, Rubin et al. (2014) conducted their study in an older infant population (age = 1.3 and 15.5 months) and used a wider range of NHF (2 to 8 L/min) compared to Saslow et al. (2006). The product of the esophageal pressure and respiratory rate (pressure-rate-product) or the esophageal pressure and breathing period (pressure-time- product) are surrogates of work of breathing. Collett et al. (1985) found a good correlation between O_2 cost of breathing and the pressure-time product. Rubin et al. (2014) used the pressure-rate product and found a fall in work of breathing with rising NHF. Pham et al. (2014) administered 2L/Kg/min of NHF and measured the esophageal pressure, tidal volume and diaphragmatic electrical activity of 14 infants with bronchiolitis and 14 infants with congenital heart disease. The researchers reported on a decrease in work of breathing with NHF based on reductions in the pressure-rate product and pressure-time product and off-loading of diaphragmatic electrical activity. From the data presented in all three reports (Pham et al. (2014); Rubin et al. (2014); Saslow et al. (2006)) it is concluded that the work of breathing due to NHF is comparable to CPAP and is less than WOB during spontaneous breathing. To date, the only published works that quantitatively examined the effect of NHF on WOB are these three (Pham et al. (2014); Rubin et al. (2014); Saslow et al. (2006)) with none existing for the adult population .

The effect of NHF on gas exchange constitutes another body of research. Flushing of CO_2 from the airway has been suggested as a mechanism of action of NHF but quantitative data has been lacking until recently. Recently, Ritchie et al. (2011) conducted a clinical trial in which a group of 10 healthy adults (mean age of 30.1 years) were administered NHF (titrated to inspired oxygen fraction (FiO2) = 0.6) at flows ranging from 10 to 50 L/min

in steps of 10 L/min. $EtCO_2$ was found to increase by 10 % when NHF was applied over the same range during exercise. Open mouth breathing with NHF was however found to produce a lower (by about 10 %) $EtCO_2$ compared to closed mouth breathing. As suggested by the authors, similar studies conducted amongst individuals suffering from respiratory pathologies such as COPD would be interesting. Möller et al. (2015) filled an anatomically correct upper airway model with a tracer gas (81mKr-gas) and separately administered NHF of 15, 30 and 45 L/min, followed by a CO_2 clearance measurement with infra-red based capnography and 81mKr-gas radioactive gamma camera. The authors found a complete tracer gas removal within 1.0 seconds with clearance half times decreasing with increasing NHF. In their summary, the rapid clearance was attributed to a potential for NHF to reduce dead space CO_2 rebreathing though no such reductions have been observed clinically due to the difficulty in quantifying CO_2 clearance in the airway in vivo (Möller et al. (2015)).

1.6 Motivations and Thesis Summary

From the review of published data on NHF, it is notable that little attention has been paid to evaluation of work of breathing and CO_2 flushing in the adult population, and even in the neonate and infant groups, the power of findings (impact of studies) has been limited by the number of participants. Also, the number of parameters (airway pressure, breathing flow, gas tensions) that can be measured simultaneously is often restricted by patient pathology and technology. Additionally, inter- and intra- population variation do not permit data drawn from different sources to be united into an accurate understanding of NHF therapy.

It is intuitive to think that administration of NHF will make inspiration easier and expiration difficult as inspiration flow is along NHF jet and expiratory flow is counter to the NHF jet. It has been observed that both inspiratory and expiratory pressure rise with NHF (Groves and Tobin (2007); Parke et al. (2009)). The relationship between pressure gradient and flow in a straight pipe is linear but non-linear for a complex geometry such as

the airway (Ferris et al. (1960)) i.e. resistance to flow in the airway is dependent on flow such that increasing flow increases airway resistance (Otis et al. (1950)). This suggests an increased airway resistance to flow during inspiration if NHF adds to the breathing flow and thus a rise in inspiratory effort. Further, some of the cannula flow exit through the leak area between the prongs and the nares after recirculation in the nasal cavity. When inspiratory flow demand exceeds the cannula flow, the extra flow entrained from the atmosphere would have to overcome the resistance posed by the small entry area (difference between cannula prong area and nares) and the momentum of the exiting cannula flow following recirculation. Does it mean inspiration may be more difficult with NHF than without? It is worth mentioning that the jet momentum can drive some flow through the airway during inspiration. When these considerations are taken together, it is difficult to predict the influence of NHF on inspiratory effort of breathing. Even with a correct prediction that NHF will raise expiratory resistance, it is of interest to know how much rise is expected, for instance when there is a 10 % rise in NHF. Finally, how the change in breathing flow parameters such I:E ratio due to NHF, may affect overall breathing effort (inspiration plus expiration) is not readily straightforward.

In investigating the mechanism of action of NHF, the present work aims at providing quantitative data via bench-top modelling and mathematical simulation on the effect of NHF on work of breathing and CO_2 flushing. Some interesting questions to be answered include:

- Does NHF increase or reduce inspiratory resistance?
- Does NHF increase or reduce expiratory resistance?
- What is the overall work of breathing with NHF, including inspiratory and expiratory work of breathing ?
- What assumptions can be made to produce a simple mathematical model for gas exchange and work of breathing?
- Can a simple mathematical model of gas exchange predict CO_2 flushing?

- Can a simple mathematical model be used to study effect of NHF on central sleep apnea patients?

The Chapters of this thesis are ordered thus: Chapter 2 is a description of the tools developed for conducting bench-top model studies. In Chapter 3, results from the experimental measurement of tracheal pressure (of a 3D printed upper airway model of a neonate and adult) in closed mouth and open mouth states are presented for a range of NHF flows. Tests aimed at finding the effect of nasal cannula size on tracheal pressure are also presented. The chapter closes with estimation of the resistance of the upper airway model to airflow during NHF. Chapter 4 encompasses the development of a model to estimate work of breathing based on the calculated upper airway resistance parameters and clinically observed effects of NHF on breathing parameters. Bench-top measurement of airway pressure and CO_2 concentration were made to validate a computational fluid dynamics (CFD) model aimed at investigating the effect of NHF on airway pressure, velocity distribution and CO_2 clearance. This is presented in Chapter 5. Chapter 6 is a study of the effect of NHF on CO_2 clearance in individuals suffering from central sleep apnea. In Chapter 7, the influence of breathing flow waveform shape on $EtCO_2$ concentration is investigated using four COPD breathing flow waveforms collected from the literature. Chapter 8 embodies the development of a mathematical model to predict how NHF affects $EtCO_2$ clearance. The conclusion, essential outcomes and future work are presented in chapter 9.

Generally, this work focuses on two main areas of research namely the impact of NHF on breathing effort and airway CO_2 content and how the breathing flow pattern of COPD patient may bear on airway CO_2 concentration. A road map summarising the research goals pertaining to these focus areas and the approaches used is presented in Fig. 1.9.

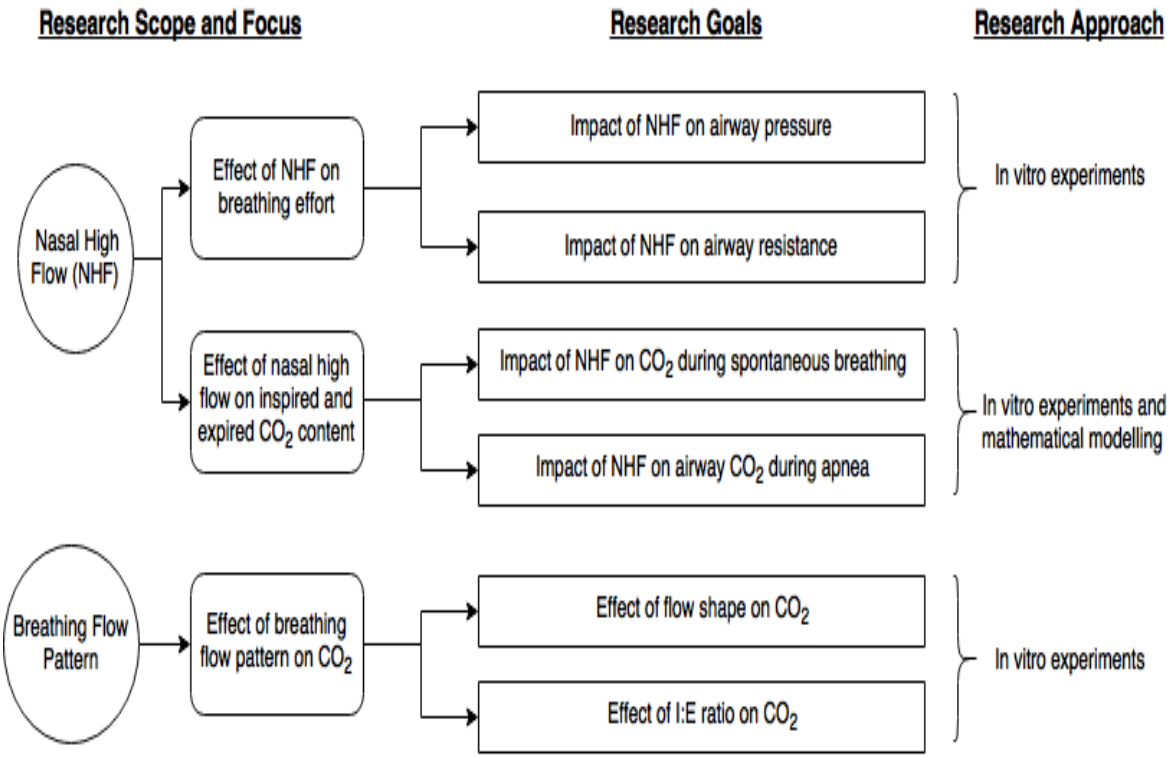

Fig. 1.9 Road map indicating the research focus areas, main research goals and research approaches used for investigation

Chapter 2

Laboratory Instrumentation

2.1 Introduction

The parameters to be measured include airway pressure, airway resistance, and CO_2 concentration. Previous to the commencement of this work, an in-house pulsatile pump capable of reproducing breathing flow patterns was built to study how NHF influences air velocity distributions in the upper airway using particle imaging velocimetry techniques (Spence (2011)). A capnograph was available (MiniMedi, manufactured by Oridion Medical Ltd, USA) which uses infrared technology to quantify CO_2 concentration by sampling at a rate 20 Hz via a 2 m capillary tube. Its response time and resolution are 2.7 seconds and 0.1 mmHg respectively. The MiniMedi capnograph (Fig. 2.1) was used for the present work. It was calibrated against the atmosphere and a 10 % CO_2-air calibration gas mix.

The multi pressure sensor system (used by Dey (2014)) was made of MPXV7002DP pressure sensors (Fig. 2.2). It has a measurement range of -2000 Pa to 2000 Pa and an accuracy of $\pm$ 2.5 %. At the beginning of this work, a stability problem potentially due to drifts in the output voltage characteristics of the sensors and the need to measure neonatal airway pressure prompted the design of a more reliable and accurate pressure acquisition system.

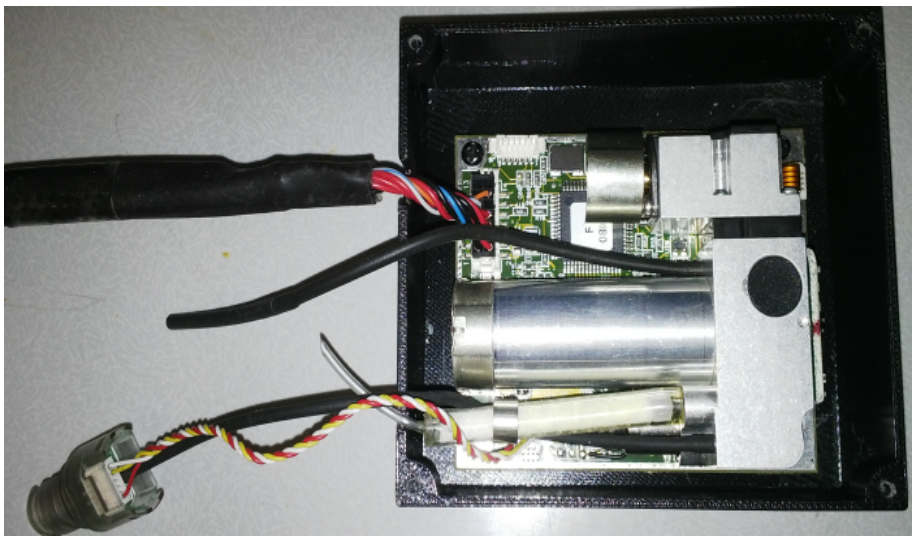

Fig. 2.1 MiniMedi capnograph

Fig. 2.2 The MPXV7002DP pressure sensor (adapted from http:// www.aliexpress.com)

A TSI 4000 flow meter was used to measure breathing flow rate. After examination, a calibration of the TSI 4000 flow meter showed an error of 6.4 % therefore flow rates stated or plotted in the thesis should be multiplied by 1.064 to find the best estimate of the true flow rate. Also a new pulsatile pump identical to the one used by Dey (2014) was built with some improvements. A description of the new pulsatile pump is presented in the next section followed by a description of the new pressure acquisition system.

2.2 The Pulsatile Pump

The piston motion is achieved by converting the rotary motion of a stepper motor (ASTROSYN ML34HY1-9) into translatory motion via a pulley, belt and ball screw assembly. As the stepper motor rotates in clockwise or anticlockwise steps, the belt transfers the rotary motion to the ball screw which in-turn drives the piston fastened to it forward or backwards depending on the direction of the stepper motor. The design step angle of the stepper motor is 1.8 ° (equivalent to 200 steps/revolution). In a previous study aimed at investigating the effect of compliance on models of arterial hemodynamics (see work by Geoghegan (2012)), an Astrosyn P808A Micro-stepping motor driver was used to increase the number of steps per revolution to 1050. This means an improvement in the resolution and hence quality of data generated using the pump. The new pulsatile pump (Fig. 2.3) was fitted with the same device. The plunger of the piston is supported on a rail (Fig. 2.3) via a ball bearing arrangement to reduce friction. At a distance of 40 mm from either ends of the ball screw, a terminal switch is installed to stop the stepper motor in case it fails to stop at the preset displacement of the piston. The piston cylinder has an inside diameter of 140 mm, an outside diameter of 150 mm and a length of 420 mm. It is held in place by two arched steel plates as shown on Fig. 2.3.

Compared to the old pump, the re-designed supporting arch allows for ease of removal of the piston cylinder. The maximum volume and flow of air deliverable by the system are 4.6 L and 50 L/min respectively. A 10 mm diameter tapped hole is made at a distance of 35 mm from the front end of the cylinder for the purpose of bleeding CO_2 into the cylinder (Fig. 2.3). The CO_2 inlet fitting (see Fig. 2.3), attached to the piston cylinder, has also been redesigned to make it easy to replace.

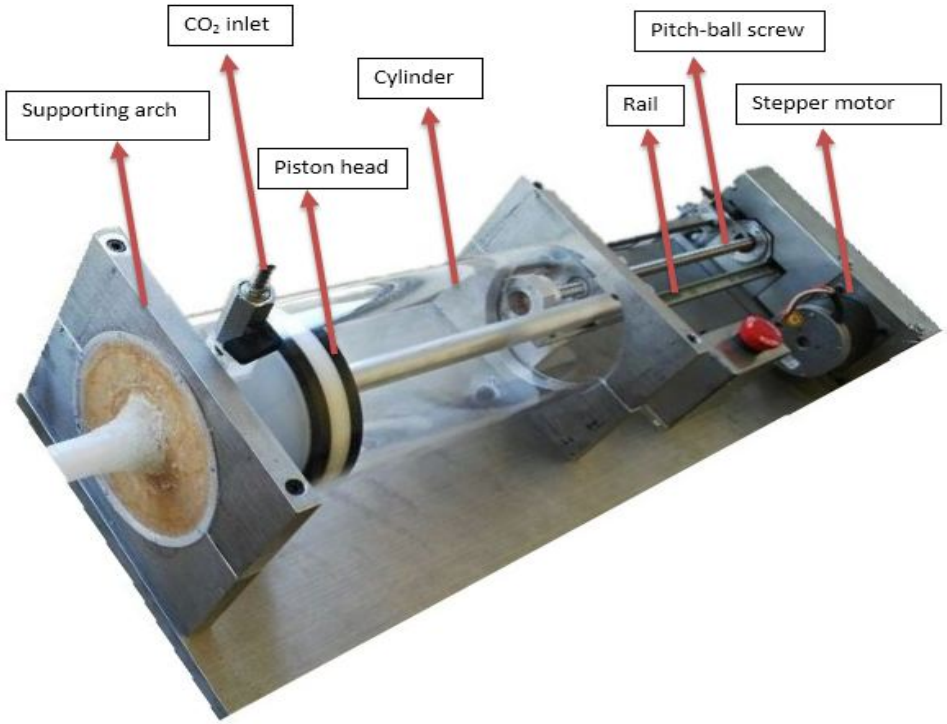

Fig. 2.3 New pulsatile pump with labels on parts

The pump is controlled by an in-house software (originally developed for the older pump), which is programmed in LabVIEW (version 2012). The software requires the Fourier coefficients of a flow waveform (q) and its period to run. The Fourier coefficients are obtained using Eq. 2.1

$$q(t) = a_o + \sum_{n=1}^{N} (a_n cos(\frac{n\pi t}{T}) + b_n sin(\frac{n\pi t}{T})) \tag{2.1}$$

Where N and T respectively represent the number of Fourier coefficients and period of the flow waveform. a and b are accordingly the cosine and sine coefficients required by the

pump's LabVIEW program. The first 8 Fourier coefficients contain 99 % of the energy of the physiological flow waveform and therefore can accurately reproduce the flow waveform (Geoghegan et al. (2012)). The displacement of the piston is computed in the software using Eq. 2.2 (integral computed with trapezium method).

$$x(t) = \frac{1}{A}\int_0^T q(t)dt \tag{2.2}$$

Where A is the cross-sectional area of the piston head.

2.3 The Pressure Acquisition System

The need to build a new pressure acquisition system was prompted by the detection of instability in the existing pressure sensors and the need for a higher accuracy in measuring low amplitude airway pressure. In this section, the system requirements, design considerations and methods used to build the new multi pressure sensor system are discussed.

2.3.1 Selection of pressure transducer

In the selection of the pressure transducer, the following specifications were considered: pressure range (< 500 Pa), response time (< 10 ms), voltage supply (< 5 V) and communication protocol (I^2C or SPI). The AMS5915 pressure transducer (manufactured by Analog Microelectronics GmbH, Germany) - see Fig. 2.4 - met these specifications. This pressure sensor has an onboard chip to process and transmit pressure data as a digital signal using I^2C protocol. This is an advantage because noise and losses due to long transmission lines

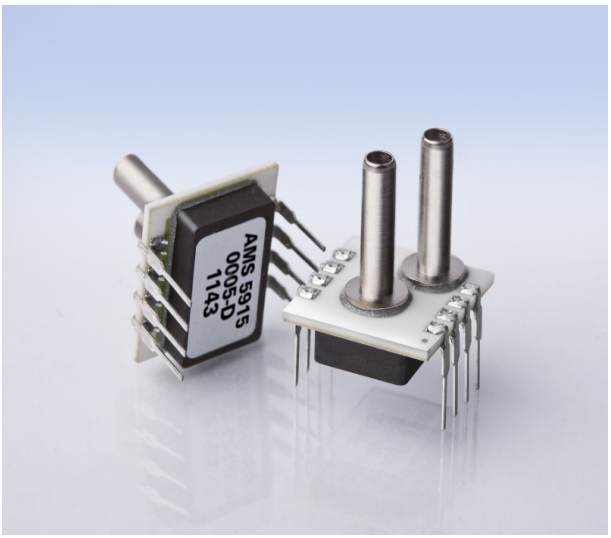

Fig. 2.4 The AMS5915 pressure sensor (adapted from http://www.messweb.de)

are avoided. The specifications of AMS5915 are listed in Table 2.1. Once the pressure transducer was selected, the next step was to design the multi pressure measurement and acquisition system.

Table 2.1 Specifications of the AMS5915 pressure sensor

Parameter	Typical value	Unit
Range	-500 to 500	Pa
Accuracy	$\pm$ 1.5	% FSO
Supply voltage	3.3	V
Current	5	mA
Reaction time	0.5	ms
Thermometer (on board)	-25 to 85	$^\circ$ C
Dimension	15.24 x 15.24 x4.3	mm
Transmission protocol	I^2 C	-

2.3.2 Design of the data acquisition system

10 units of the AMS5915 were sourced to build the pressure data acquisition system. A sampling frequency of 25 Hz was specified for the data acquisition system and to achieve this an Arduino nano V.3 board (Fig. 2.5, right) which is powered by an Atmega328P microcontroller was sourced. The nano V.3 board has a clock speed of 16 MHz; a program

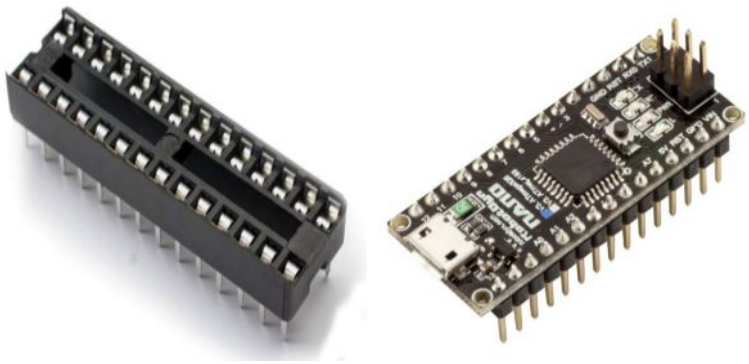

Fig. 2.5 The Arduino nano3 and the dual-in-line socket

memory of 32 KB; and the capability to read data from 128 pressure transducer devices via its I^2C lines. Additionally, its small size (43mm X 18mmX 10mm) makes it portable. A dual-in-line pin (DIP) socket (Fig. 2.5, left) was sourced to make replacement of the nano V.3 in the system easy.

The next phase involved the development of the schematic of a printed circuit board (PCB) for the system. DesignSpark PCB 7.1 (PCB development software) was chosen because it was relatively easy to learn and use, and it is open source. In Table 2.2, specifications for the PCB design are listed.

Table 2.2 Specifications of the PCB

Parameter	**Value**	**Unit**
Board dimension	110 x 90	mm
Copper track width	0.64	mm
Minimum track spacing	0.25	mm
Pad type	round	mm
Pad diameter	1.82	mm
Dual-in-line package width	0.85	mm

Upon completing the schematic of the PCB (Fig. 2.6a) it was printed and developed on a two-sided copper laminated board. Afterwards, 0.5 mm diameter holes were drilled at positions marked for insert pins of electronic components (the pressure sensors, resistors, the DIP socket). Following from this the AMS5915, DIP and pull-up resistors (required for the I^2 C circuitry) were soldered on the printed circuit board (See Fig. 2.6b)

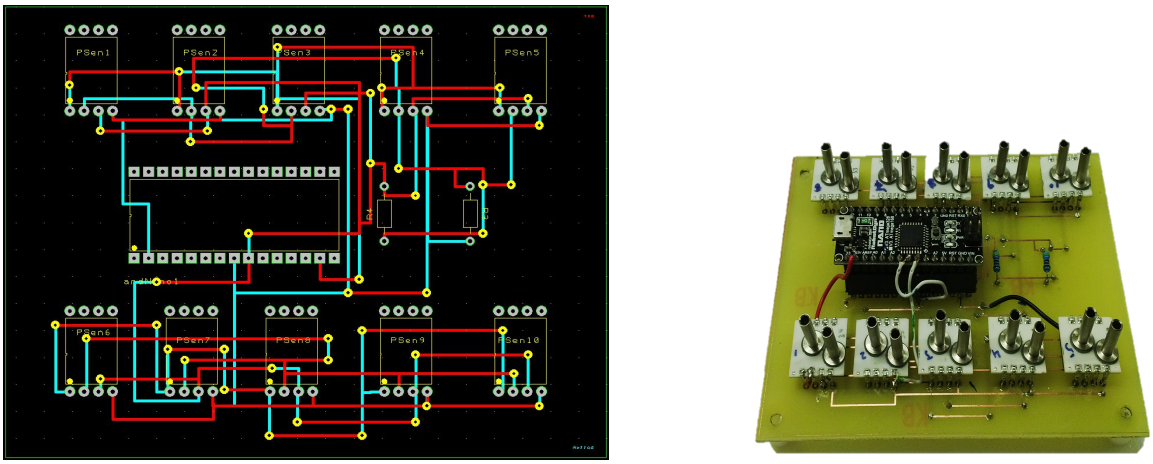

(a) PCB schematic (b) PCB with components soldered

Fig. 2.6 Schematic and built PCB

2.3.3 Programming the arduino nano 3 V.3

The embedded software was written in C program using the Atmel Studio 7 integrated development environment. A flow chart which defines the structure of the embedded software is shown in Fig. 2.7. The numbering on Fig. 2.7 shows the sequence of activities that define the operation of the system.

Basically, the microcontroller issues an instruction that activates a pressure transducer (activity 1 (Fig. 2.7)) and directs it to make a measurement (activity 2). The microcontroller receives and acknowledges a signal which indicates completion of measurement by the transducer and then requests the pressure data (in hexadecimal form) to be transmitted for storage in memory (activities 3 and 4). Activities 1, 2, 3 and 4 (as encased in the dashed rectangle), are repeated for all 10 pressure transducers allowing a time interval of 1μs (1 MHz) between repeats. The sampling frequency (25 Hz) is a negligible fraction of the repeat frequency (of activities 1 - 4) and thus produces no significant inter sensor timing disparities i.e. data from all sensors can be considered as arriving simultaneously for conversion and transmission. Once the pressure data from all sensors are received, it is then converted into decimal form (activity 5), bundled into a 50 word length signal and sent via the universal serial

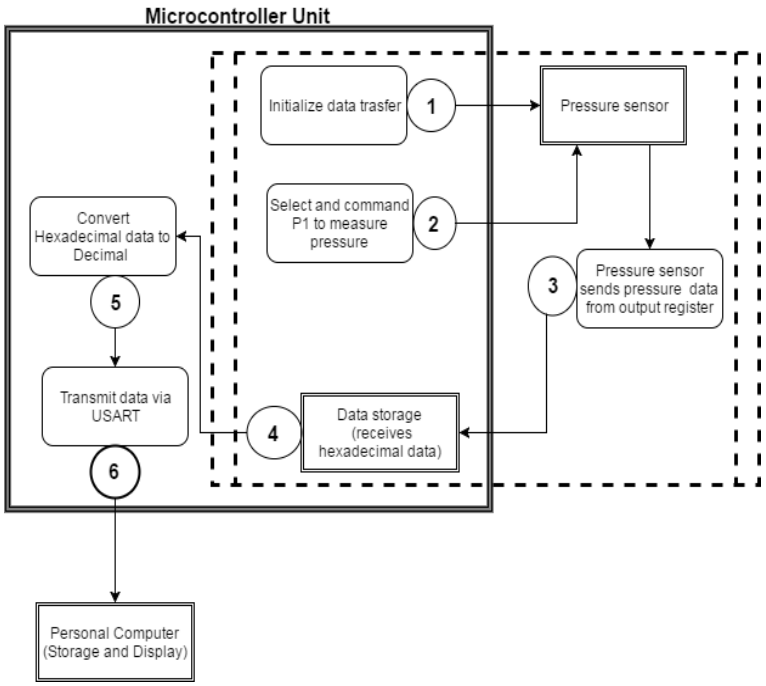

Fig. 2.7 Flow chart for pressure acquisition

asynchronous receiver-transmitter (USART) line (activity 6) to a computer for recording and graphical user interface display.

According to its data sheet, the AMS5915 pressure sensors are factory programmed to self-calibrate using sensor specific correction coefficients stored on its electrically erasable programmable read only memory (EEPROM). All sensors were however checked against a factory calibrated digital pressure device (Testo 510 differential pressure sensor) which has an accuracy of $\pm$ 3 Pa, $\pm$5 Pa and $\pm$ 10 Pa that respectively correspond to pressure ranges of 0 to 30 Pa, 31 to 100 Pa, and 101 Pa to 10000 Pa. The AMS5915 reported 3 % less pressure than the Testo 510. This was corrected by scaling the digital output of the AMS5915 by 3 %.

2.3.4 Designing of the housing

To protect the PCB and on-board microchips of the pressure sensors from possible damage, a housing unit was designed and built. The design (Fig. 2.8a) was done in SolidWorks (Version 2012). A base cover was designed to enclose the housing unit. The prototype of

the housing unit (Fig. 2.8b) was 3D-printed using ABS material by the fused deposition modelling method. Four screws, each located at a corner of the horizontal surface (Fig. 2.8b), were required to fasten the housing unit to the bottom cover. The completely assembled prototype of the pressure acquisition system is shown in Fig. 2.8b.

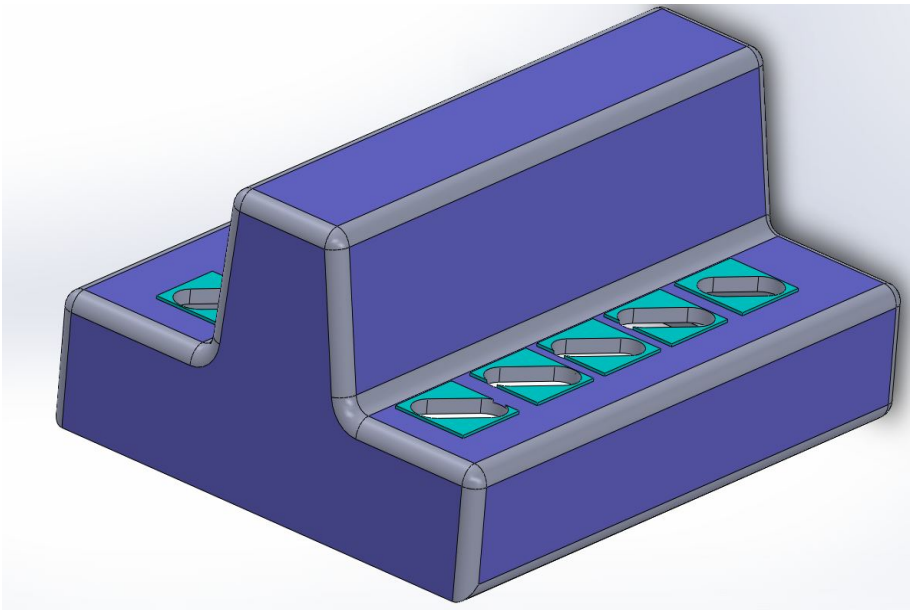

(a) CAD model of housing

(b) Fully assembled pressure acquisition system

Fig. 2.8 Housing for pressure acquisition system

2.3.5 Design of the graphical user interface

It was desired that the measured pressure be displayed on a computer screen during experiment. A graphical user interface (GUI) that permits the display and recording of data from any of the transducers was developed in MATLAB (Version 2014). A snap-shot of the GUI is shown on Fig. 2.9. See Table 2.3 for information about the buttons and panes on the GUI.

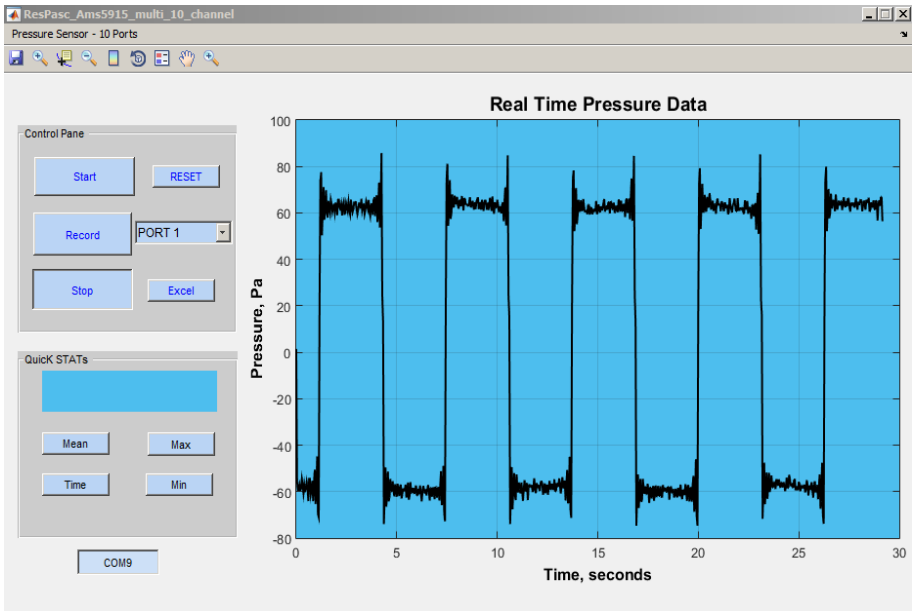

Fig. 2.9 Graphical user interface for the pressure acquisition system

The pressure data measured in successive experiments can be stored together in one file. Also, there is a functionality which allows simple statistical calculations (e.g. finding mean, maximum and minimum data points) to be performed immediately on recorded data.

Table 2.3 Functions of buttons and panes on GUI

Parameter	Value
Start	Enable data plotting
Stop	End plotting
Port	Select sensor
Excel	Record data
Reset	Clear data and reset axis
Mean	Compute data average
Max	Find maximum value
Min	Find minimum value
Time	Show recording time
COM	Select communication port

2.4 Airway Model Making

The airway models used in the present work were constructed by previous students from computed tomographic (CT) images acquired retrospectively. The model acquisition, preparation and printing process are briefly described here.

Modern medical imaging provide a rich source of information about anatomical structures that are otherwise difficult to replicate. Computed tomography and magnetic resonance images are good examples. CT images slices (2D cross-sectional images) of the upper body of a 44 year old male with no apparent physical abnormalities was acquired. Following from this, a segmentation algorithm was used to demarcate pixels that belonged to a specific range of intensities (thresholding). Segmentation was used to mark the areas of the airway in each CT image slice. There are commercial and free software packages (e.g. 3D Slicer (www.slicer.org)) that are able to group all the marked airway regions on the image slices into a volume object. The software can then reconstruct a 3D object from the segmented image slices. Manual editing of unwanted features (e.g. paranasal sinuses, Hasner's membrane, auditory tubes) and residual surfaces (due to little distinction in pixel intensity between airway tissue and surrounding tissue) may be required. Editing of the geometry can be performed with Meshlab (www.meshlab.sourceforge.net) and Meshmixer (www.meshmixer.com). Because the facial geometry around the nares may influence the inhalation flow profile, the area

around the nostril and upper lips were retained during segmentation. A shelling algorithm was used to produce a model shell of 3mm thickness (wall thickness of airway geometry). After editing the model, it was printed in acrylic photopolymer material (Visijet EX200) with a Project HD 3000 Plus printer.

2.5 Conclusion

A pulsatile pump capable of reproducing a breathing flow pattern was built to study pressure and flow characteristics of the airway along with CO_2 concentration fluctuations during spontaneous breathing and breathing under conditions of nasal high flow (NHF). Following from this, a ten-port multi pressure transducer system was designed to enable the accurate, fast and simultaneous measurement of pressure at ten different regions of the airway. In addition, an interactive graphical user interface program was developed in MATLAB (Version 2014) for immediate pressure data plotting and recording plus a functionality that makes it possible to perform quick statistical analysis. Summarily, the hardware requirement to successfully complete the present work have been presented in this chapter.

Chapter 3

Effect of NHF on Airway Pressure and Resistance

3.1 Introduction

The resistance to flow of the airway must be known in order to estimate the work of breathing (Otis et al. (1950)). NHF increases airway pressure in both neonates (Locke et al. (1993); Wilkinson et al. (2008)) and adults (Parke et al. (2009)) and therefore affects the pressure - flow characteristics of the airway. During expiration, the breathing flow is against the cannula flow and it is thought that this may increase expiratory resistance however quantitative data on this effect is lacking (Dysart et al. (2009)). Recently, Lee et al. (2013b) mentioned that "whether high flow nasal cannula reduces work of breathing by mechanically stenting the airway or by providing gas flow that matches or exceeds the patient's peak inspiratory flow as proposed by Dysart et al. (2009) remains to be determined". Furthermore, there is little information on how the choice of nasal cannula size and mouth state (open or closed) may affect work of breathing. This chapter provides measurement of tracheal pressure with different cannula sizes and flow rates, from which the upper airway resistance of an adult and neonate is estimated.

3.1.1 Chapter nomenclature

K_1 - laminar resistance coefficient

K_2 - turbulent resistance coefficient

MO - mouth open

MC - mouth close

NHF - nasal high flow

NHF3 - 3 L/min of NHF

NHF6 - 6 L/min of NHF

NHF9 - 9 L/min of NHF

NHF20 - 20 L/min of NHF

NHF40 - 40 L/min of NHF

NHF60 - 60 L/min of NHF

OPT842 - small cannula size (adult)

OPT844 - medium cannula size (adult)

OPT846 - large cannula size (adult)

OPT314 - small cannula size (neonates)

OPT316 - large cannula size (neonates)

UAM - upper airway model

ZPIF - zero pressure inspiratory flow

3.2 Materials and Methods

3.2.1 Experimental setup

Existing adult and neonate upper airway models were used. In fabricating the adult upper airway model, computed tomography (CT) images of the upper airway of a 44 year old male adult, with no apparent airway abnormality, and in a mouth open resting state, were

segmented to extract the airway. The sinuses were deleted and the model terminated at the trachea. The 3D model (Fig. 3.1a) was 3D printed in acrylic (Visijet EX200). The upper airway model of a neonate (healthy male weighing 3.6 Kg), Fig. 3.1b, was also 3D printed in acrylic. This was a closed mouth model i.e. the baby had his or her mouth closed at the time of the scan. A complete description of model making methods can be found in the report by Geoghegan et al. (2012). To study mouth closed breathing, which is recommended for NHF, the oral opening of the adult was sealed. In reality, during a mouth closed posture, the tongue may or may not occlude the oral cavity. Since the tongue is absent in the model, an unoccluded mouth closed posture was simulated. The mouth was unsealed to study open mouth breathing.

(a) Adult UAM (b) Neonate UAM2

Fig. 3.1 Upper airway models: neonate and adult

A 1 mm diameter hole was drilled through the posterior surface close to the trachea opening of the UAM for pressure measurement. Though the tracheal opening is circular, pressure sampled at the anterior surface may be different. This is a limitation. A positive displacement programmable piston pump (PP) (used by Van Hove et al. (2016) and Spence (2011)) was connected to the adult UAM (Fig. 3.1a). The PP is able to produce bidirectional flows up to 50 L/min. A TSI 4000 flow meter was used to confirm the flow delivered by the PP was as expected from the piston velocity. After examination, a calibration of the TSI

4000 flow meter showed an error of 6.4 % therefore flow rates stated or plotted in the thesis should be multiplied by 1.064 to find the best estimate of the true flow rate. An AIRVO2^{TM} nasal high flow device (manufactured by Fisher & Paykel Healthcare Limited, Auckland, New Zealand) was used to administer NHF via a breathing circuit and nasal cannula (Fisher & Paykel Healthcare Ltd). The apparatus setup is shown in Fig. 3.2. The nasal cannula was placed such that the two prongs rested in the nostril with mid-section of the space between the prongs aligned with the septum of the nostril. A misalignment to the right or left can lead 7 - 14 % change in pressure (also observed by Buchajczyk (2017)). During the experiments, the cannula base, which rests on the upper lip during NHF was firmly secured with Blu-tack without obstruction to breathing flow. Before each test, rectangular flow waves were used to ensure that variation in pressure due to cannula placement was less that 1 %. A pressure transducer (AMS 5915, Analog Microelectronics GmbH, Germany) was connected to the pressure tap at the tracheal opening (P_1 in Fig. 3.2). P_2 is the atmospheric pressure.

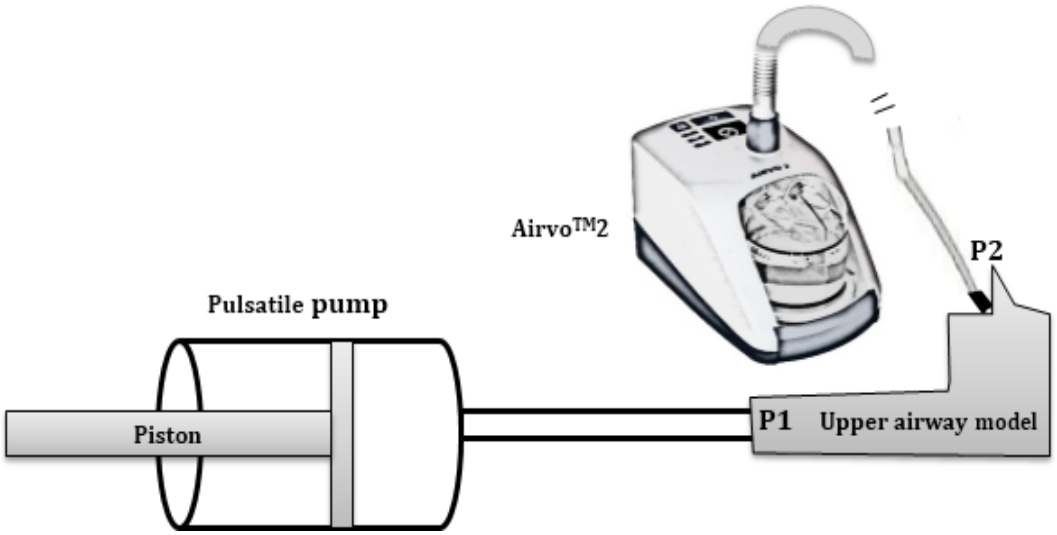

Fig. 3.2 Apparatus setup

Three different cannula sizes namely: small (OPT842), medium (OPT844) and large (OPT846) (manufactured by Fisher & Paykel Healthcare) were used to administer nasal high flow to the adult UAM. NHF was delivered to the neonatal UAM using the OPT314 and

OPT316 nasal cannula (Fisher & Paykel Healthcare). See Table 3.1 for the dimensions of all the cannula used in this work.

Table 3.1 Dimensions of the adult and neonate nasal cannula used in this work

Prong dimensions	**OPT842 (small)**	**OPT844 (medium)**	**OPT846 (large)**	**OPT314 (neonate)**	**OPT316 (neonate)**
Area of prong two holes (mm^2)	42.2	60.5	113.1	9.1	16.6
Wall thickness (mm)	0.4	0.4	0.5	0.4	0.4
Height (mm)	13	15	18	8	8
Distance apart (mm)	14	15	18	10.6	12

3.2.2 Experimental procedure

The resistance of the adult UAM itself was first determined by driving steady flow rates (F), measured by the piston motion, and ranging from -50 L/min to 50 L/min through the UAM. Negative flow rates denote inspiration. Rohrer's equation (Otis et al. (1950)), Eq. 3.1, describes the relationship between air flow and the driving pressure (P)

$$P = K_1 F + K_2 F^2 \tag{3.1}$$

where K_1 and K_2 are resistance coefficients, respectively for the laminar and turbulent components of the resistance. Airway resistance, R, is defined as $R = P/F$ thus Eq. 3.2

$$R = K_1 + K_2 F \tag{3.2}$$

is obtained by dividing through Eq. 3.1 by F. Due to the second term in Eq. 3.2, resistance depends on flow rate. K_1 and K_2 in Eq. 3.1 are determined by least-squares fitting to the recorded flow (F) and differential pressure data ($P = P_2 - P_1$)

The mouth of the UAM was sealed and unsealed to simulate mouth open and mouth closed breathing. Tracheal pressure was recorded without NHF, and with NHF delivered via the small (OPT842), medium (OPT844) and large (OPT846) cannula. For each cannula, the flow rate through the cannula (NHF flow rate) was set at 20, 40 and 60 L/min in turn. The PP was used to deliver rectangular flow waves in which the steady flow ranged from -50 to 50 L/min in steps of 10 L/min. The piston motion determined the tracheal flow. Identical sets of experiments were conducted using the neonate UAM (Fig. 3.1b) however tracheal flows ranging from 1 to 6 L/min were used along with NHF of 3 L/min, 6 L/min and 9 L/min which were separately administered via the OPT314 and OPT316 cannula.

3.3 Results

3.3.1 Adult airway pressure and resistance (mouth closed)

Fig. 3.3 shows the expiratory pressure flow plots for NHF at 20 L/min (NHF20), 40 L/min (NHF40) and 60 L/min (NHF60) for all cannula sizes and flow rates induced by the piston motion (tracheal flow). Fig. 3.4 is the inspiratory pressure flow plot. The error bars represent two standard deviations in pressure calculated over 25 cycles (5 cycles from each of 5 separate experimental repeats). During expiration, except for NHF20, the pressure produced by the medium cannula is almost the same as that of the large cannula however during inspiration the pressure produced by the medium cannula is less than that of the large (except for NHF20). At each tracheal flow (ranging form 0 to 50 L/min), the expiratory tracheal pressure produced by the large cannula was divided by the pressure produced by the small cannula. The range and mean of the ratios at NHF20, NHF40 and NHF60 are 1.09 - 1.18 (1.14) , 0.91 - 1.13 (1.09), 0.91 - 1.11 (1.08) respectively. The range of ratios and mean computed for the inspiratory phase, respectively corresponding to NHF20, NHF40 and NHF60 are 1.00 - 1.20 (1.06) , 0.67 - 1.9 (1.13), 0.48 - 1.90 (1.07). In reference to the mean ratios, expiratory tracheal pressure rises by 14 %, 9% and 8 % respectively at NHF20, NHF40 and

NHF60 when the large cannula is used instead of the small. The corresponding inspiratory rise in tracheal pressure are 6 %, 13 % and 7 %. It is concluded that for both inspiration and expiration the large cannula produces a tracheal pressure increase of 6 - 14 % relative to the small cannula.

For both inspiration and expiration, the pressure rises quadratically with flow rate i.e. the K_2 term in Eq. 3.1 cannot be neglected. NHF rates have a greater effect on pressure than cannula size. The resistance coefficients, K_1 and K_2 were deduced from each of the curves shown in Fig. 3.3 and Fig. 3.4 and used to compute the resistance at a tracheal flow of 30 L/min - Fig. 3.5 and Fig. 3.6 - from which it is observed that resistance increases in an NHF dependent manner. The NHF jet produced by the large cannula has a relatively less momentum but a greater pressure compared to that of the small cannula due to the Bernoulli effect. The change of trachea pressure per a change in breathing flow (defined by the linear resistance coefficient) generally rises with NHF and cannula size (Table 3.2) for both inspiration and expiration. Thus for mouth closed breathing, a rise in airway pressure due to NHF and cannula size produces a corresponding rise in resistance to flow. During expiration, the large cannula produces the greatest resistance at all NHF values (Fig. 3.5). Replacing the large cannula with the medium cannula reduces expiratory resistance by 5 %, 4 % and 2 %, respectively corresponding to NHF20, NHF40 and NHF60. Replacing the large cannula with the small reduces expiratory resistance by 12 %, 20 % and 16 % respectively.

In Fig. 3.6 (for inspiration), the overlap of error bars at NHF20 and NHF40 means cannula size makes little difference to resistance however at NHF60, replacing the large cannula with the medium and small cannula respectively reduce resistance by 6 % and 12 %. It can be concluded that for mouth closed breathing in adults, between the small and large cannula sizes, there is a significant difference in expiratory resistance at all NHF (20 - 60 L/min) but during inspiration the difference in resistance between these two sizes of cannula is only significant at NHF60.

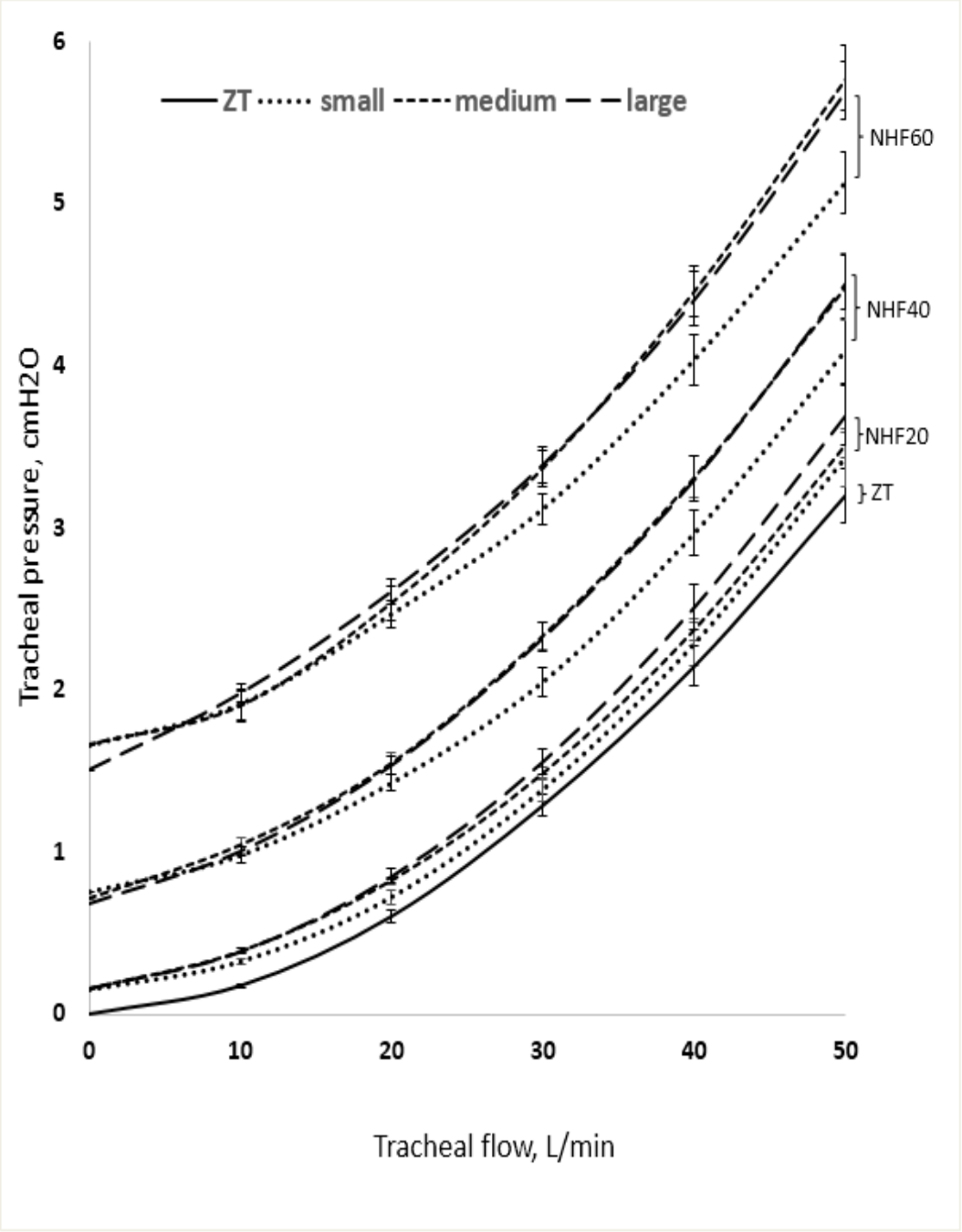

Fig. 3.3 Expiratory pressure flow relationship for adult UAM without NHF and with NHF20, NHF40 and NHF60 administered via the small, medium and large cannula. The error bars represent two standard deviations in pressure measured over 25 cycles

The pressure flow data obtained via the medium cannula for inspiration and expiration (Fig. 3.3 and Fig. 3.4) have been plotted together (Fig. 3.7) to investigate the contribution of

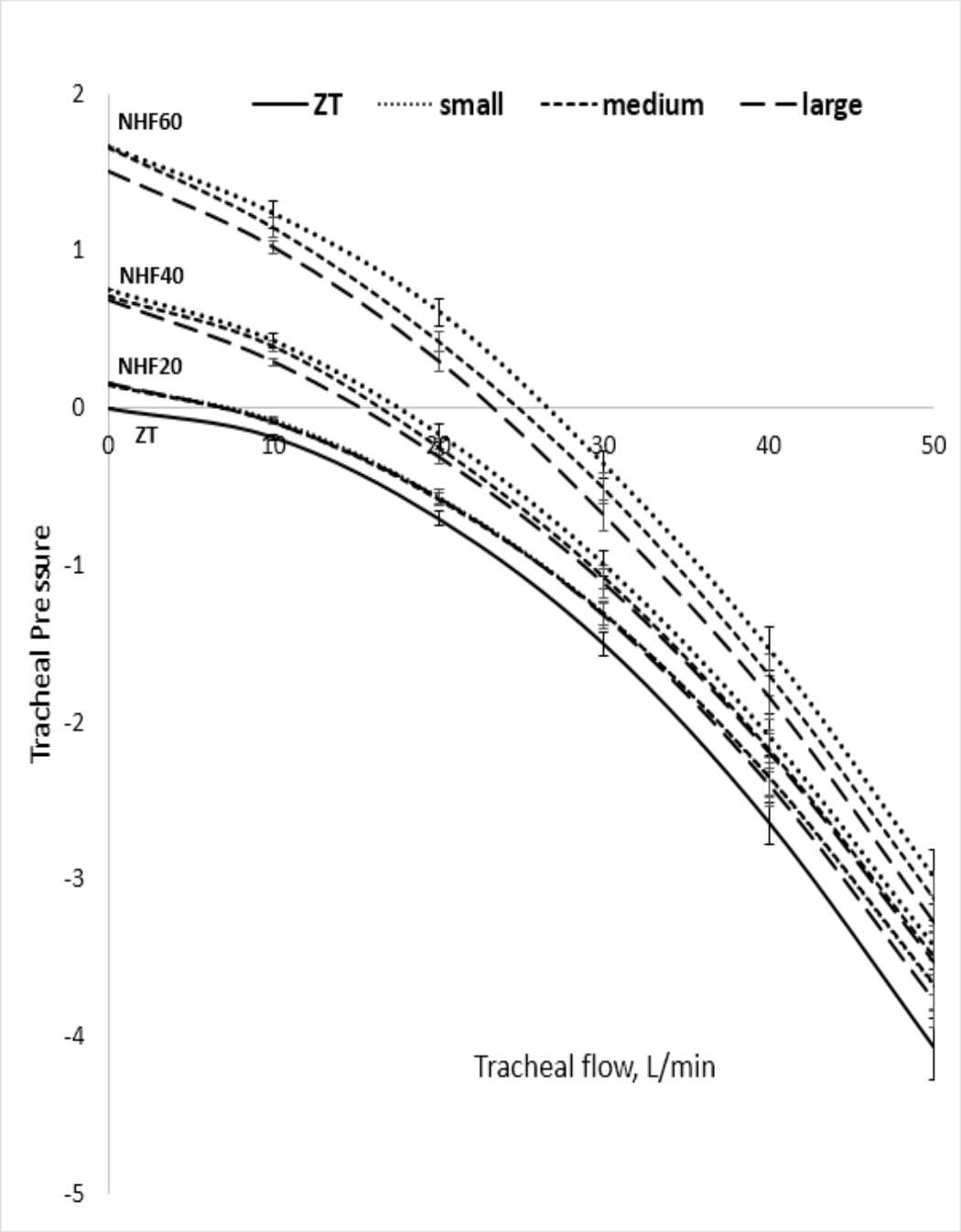

Fig. 3.4 Inspiratory pressure flow relationship for adult UAM without NHF and with NHF20, NHF40 and NHF60 administered via the small, medium and large cannula. The error bars represent two standard deviations in pressure measured over 25 cycles

inspiratory and expiratory resistance to the effort of breathing during NHF. The conclusions can be generalised for all cannula sizes. Note that in Fig. 3.7, at zero tracheal flow (piston

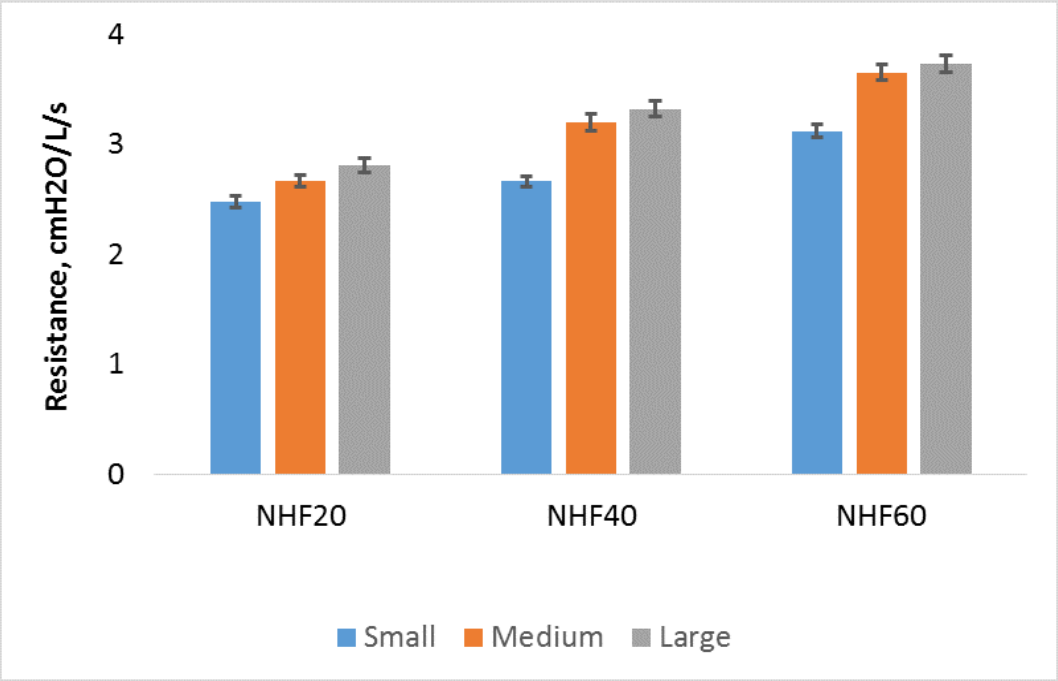

Fig. 3.5 A plot of expiratory resistance of the UAM at tracheal flow of 30 L/min when NHF20, NHF40 and NHF60 were administered via the small, medium and large cannula sizes. The standard errors in resistance due to errors in flow and pressure are shown by the error bars

not moving), the inflow through the cannula is balanced by the outflow through the leak area between the nares and cannula prongs. The pressure (P_2) at zero net flow is non-zero for all NHF and increases with increasing NHF. These pressures are produced by the stagnation of the cannula jet in the upper airway. The zero-therapy state, ZT, (no cannula in place, no NHF flow) is also shown. It is observed that the pressure (effort) required to produce a particular tracheal flow through the upper airway increases with NHF for expiration but reduces for inspiration. However the pressure change required to produce a given change in flow is greater during inspiration.

As shown in Fig. 3.7, the change in inspiratory pressure (dPi) required to increase tracheal flow by 10 L/min is greater than that required by expiration (dPe). This suggests a greater inspiratory resistance than expiratory resistance.

At the flow rate named zero pressure inspiratory flow (ZPIF) in Fig. 3.7, the pressure at the trachea required to drive inspiratory flow is zero. This flow rate is referred to as the

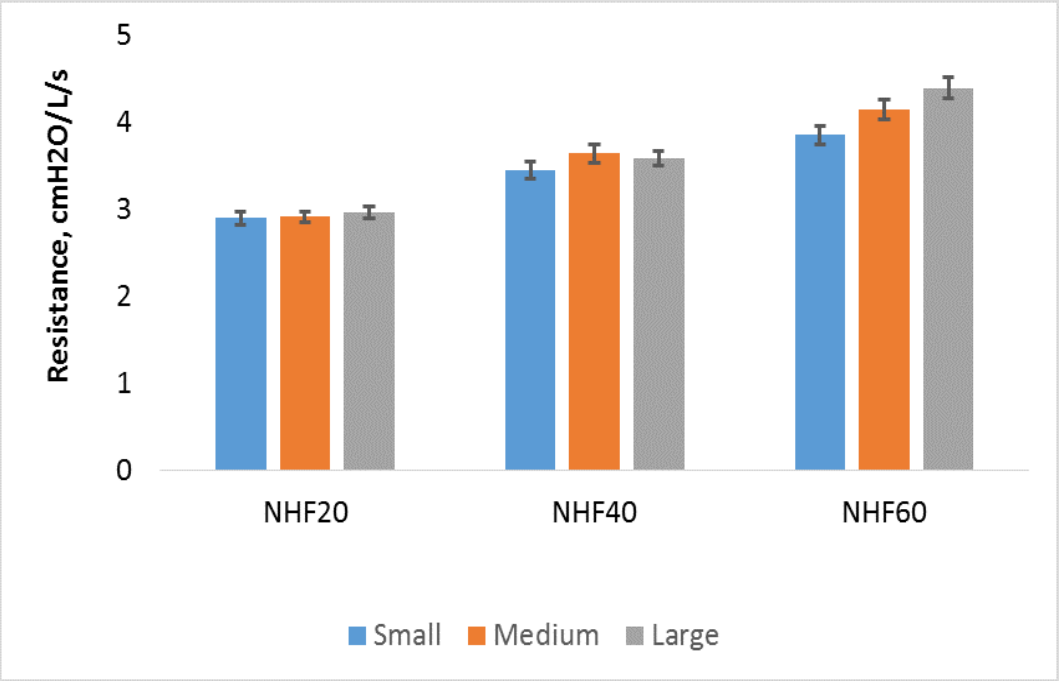

Fig. 3.6 A plot of inspiratory resistance of the UAM at tracheal flow of 30 L/min when NHF20, NHF40 and NHF60 were administered via the small, medium and large cannula sizes. The standard errors in resistance due to errors in flow and pressure are shown by the error bar

zero pressure inspiration flow (ZPIF). As NHF increases the ZPIF also rises. At flow rates between ZPIF and zero no muscular effort is required to drive inspiration against upper airway resistance. Inspiration is driven by NHF. In Fig. 3.8, the breathing flow of a male adult (age = 24 years) is shown. The horizontal lines represent the ZPIF.

When NHF20 is applied, for instance, from the start of inspiration up to a flow rate of 7.5 L/min (ZPIF at NHF20), no respiratory effort will be required to overcome upper airway resistance. Only the effort needed to overcome lower airway resistance and lung elastance is required. Muscular effort is only required to overcome upper airway resistance between time = **a** and time = **b** until expiration begins. As NHF flow rate increases, ZPIF rises and less effort is required over the inspiratory phase. Note that the ZPIF at NHF60 is greater than the peak inspiratory flow suggesting effortless inspiratory breathing across the upper airway.

The following illustration shows how the uncertainties in K_1 and K_2 (Table 3.2) were calculated. At NHF60, the average pressure and standard deviation corresponding to the

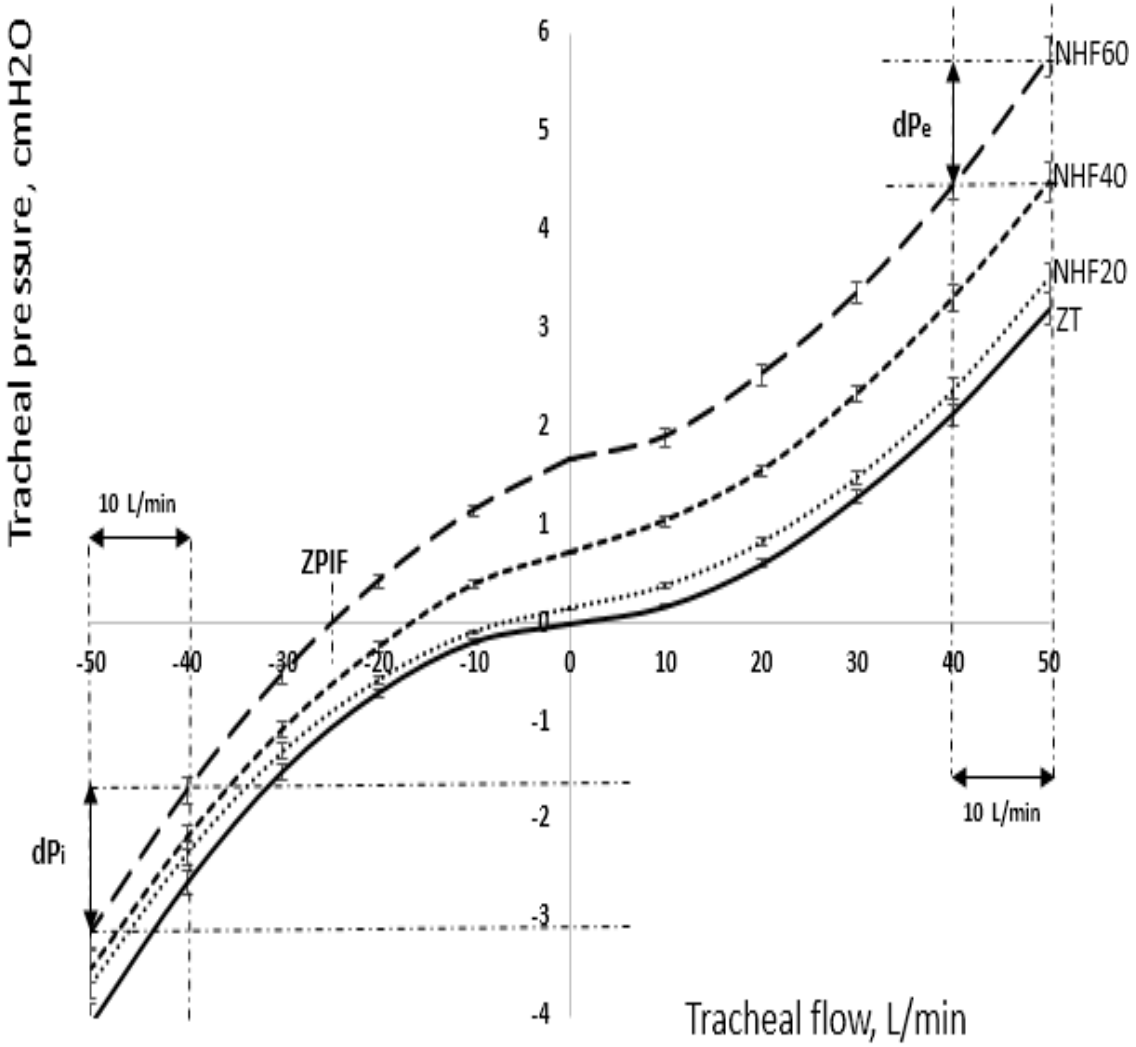

Fig. 3.7 Pressure-flow relationship for adult UAM during inspiration and expiration at ZT and NHF20, NHF40 and NHF60, administered via the medium cannula. The error bars represent two standard deviations in pressure measurement

steady tracheal flows ranging from 0 to 50 L/min (in steps of 10 L/min) are 1.66±0.01, 1.89±0.05, 2.53±0.05, 3.37±0.05, 4.46±0.06, 5.77±0.1 (all in units of cmH_2O). Subtracting the greatest standard deviation i.e. 0.1 cmH_2O (in the last data point) from all the pressure averages except 5.77 cmH_2O and adding 0.1 cmH_2O to 5.77 cmH_2O gives the following data point (only averages): 1.56, 1.79, 2.43, 3.27, 4.36, 5.87 (in cmH_2O), herein referred to as uncertainty data. In Fig. 3.9, the averages of the latter pressure data (uncertainty data) and those of the former are plotted against flow. It is seen that the uncertain data deviates

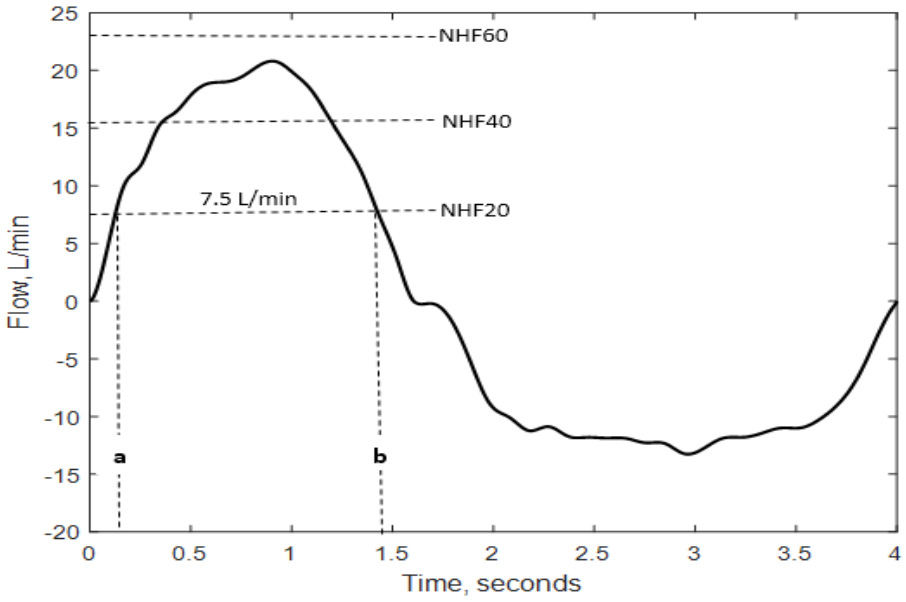

Fig. 3.8 The breathing flow pattern of a male adult (age =24). The ZPIF for NHF20, NHf40 and NHF60 found for the UAM are shown

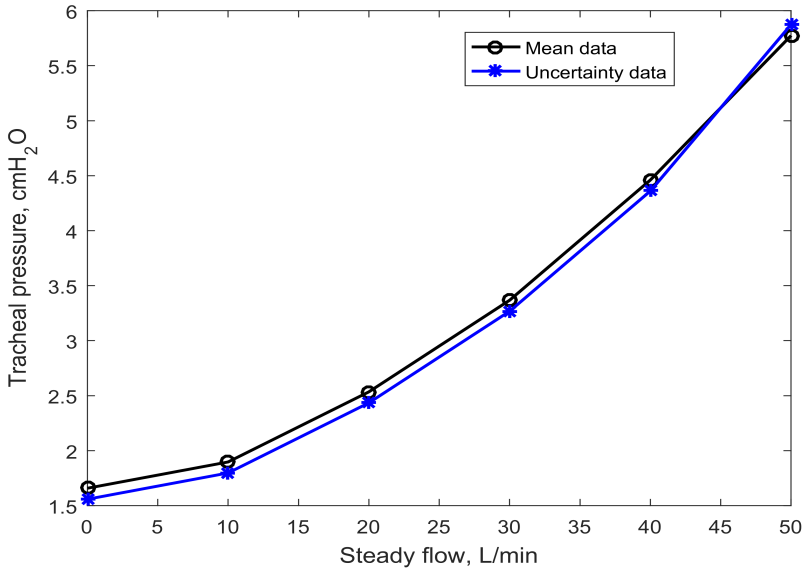

Fig. 3.9 Plots showing maximum deviation in pressure data

from the original data and represent greatest deviation that can be seen in the original data. The K_1 and K_2 values for both plots (Fig. 3.9) were calculated (by fitting to Eq. 3.1). The differences between these resistance coefficients for both plots indicates the uncertainty in their estimation.

The calculated K_1 and K_2 values (and uncertainties in their estimation) for inspiration and expiration for all cannula sizes during ZT, NHF20, NHF40 and NHF60 have been presented in Table 3.2.

Table 3.2 Resistance coefficients of the adult UAM (in close mouth state) during ZT and administration of NHF20, NHF40 and NHF60 via the small, medium and large cannula sizes. R^2 denotes the coefficient of determination of the least squares fit of the pressure flow plots Rohrer's equation

	Inspiration			**Expiration**		
	$\mathbf{K_1}$	$\mathbf{K_2}$	$\mathbf{R^2}$	$\mathbf{K_1}$	$\mathbf{K_2}$	$\mathbf{R^2}$
ZT	0.04±0.01	4.89±0.11	0.99	0.19±0.01	4.09±0.09	1.00
Small cannula						
NHF20	0.24±0.30	5.00±0.14	1.00	0.25± 0.08	4.43±0.06	1.00
NHF40	1.23±0.26	4.54±0.13	0.99	0.57±0.09	4.10±0.07	1.00
NHF60	1.64±0.53	4.72±0.35	1.00	1.15±0.69	3.63±0.48	1.00
Medium cannula						
NHF20	0.48±0.36	4.90±0.22	1.00	0.61±0.07	4.09±0.05	0.99
NHF40	1.40±0.01	4.40±0.12	0.99	1.26±0.24	3.93±0.07	0.99
NHF60	2.28±0.50	4.14±0.33	1.00	1.13±1.07	4.63±0.83	1.00
Large cannula						
NHF20	0.39±0.26	5.15±0.36	0.99	0.64±0.15	4.32±0.00	1.00
NHF40	1.49±0.40	4.26±0.22	0.99	1.26±0.29	4.00±0.15	0.99
NHF60	2.26±0.25	4.18±0.11	0.99	1.97±0.04	3.61±0.09	1.00

3.3.2 Adult airway pressure and resistance (mouth open)

Fig. 3.10 shows the pressure flow characteristics of the adult UAM during open mouth breathing. The error bars represent two standard deviations in measured tracheal pressure over 25 cycles (5 cycles from 5 separate repeats).

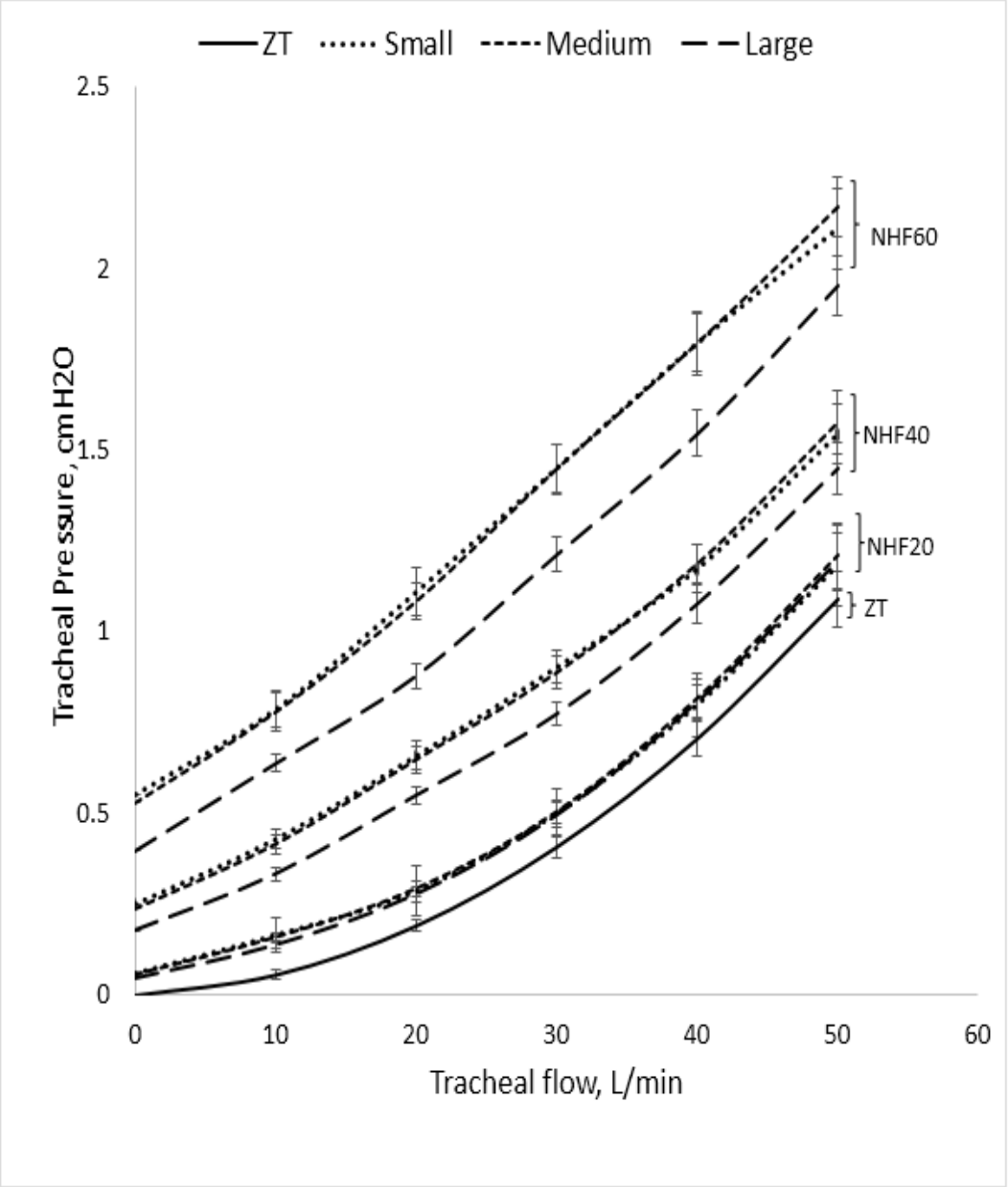

Fig. 3.10 Expiratory pressure flow relationship for adult UAM without NHF and with NHF20, NHF40 and NHF60 administered via the small, medium, and large cannula. The error bars represent two standard deviations in pressure measured over 25 cycles

Error bar overlap is observable at NHF40 and NHF60 between the plots of the small and medium cannula. Th expiratory tracheal pressure produced at each tracheal flow (ranging from 0 to 50 L/min) by the large cannula was divided by that of the small cannula. The range and mean of the ratios at NHF20, NHF40 and NHF60 are 0.99 - 1.29 (1.09), 1.06 - 1.42 (1.21), 1.08 - 1.40 (1.22) respectively. Identical ratios were computed for the inspiratory phase. The range and mean of the ratios corresponding to NHF20, NHF40 and NHF60 are 0.73 - 1.29 (1.0) , 0.69 - 2.66 (1.25), 0.67 - 1.40 (1.23) respectively. Comparing the mean ratio during expiration to that of inspiration at NHF40 and NHF60, it is seen that they are within a narrow range. By taking the average of the corresponding means (e.g. $(1.21 + 1.25)/2 = 1.23$, at NHF40), it is concluded that in open mouth breathing, for both inspiration and expiration, there is a tracheal pressure rise of 23 % at NHF40 and NHF60, and 9 % at NHF20 when the small cannula is used instead of the large cannula.

Fig. 3.11 shows inspiratory pressure flow plots during mouth open breathing with the small and medium cannula producing almost the same tracheal pressures (also greater than that of the large cannula) at all tracheal flows as observed for the expiratory phase. In the closed mouth breathing state, the large cannula produced the greatest airway pressure (Fig. 3.3). In general, mouth open breathing engenders lower airway pressures compared to mouth closed breathing. The resistance coefficients (and their uncertainties) calculated from the pressure flow plots on Fig. 3.10 and Fig. 3.11 are presented in Table 3.3

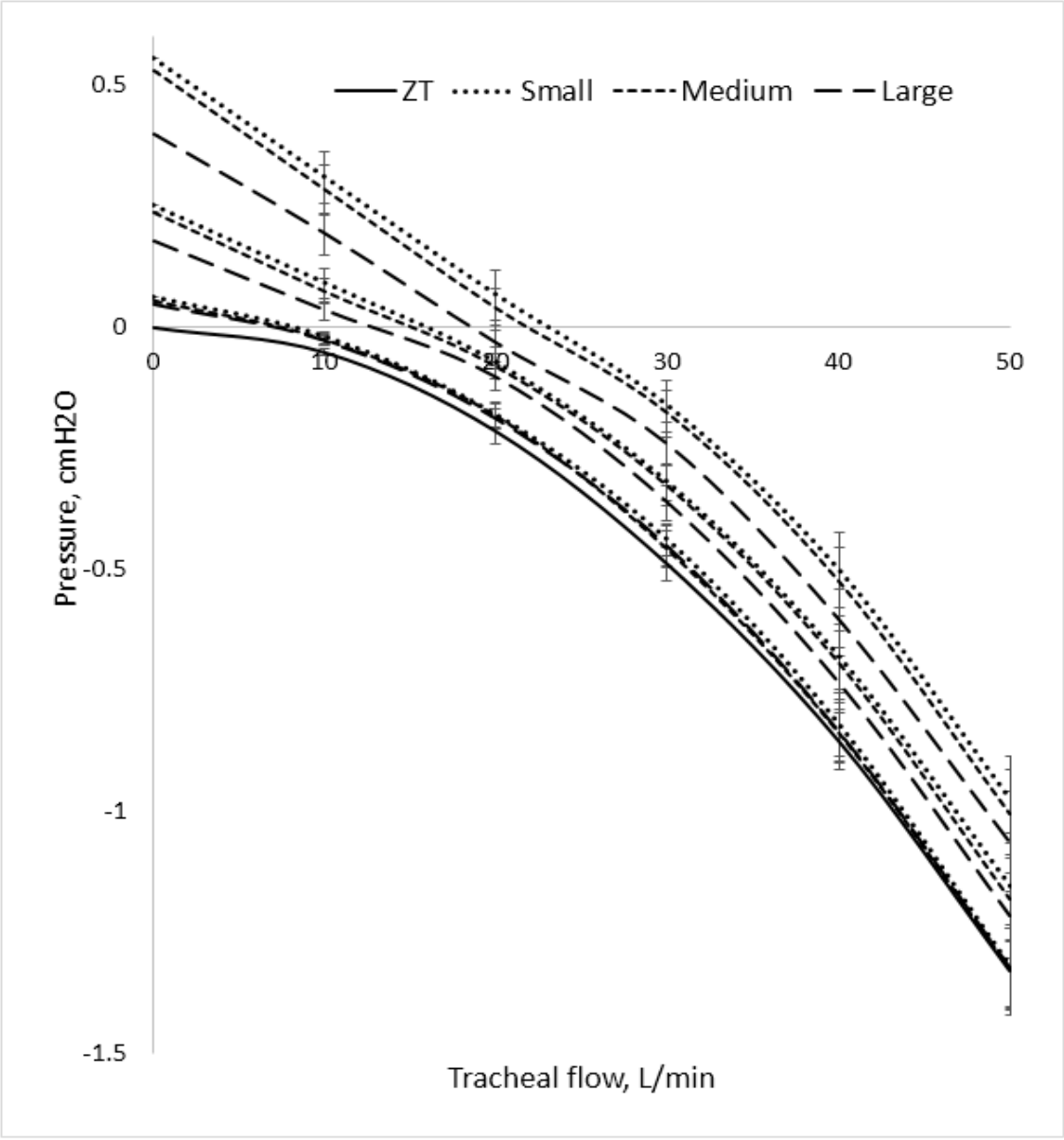

Fig. 3.11 Inspiratory pressure flow relationship for adult UAM without NHF and with NHF20, NHF40 and NHF60 administered via the small, medium, and large cannula. The error bars represent two standard deviations in pressure measured over 5 cycles

Table 3.3 Resistance coefficients of the adult UAM (in open mouth state) during ZT and administration of NHF20, NHF40 and NHF60 via the small, medium and large cannula sizes. R^2 denotes the coefficient of determination of the least squares fit of the pressure flow plots Rohrer's equation

	Inspiration			**Expiration**		
	K_1	**K_2**	**R^2**	**K_1**	**K_2**	**R^2**
ZT	0.03±0.05	1.88±0.21	1.00	0.08±0.02	1.48±0.32	1.00
Small cannula						
NHF20	0.05±0.02	1.91±0.16	1.00	0.20±0.19	1.35±0.24	1.00
NHF40	0.38±0.23	1.51±0.40	1.00	0.93±0.10	0.72±0.04	1.00
NHF60	0.95±0.85	0.98±0.70	1.00	1.65±0.70	0.32±0.07	1.00
Medium cannula						
NHF20	0.08±0.03	1.88±0.12	1.00	0.20±0.17	1.40±0.22	1.00
NHF40	0.33±0.05	1.58±0.49	0.99	0.88±0.04	0.85±0.03	1.00
NHF60	0.92±0.85	1.58±0.49	1.00	1.57±0.56	0.51±0.45	0.99
Large cannula						
NHF20	0.06±0.00	1.89±0.12	0.99	0.21±0.08	1.39±0.13	1.00
NHF40	0.23±0.04	1.69±0.38	0.99	0.74±0.01	0.93±0.04	1.00
NHF60	0.72±0.66	1.17±0.52	1.00	1.22±0.08	0.77±0.02	1.00

3.3.3 Adult airway pressure: mouth closed (MC) versus mouth opened (MO); expiration versus inpiration

From Fig. 3.3, Fig. 3.4, Fig. 3.10 and Fig. 3.11, it is concluded that tracheal pressure varies with tracheal flow, NHF flow, mouth state (closed or opened) and cannula size. How the airway pressure during mouth closed (MC) breathing compares to mouth opened (MO) breathing under conditions of NHF may have clinical implications. The tracheal pressure, at a particular NHF and tracheal flow, were averaged for all cannula sizes as:

$$([Pressure]_{OPT842} + [Pressure]_{OPT844} + [Pressure]_{OPT846})/3 \tag{3.3}$$

[Pressure]$_{OPT842}$, [Pressure]$_{OPT844}$, [Pressure]$_{OPT846}$ are the tracheal pressures corresponding to the small (OPT842), medium (OPT844) and large (OPT846) cannula respectively. The average pressure (Eq. 3.3) at all NHF (NHF20, NHF40, and NHF60) and tracheal flows (for both MC and MO states) are presented in Table 3.4. The ratios of the MC pressure to the MO pressure (MC/MO), are also presented in Table 3.4.

It is observable that the MC/MO ratio for all tracheal flows at a particular NHF are close. This prompted the calculation of the averages of these ratios and their standard deviations (see Table 3.4 (italicised)). Note how the average MC/MO ratios corresponding to NHF20 (2.81), NHF40 (2.75) and NHF60 (2.66) are within a narrow range i.e. 2.66 to 2.81 during expiration. The difference in ratios at different NHF is less than one standard deviation i.e. not statistically significant. The range of ratios for inspiration is 2.97 to 3.29. Due to the very low inspiratory tracheal pressure (during MO breathing) at tracheal flows of 10 L/min and 20 L/min for NHF40 and NHF60 respectively, – see asterisks in Table 3.4, the very high corresponding pressure ratios were treated as outliers (as they are far greater than the other ratios) and were not included in the calculation of the average of the pressure ratios. The excluded values (outliers) are due to division by lower values of MO tracheal pressures.It can be concluded that irrespective of the tracheal flow and NHF, expiratory MC breathing

produces an average tracheal pressure (standard deviation) which is 2.7 (0.28) times that of MO breathing whilst that for inspiration is 3.1 (0.34) times greater .

Table 3.4 Average tracheal pressure of small, medium and large cannula for MC and MO breathing

Expiratory pressure (cmH_2O)

NHF (L/min)	**20**			**40**			**60**		
Flow (L/min)	**MC**	**MO**	**MC/ MO**	**MC**	**MO**	**MC/ MO**	**MC**	**MO**	**MC/ MO**
0	0.15	0.05	3	0.72	0.22	3.24	1.61	0.49	3.26
10	0.36	0.15	2.35	1.01	0.39	2.57	1.93	0.73	2.62
20	0.80	0.29	2.79	1.51	0.62	2.43	2.54	1.02	2.47
30	1.47	0.50	2.95	2.24	0.86	2.61	3.29	1.37	2.40
40	2.39	0.81	2.96	3.19	1.15	2.78	4.30	1.71	2.51
50	3.55	1.2	2.96	4.36	1.53	2.86	5.53	2.08	2.66
Average of ratios			***2.81***			***2.75***			***2.66***
Std. Dev. of ratios			***0.23***			***0.28***			***0.31***

Inspiratory pressure (cmH_2O)

NHF (L/min)	**20**			**40**			**60**		
Flow (L/min)	**MC**	**MO**	**MC/ MO**	**MC**	**MO**	**MC/ MO**	**MC**	**MO**	**MC/ MO**
0	0.15	0.05	3.00	0.72	0.22	3.24	1.61	0.49	3.26
10	-0.08	-0.02	4.00	0.37	0.007	***5.61**	1.13	0.26	4.35
20	-0.57	-0.18	3.09	-0.24	0.09	2.80	0.44	0.02	***18.81**
30	-1.31	-0.45	2.91	-1.06	-0.34	3.16	-0.52	-0.19	2.67
40	-2.36	-0.83	2.85	-2.15	0.70	3.06	-1.69	-0.54	3.11
50	-3.70	-1.32	2.80	-3.48	-1.18	2.95	-3.13	-1.01	3.08
average of ratios			***2.97***			***3.04***			***3.29***
Std. Dev. of ratios			***0.22***			***0.17***			***0.63***

The change in tracheal pressure with breathing direction (inspiration or expiration) under NHF conditions was also investigated. This was done by finding the ratio of the expiratory and inspiratory tracheal pressure at all tracheal flows at a particular NHF in Table 3.4. For instance, during MC breathing at NHF20, the expiratory to inspiratory pressure ratios for tracheal flows ranging 0 - 50 L/min in steps of 10 L/min are $0.15/0.15 = 1, 0.36/0.08 =$

$4.35, 0.80/0.57 = 1.40, 1.47/1.31 = 1.13, 2.39/2.36 = 1.01, 3.55/3.70 = 0.96$. It is seen that these ratios are comparable except for second term ($0.36/0.08 = 4.35$, which is due to the low inspiratory pressure near the ZPIF) which is considered as an outlier. The average of these ratios equals 1.10. Such average ratios were calculated for NHF40 and NHF60 and these corresponded to 1.71 and 1.75. Note that these average ratios are based on pressure data (Tabel 3.4) averaged over cannula size (Eq. 3.3). By taking into account the variations due to cannula size, the ratio of expiratory pressure to inspiratory pressure was 1.04 - 1.14 (for NHF20), 1.59 - 1.86 (for NHF40) and 1.72 - 2.33 (for NHF60). Identical average ratios were were computed for MO state. The range for ratios corresponding to NHF20, NHF40 and NHF60 are 1.09 - 1.12, 1.45 - 2.32, 2.18 - 2.33.

It is concluded that in both MC and MO states, the ratio of expiratory to inspiratory tracheal pressure rises with NHF. Generally, for MC state, the percentage rise of expiratory tracheal pressure over inspiratory tracheal pressure at NHF20, NHF40 and NHF60 are 9 %, 72 % and 103 % respectively. For MO state, the expiratory pressure rises by 11 %, 88 % and 125 % for NHF20, NHF40 and NHF60 respectively. Note that these percentages are the averages of the range of ratios presented above.

3.4 Neonatal Airway Pressure and Resistance

The pressure flow plots obtained when NHF of 3 L/min (NHF3), 6 L/min (NHF6) and 9 L/min (NHF9) were delivered via the OPT314 (smaller) and OPT316 (larger) cannula sizes are shown on Fig. 3.12. That for zero-therapy (ZT) - no NHF - is also shown. The error bars represent two standard deviations computed over 25 cycles (5 cycles from 5 separate tests). It is observable that cannula size makes no significant difference to inspiratory (negative flow) pressure flow characteristics (as the error bars overlap) except at NHF9.

During expiration, cannula size produces a significant difference in tracheal pressure for all NHF except NHF3. OPT316 produces a greater tracheal pressure during inspiration

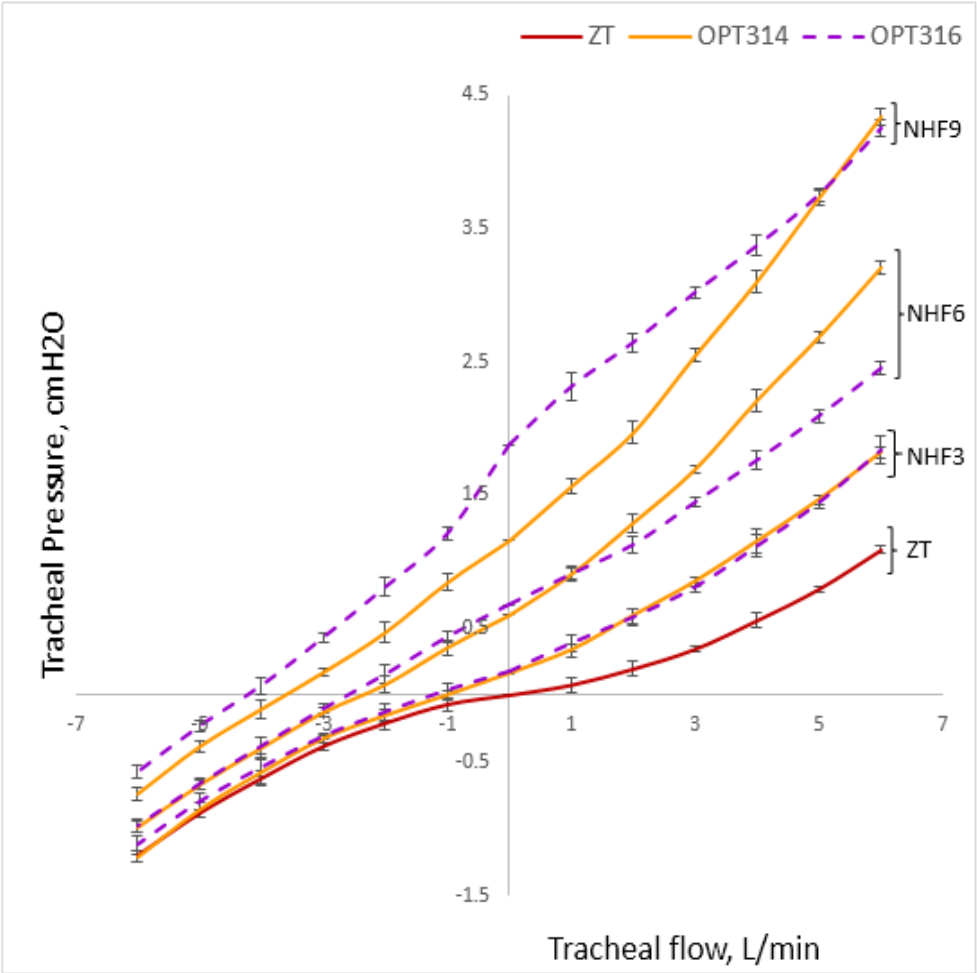

Fig. 3.12 Inspiratory and expiratory pressure flow relationship for the neonate UAM without NHF and with NHF3, NHF6 and NHF9 administered via OPT314 and OPT316 cannula. The error bars represent two standard deviations in pressure measured over 5 cycles

and expiration at NHF9. This is consistent with the recommended use of OPT314 (which is specified for NHF range of 2 - 8 L/min) and OPT316 (NHF range of 3 - 15 L/min). At NHF6 however, OPT314 produces a greater tracheal pressure compared OPT316. The resistance coefficients (and their uncertainties) calculated for the pressure flow plots shown on Fig. 3.12 are presented in Table 3.5. It can be seen that the linear resistance coefficients, K_1, consistently increase with NHF for both inspiration and expiration irrespective of cannula size. The nonlinear component, K_2, decreases with NHF during inspiration for OPT314

and expiration for OPT316. K_2 follows no particular trend during the expiratory phase for OPT314 and inspiratory phase for OPT316.

Table 3.5 Resistance coefficients of the neonate UAM (in closed mouth state) during ZT and administration of NHF3, NHF6 and NHF9 via the small, medium and large cannula sizes. R^2 denotes the coefficient of determination of the least squares fit of the pressure flow plots Rohrer's equation

	Inspiration			**Expiration**		
	K_1	**K_2**	**R^2**	**K_1**	**K_2**	**R^2**
ZT	3.62±1.31	84.97±24.94	1.00	3.18±2.18	76.77±36.15	1.00
OPT314 cannula						
NHF3	5.86±1.79	75.02±11.04	1.00	11.33±3.50	53.55±27.18	1.00
NHF6	13.47±3.78	21.30±13.47	1.00	18.87±3.17	74.63±24.86	1.00
NHF9	20.05±2.91	12.88±3.02	1.00	23.19±5.02	88.87±41.44	1.00
OPT316 cannula						
NHF3	6.47±3.44	63.46±25.83	1.00	8.94±2.59	74.03±18.40	1.00
NHF6	14.67±3.46	18.05±12.78	1.00	12.72±4.90	51.16±37.36	1.00
NHF9	32.61±12.45	91.21±35.89	0.99	20.80±3.07	22.15±5.01	0.99

The resistance of the neonate UAM to a tracheal flow of 5 L/min at ZT, NHF3, NHF6 and NHF9 have been shown in Table 3.6. At a tracheal flow of 5 L/min, inspiratory and expiratory resistance consistently increase with NHF in both cannula sizes. OPT314 (which is smaller) however produced a greater expiratory resistance but a generally lower inspiratory resistance than OPT316.

Table 3.6 Resistance of neonate UAM at 5 L/min during NHF

	OPT314 cannula		**OPT316 cannula**	
	Inspiratory Resistance @ 5 L/min (cmH_2O/L/s)	**Expiratory Resistance @ 5 L/min (cmH_2O/L/s)**	**Inspiratory Resistance @ 5 L/min (cmH_2O/L/s)**	**Inspiratory Resistance @ 5 L/min (cmH_2O/L/s)**
NHF3	12.11	15.79	11.76	15.11
NHF6	15.25	25.09	16.17	16.99
NHF9	21.13	30.59	40.22	22.65

3.5 Discussion

The present study supports previously reported observations (Locke et al. (1993); McGinley et al. (2007); Parke et al. (2009)) that airway pressure increases with NHF and varies with cannula size (Mündel et al. (2013)). This study is however the first to explore the effect of cannula size on airway pressure in anatomically realistic airway model of an adult and a neonate and further examine the influence of mouth state (open or closed) on airway pressure for a wide range of NHF (20 to 60 L/min). The use of an invasive method to obtain tracheal pressure may be a reason why these studies have not been done clinically. Mündel et al. (2013) found that NHF of 15 L/min produced a greater nasal pressure with the large cannula compared to the small cannula. Their model was simpler than the current one, with an axis-symmetric passage including a constriction that simulated the nasal valve. Their results and the present results agree qualitatively.

In the closed mouth state, the leak area between the cannula prong and the nostril contributes to the rise in pressure with cannula size as the expired flow must pass through a smaller area with greater pressure loss. As expected, the large cannula was found to produce the greatest resistance whilst the small cannula produced the least in the adult upper airway model. At NHF40 (mouth closed state) for instance, the expiratory resistance due to NHF administration via the large cannula was 20% higher than when delivered through the small cannula.

In open mouth state (adult UAM), the small and medium cannula produced a greater tracheal pressure than the large cannula during inspiration and expiration. Spence (2011) found that during expiration, the cannula flow passing through the nasopharynx towards the trachea joins the lung flow and exits via the oral cavity as shown in Fig. 3.13. The cannula flow through the nasopharynx (towards the trachea) was observed to decrease with increasing expiratory lung flow whilst the leakage through the area between the cannula prongs and nostril greatly increased (Spence (2011)). Since the smaller cannula, compared to the large cannula, produces a jet of greater momentum and penetration into the nasopharynx, relatively

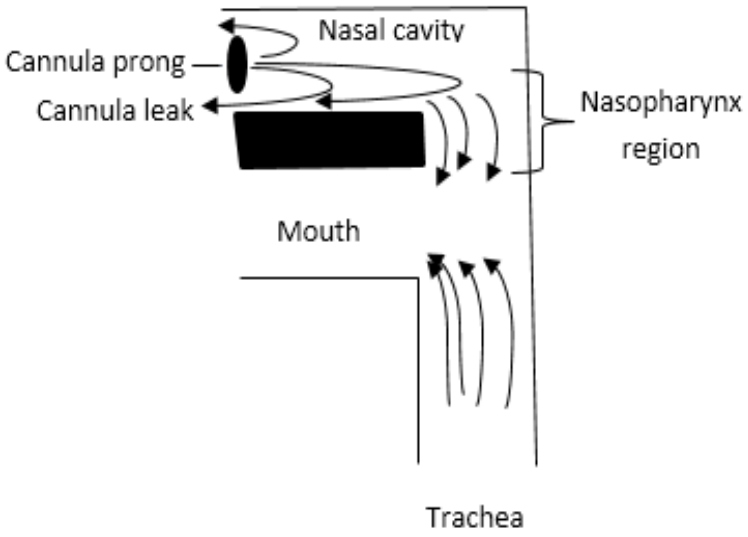

Fig. 3.13 Expiratory flow path during mouth open breathing

higher amounts of cannula flow will reach and exit the oral cavity. This explains the greater tracheal pressure (due to the small cannula) as the expiratory lung flow must interact with the cannula flow.

The inspiratory and expiratory airway resistance increase in an NHF dependent manner. In Table 3.2 and Table 3.3 it can be seen that the inspiratory resistance is consistently greater than the expiratory resistance. This can be attributed to the geometry of the UAM and NHF. The airway geometry in the inspiratory direction differs from the geometry in the expiratory direction. Ferris et al. (1960) measured the pressure flow characteristics of 6 spontaneously breathing male adults and found a greater inspiratory resistance. NHF was observed to cause a greater change in pressure over the same flow range in the inspiratory direction than in the expiratory direction (Fig. 3.7). During NHF administration, inspired flow from the atmosphere will require a greater pressure drop because of the relatively small area between the cannula prongs and the nostril. Also, there may be a further pressure drop due to the interaction of the cannula leak with the inspired flow. For both mouth state breathing (closed and open), K_1 increases monotonically with NHF but K_2 decreases with NHF. The uncertainty in the prediction of K_1 and K_2 is greater at NHF of 60 L/min as fluctuations in

tracheal pressure at NHF of 60 L/min was relatively greater. In consideration of the range of uncertainties, it appears that at any given NHF flow rate, K_1 and K_2 appear to be insensitive to cannula size.

In the neonate UAM (which is a closed mouth model) the OPT316 (the largest) produced a significantly greater inspiratory resistance at NHF of 9 L/min whilst OPT314 (the smallest) produced a greater expiratory resistance at all other NHF. On the basis of the amount of extrinsic positive end-expiratory pressure (ePEEP) that can be delivered at a greater NHF, the present results supports the recommendation by the manufacturers to use OPT316 for NHF in the range of 3-15 L/min.

On expiration, the breathing flow travels against cannula flow leading to more shear and higher turbulence (i.e. higher K_2 on expiration than inspiration): generally seen in Table 3.5 with some exceptions the quadratic Rohrer equation does not describe the pressure flow relationship well). However the values of K_1 during expiration and inspiration are comparable. In the adult UAM (mouth closed state) the opposite seems to hold (expiration has higher K_1 but lower K_2 than inspiration). Most of the difference is in the laminar term (K_1).

A resting neonate, about the same size as the neonate model will have a peak inspiratory flow of about 5 L/min (te Pas et al. (2009)). At this flow, its upper airway resistance will be 10.77 cmH2O/L/s (Table 5). A healthy 44 year old adult (the adult UAM) will have a resting peak inspiratory flow 30 L/min (Morris and Lane (1981)) which corresponds to an airway resistance of 2.5 cmH2O/L/s. Therefore at peak inspiratory flow rates, the neonatal airway resistance is about 4 times that of the adult model. This is not surprising as according to the Poiseuille's law for flow through a straight pipe ($Resistance = 8nl/\pi r4, wheren = viscosity, r = radius, l = length$), the resistance varies with $1/r^4$ for a laminar flow regime. It must be mentioned that the tracheal diameter of the adult model (at the mentioned peak flows) is 3 times that of the neonate and the Reynolds number (at the same point, and for the peak flows) is 1063 neonate model (trachea) and 2014 for the adult model (trachea). The

upper airway produces a quadratic relationship between flow and pressure (Eq. 3.1) because the flow in some regions of the airway (nasal valve for instance) is partly turbulent. Because of the relatively large tidal volume of adults compared to neonates, the work of breathing of an adult is expected to be greater than that of a neonate in spite of the observed lower resistance of th adult UAM. See chapter 4 for a comparison of neonatal and adult work of breathing.

3.5.1 Limitations

There are some limitations associated with this work. Measurements of resistance coefficients was limited to one individual adult and neonatal airway model. Upper airway geometry varies from one individual to another however the general shape is the same, as the range of Reynolds numbers. It is expected that the results presented in this chapter will vary quantitatively but agree qualitatively with results from other airway geometries.

The UAM lacks the mucosal layer and compliance which the biological upper airway possesses. Though changes in airway surface properties may affect flow via development of viscous forces, the thin mucosal layer present in the healthy individual is reported to produce little effect on flow (Clarke et al. (1970))

Also, a significant upper airway compliance may require an extra pressure drop but the small compliance of the upper airway ($\approx$ 3 ml/cmH_2O) (Mead (1969)) will exact a minimal pressure drop. It is plausible however that under conditions of high airway compliance and thick mucosal lining, the estimated upper airway resistance may disagree with those presented here.

3.6 Conclusion

The data presented here suggests that in mouth closed state, the large cannula effects a greater expiratory pressure than the small cannula during expiration (in inspiration, small

cannula pressure is greater). During mouth open breathing the small cannula produced a greater airway pressure than the large cannula. The disparities in airway pressure due to cannula size were significant at NHF60 (no error bar overlap). Mouth closed breathing produces approximately 3 times as much airway pressure as mouth open breathing at all NHF. Inspiratory airway resistance was found to be greater than expiratory resistance though both rise with NHF. In spite of the rise in inspiratory resistance with NHF, the concept of zero-pressure inspiration flow (ZPIF) (see Fig. 3.8) suggests a possible reduction in work of breathing due to effortless breathing at lower values of tracheal flow ($<$ ZPIF). At their respective peak inspired flow (neonate =5 L/min, adult =30 L/min), the neonatal airway resistance was found to be a factor of 4 greater than the adult airway resistance. In regards to the range of uncertainty values calculated in the estimation of K_1 and K_2, the influence of cannula size appears to be insignificant.

Chapter 4

How NHF may Affect Work of Breathing

4.1 Introduction

Individuals suffering from chronic airway disorders, mild obstructive sleep apnoea, acute hypoxemic respiratory failure and post-operative hypoxemia have been reported to benefit from nasal high flow (NHF) therapy (Porhomayon et al. (2016); Rea et al. (2010); Roca et al. (2010)). NHF involves the administration of warmed and humidified air, which may be enriched with more oxygen, at flow rates up to 60 L/min for adults and 8 L/min for neonates (Manley et al. (2013); Motojima et al. (2016); Ojha et al. (2013); Ward (2013)). The conditioned air is supplied to the patient via a breathing circuit connected to a nasal cannula.

Dysart et al. (2009) postulated some mechanisms of action of NHF and these included a reduction in mechanical work of breathing (WOB) - the muscular effort which drives breathing. Dysart et al. (2009) suggested that inspiratory WOB was reduced as NHF provides air flow, which supplies inspiratory flow without effort by the patient. However, NHF may raise expiratory WOB as the patient must expel air against the cannula jet.

Esophageal pressure is often measured as a surrogate for pleural pressure (Rubin et al. (2014); Saslow et al. (2006)). The standard method for the measurement of mechanical WOB is to compute the area under the pressure–volume loop, also known as Campbell diagram

(Pandit et al. (2001)). In Fig. 4.1, a pressure-volume loop, adapted from Saslow et al. (2006) is shown for the inspiratory and expiratory phases of a single breath cycle. The area of the dashed triangle (stored elastic energy) plus the area labelled rWOBi represent the WOB at the end of inspiration. rWOBi is the energy dissipated in overcoming inspiratory airway resistance. In a healthy state, expiration is passive, as part of the elastic energy is used to overcome expiratory airway resistance (rWOBe) (Cabello and Mancebo (2006); Otis et al. (1950); Saslow et al. (2006)). The overall energy (rWOB) dissipated in overcoming airway resistance equals the sum of rWOBi and rWOBe.

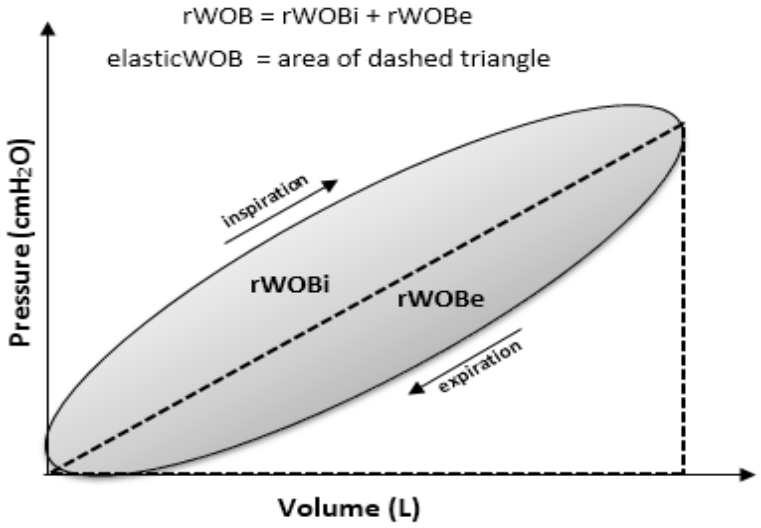

Fig. 4.1 Plot of pressure versus volume with bounded area indicating WOB

This method of finding work of breathing (as illustrated in Fig. 4.1) is known as planimetric analysis. In the presence of a resistive disease (increased inspiratory airway resistance e.g. pulmonary fibrosis), rWOBi will be greater relative to a healthy subject. In the presence of an obstructive disease (increased expiration airway resistance) e.g. COPD and asthma, rWOBe will be greater relative to a healthy subject. Rubin et al. (2014) and Willis et al. (2005) used the pressure-rate product as a surrogate for WOB under conditions of NHF in a population of neonates and children and reported a decrease in WOB due to NHF. By providing positive end expiratory pressure (PEEP) with a pressure support device, Graham et al. (2006) arrived at the same conclusion for children. A recent clinical study using electrical impedance

tomographic techniques has provided some evidence on the reduction of diaphragmatic electrical activity under the influence of NHF - suggesting in some sense, the 'offloading' of the diaphragmatic muscular effort during inspiration and hence a reduction in mechanical work of breathing Pham et al. (2014). To date, evaluation of WOB has been limited to the inspiratory breathing phase (Pham et al. (2014); Rubin et al. (2014); Saslow et al. (2006)). It is reasonable to expect that breathing out against an NHF jet through the open area of the nares when the cannula is in place will require more effort than when NHF is absent. The resistance of the upper airway, from the nares to the trachea constitutes about two-thirds of the total airway resistance (Ferris et al. (1960)). In Chapter 3, the upper airway resistances of an anatomically representative rigid model of an adult and a neonate were measured under NHF conditions. In this chapter, the WOB model proposed by Otis et al. (1950) is refined by incorporating clinically observed changes in respiratory parameters during the administration of NHF. The refined model is then used to predict the changes in resistive WOB (rWOBi and rWOBe) due to NHF.

4.1.1 Chapter nomenclature

$\mathbf{A}_i$ - inspiratory flow amplitude

$\mathbf{A}_e$ - expiratory flow amplitude

CV - coefficient of variation

I:E ratio - ratio of inspiratory time to expiratory time

$\mathbf{K}_{el}$ - lung elastance **MCB** - mouth closed breathing

MOB - mouth open breathing

MV - minute volume

PEF - peak expiratory flow

PIF - peak inspiratory flow

RR - respiratory rate

rWOB - resistive work of breathing

rWOBe - expiratory resistive work of breathing

rWOBi - inspiratory resistive work of breathing

rWOBzt - work of breathing during zero-therapy

St.D - standard deviation

$\mathbf{T}_i$ - inspiratory time

$\mathbf{T}_e$ - expiratory time

$\mathbf{V}_t$ - tidal volume

WOB - work of breathing

ZT - zero therapy (no therapy)

ZPIF - zero pressure inspiratory flow

δ**ZT (%)** - percentage change in rWOB due to NHF

4.2 Work of Breathing Model Setup

Due to a lack of clinical data (which is necessary for planimetric analysis), a mathematical derivation of WOB based on known equations which govern lung and airway mechanics will be explored to examine the influence of NHF on WOB. Here, a basic assumption is made that the flow wave is sinusoidal - this simplifies the computations involved but preserves the generality of the conclusions to any flow pattern as the model is not history-dependent. Fig. 4.2 shows a sinusoidal waveform with amplitude, A, and period, T, representing the flow waveform.

The mathematical representation of the sinusoid is presented in Eq. 4.1. In this work, the period of positive flow rate is inspiration, and negative flow rate is expiration. Note that by assuming a sinusoid, an inherent assumption is made that I:E ratio equals unity. A method for incorporating a more physiologically correct value of I:E ratio will be presented later in this work. The tidal volume (V_t) equals the area under the inspiratory or expiratory portion of the flow waveform and can be found by direct mathematical integration of Eq. 4.1 from 0

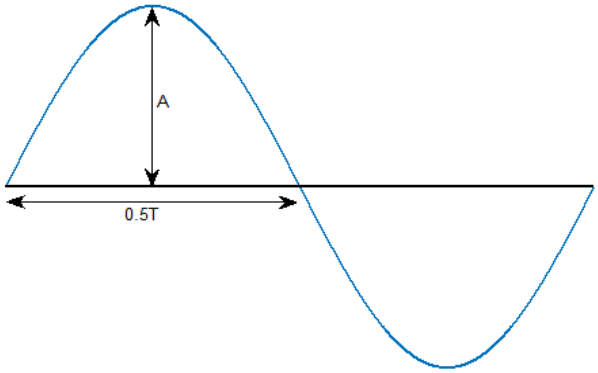

Fig. 4.2 Sinusoidal signal representing the breathing flow waveform

to t = 0.5T (see Eq. 4.2 which also describes the relationship between the flow amplitude (A), period (T) and tidal volume, V_t).

$$F = A\sin(\frac{2\pi t}{T}) \tag{4.1}$$

$$V_t = \int_0^{0.5T} F\,dt = \frac{AT}{\pi} \tag{4.2}$$

$$P = K_{el}V_t + K_aF + K_bF^2 \tag{4.3}$$

Eq. 4.3 describes the pressure required to overcome lung elastance (resistance of the lungs to inflation) and the resistance of the airway to air flow (second and third terms of Eq. 4.3). In Eq. 4.3, K_{el} represent elastance of the lungs and K_a and K_b are the resistance coefficients of the entire airway, upper plus lower. Since the upper and lower airways are coupled in series, the total airway resistance must be equal to their sum i.e. $K_a = K_1 + K_m$ and $K_b = K_2 + K_n$ where K_m and K_n are the laminar and turbulent resistance coefficients of the lower airways and K_1 and K_2 are those of the upper airway.

The lower airway resistance consists of a principally laminar pressure loss due to flow. The pressure loss due to flow, being largely laminar due to low Reynolds number, is the same whether NHF is applied or not (losses are linear with flow, so integrated work over a given volume passed is the same whether breathing a short fast flow or long slow flow if the patient breathes the same MV). Only the pressure required to produce flow through the upper airway during inspiration and expiration is relevant to the present work.

The pressure (P_{UA}) required to produce flow through the upper airway during inspiration, (iP_{UA}), is described by Eq. 4.4 and that for expiration, (eP_{UA}), is described by Eq. 4.5. iK_1 and iK_2 (Eq. 4.4) are the resistance coefficients of the upper airway during inspiration and eK_1 and eK_2 (Eq. 4.5) are the expiratory upper airway resistance coefficients.

$$iP_{UA} = iK_1 + iK_2F^2 \tag{4.4}$$

$$eP_{UA} = eK_1 + eK_2F^2 \tag{4.5}$$

Given the breath-by-breath variability in tidal volume, which Tobin et al. (1983) estimated to be 33 ± 14.3 % for 47 healthy young adults (mean age = 28.6 years), the WOB averaged over a minute (work rate, WOB/min) was thought to be a better representation of the influence of NHF on respiratory effort. Mathematically, the area under the upper airway pressure-volume curve is equivalent to the integral shown in Eq. 4.6 which when solved, yields Eq. 4.7. The product of Eq. 4.7 and the respiratory rate (RR) (number of breaths per minute) yields Eq. 4.8 – which was first presented by Otis et al. (1950). By replacing K_1 and K_2 in Eq. 4.8 with the inspiratory and expiratory upper airway resistance coefficients, Eq. 4.9 is obtained. Eq. 4.9 represents work done over a minute (expressed in J/min) in overcoming the inspiratory and expiratory upper airway resistance by the close of the breathing cycle - denoted as rWOB.

$$WOB = \int_0^{0.5T} P_{UA} dV = \int_0^{0.5T} P_{UA} F dt \tag{4.6}$$

$$WOB = 0.25 K_1 RR(\pi V_t)^2 + 0.67 K_2 \pi^2 RR^2 (V_t)^3 \tag{4.7}$$

$$WOB/min = 0.25(K_1)(\pi RRV_t)^2 + 0.67(K_2)\pi^2 (RRV_t)^3 \tag{4.8}$$

$$\begin{aligned} rWOB = {} & 0.25 iK_1(\pi RRV_t)^2 + 0.67(iK_2)\pi^2 (RRV_t)^3 + \\ & 0.25 eK_1(\pi RRV_t)^2 + 0.67 e(K_2)\pi^2 (RRV_t)^3 \end{aligned} \tag{4.9}$$

The product of RR and V_t is the minute volume (MV). It can be seen (from Eq. 4.9) that the work required to overcome airway resistance depends in part on MV. Nasal high flow therapy has been widely reported to reduce RR but its effect on tidal volume (V_t) and MV is complicated by disease state (Bräunlich et al. (2013)) and wakefulness (Mündel et al. (2013)). The effect of NHF on I:E ratio has been investigated by Fraser et al. (2016) whose results were used to infer how variation in I:E ratio might affect rWOB.

In what follows, rWOB for three categories of subjects are explored based on changes in RR and V_t. These include subjects in whom (1) RR and V_t do not change (2) RR and V_t change but I:E ratio is constant (3) RR, V_t and I:E ratio change with NHF. The values of K_1 and K_2 obtained for the adult and neonate upper airway models for varying NHF, cannula sizes and mouth states (opened or closed) - see Chapter 3 (Tables 3.2, 3.3 and 3.5) - will be used in the present Chapter. As a model for rWOB (during NHF) is being developed, only the inspiratory and expiratory resistance coefficients of the adult upper airway model for mouth closed state (with NHF delivered via the medium cannula) will be used.

4.2.1 Subject in whom RR and V_t do not change

The Otis equation (Eq. 4.9) was used to compute rWOB for the adult upper airway model (see Chapter 3, Figure 1) without NHF (zero-therapy, ZT) and with NHF of 20 L/min (NHF20), 40 L/min (NHF40) and 60 L/min (NHF60) administered during mouth close breathing. Here, rWOB was calculated using the RR and V_t of a resting young adult i.e. 15 bpm and 0.5 L respectively (Gisolf et al. (2004); Tobin et al. (1989)). The percentage change in rWOB due to NHF was calculated using the formula: δZT (%) = $100(rWOBnhf - rWOBzt)/rWOBzt$ where $rWOBnhf$ is the rWOB during NHF and $rWOBzt$ is the rWOB at ZT. The percentage change in rWOB for NHF delivered via the medium cannula is shown in Table 4.1. Notably, rWOB increases with NHF.

Table 4.1 Summary of results of rWOB using the Otis equation

NHF (L/min)	**NHF20**	**NHF40**	**NHF60**
δ**ZT (%)**	24.54	66.54	93.40

Whilst the prediction made by the Otis equation makes sense as both inspiratory and expiratory airway resistance were found to increase with NHF (see Tables 3.2 and 3.3, Chapter 3), the Otis equation fails to capture the identified effect of zero-effort required to inspire at flows below the zero-pressure inspiratory flow (ZPIF) (discussed in Chapter 3 and re-illustrated here in Fig. 4.3). For the sinusoidal flow waveform being used (Fig. 4.2) the half-sinusoid (Fig. 4.3) represents the inspiratory flow waveform and the horizontal lines represent the ZPIF at NHF20, NHF40 and NHF60. By considering NHF20 for instance, at the start of inspiration up to a flow rate of q L/min, no respiratory effort will be required to overcome upper airway resistance but only that needed to overcome lower airway resistance and lung elastance, which will be same as in spontaneous breathing. Therefore between times, t = 0 and t = a , respiratory effort is reduced. Respiratory effort is generated to overcome upper airway resistance for flows between q L/min and r L/min followed by another period effortless breathing between time t = b to t = total inspiratory time (T_i).

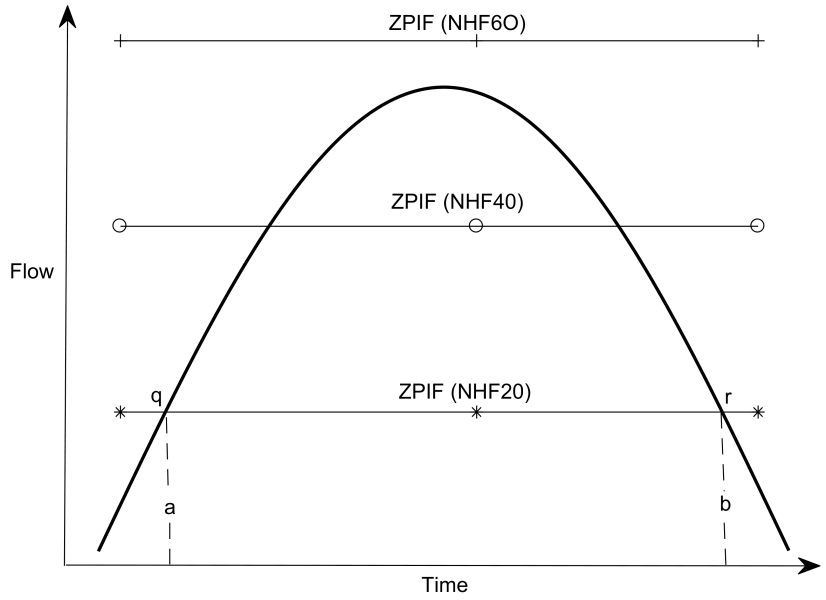

Fig. 4.3 Plot of sinusoidal inspiratory flow illustrating the ZPIF for NHF20, NHF40 and NHF60

This emphasizes the need to refine Otis' approach to more accurately predict rWOB under the influence of NHF. In the refinement of the Otis approach (Eq. 4.9), the integral shown in Eq. 4.6 was performed over the time interval between **a** and **b** as shown in Eq. 4.10.

$$WOB = \int_a^b P_{UA} dV = \int_a^b P_{UA} F dt \tag{4.10}$$

The ZPIF for mouth close breathing at NHF20, NHF40 and NHF60 were found to be 7.4, 16.5 and 24.8 L/min respectively (Chapter 3). Time **a**, can be found from the ZPIF using Eq. 4.11. Time **b** is simply the difference between inspiratory time, T_i and **a** for a symmetrical flow pattern such as a sinusoid. This modification of the Otis model will be referred to as Model 1.

$$t = \left(\frac{T}{2\pi}\right) arcsin\left(\frac{ZPIF}{A}\right) \tag{4.11}$$

Note that at time $0 < t < \mathbf{a}$ and $\mathbf{b} < t < T_i$, i.e. at $F < ZPIF$, the tracheal pressure required to drive inspiration is positive with respect to atmosphere. The diaphragm and intercostal contraction yields negative pressure with respect to atmosphere (measured with respect to atmosphere because atmospheric pressure acts on the outside of the chest wall). A negative tracheal pressure requires muscular effort. A positive tracheal pressure requires no muscular effort, and in fact the air is doing work on the chest (but this requires no expenditure of calories in the muscles, and they cannot recoup energy by work being done on them).

Fig. 4.4 shows percentage changes in rWOB obtained using Model 1, which has been juxtaposed with findings from the Otis Eq. (Table 4.1). It is noticeable that Model 1 predicts a lower rWOB. NHF60 produces rWOB which is less than rWOB at ZT and it is partly due to the effortless inspiratory breathing at NHF60 (as the ZPIF at NHF60 is greater than the peak inspiratory flow).

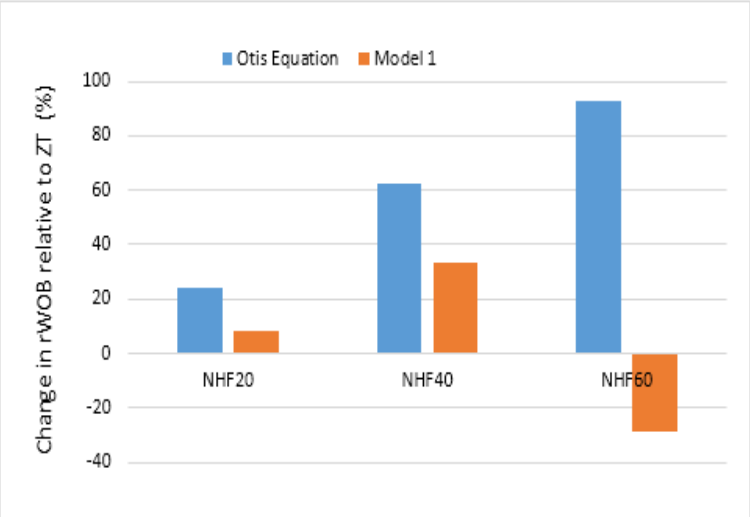

Fig. 4.4 Comparison of result of the rWOB predicted the Otis Equation and Model 1.

Up to this point, rWOB has been computed with a flow signal which is a perfect sinusoid – which implies that the inspiratory time (T_i) is equal to the expiratory time (T_e) – I:E ratio is unity - and that the peak inspiratory flow (PIF) is equal to the peak expiratory flow (PEF). This assumption is not realistic. Physiologically, the T_i is lesser than T_e whilst PIF is greater than PEF during resting state breathing (Tobin et al. (1983)). These effects can be included

by concatenating two sinusoids of different periods and amplitudes such that the rising phase of one (Fig. 4.5, plot A) represents inspiration and the falling phase of the other (Fig. 4.5, plot B) represent expiration as shown in Fig. 4.5, plot C. When a particular I:E ratio (T_i/ T_e) is specified, Eq. 4.12 can be used to compute T_i and T_e as long as the period of the entire flow waveform, T, is also given.

$$T_e = \frac{T}{I:Eratio+1}; T_i = T - T_e \tag{4.12}$$

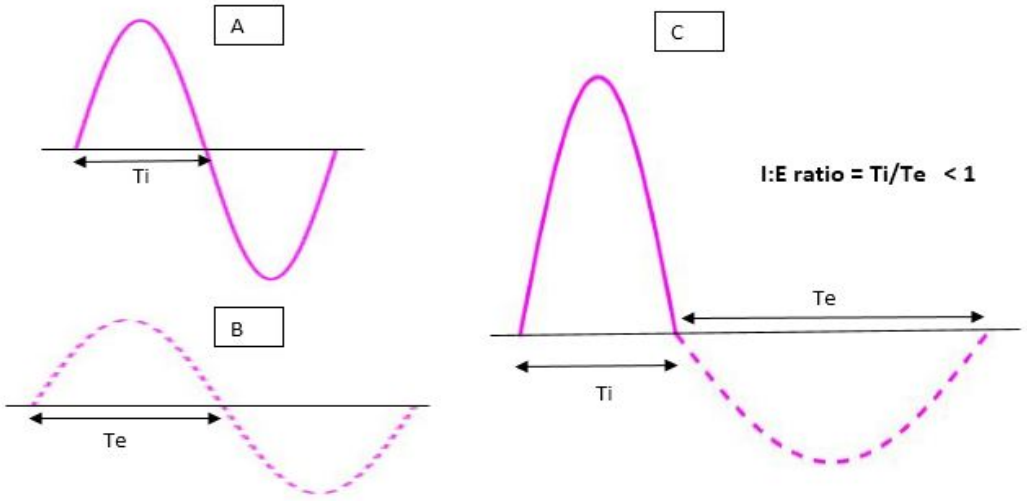

Fig. 4.5 Plot showing the concatenation of two sinusoids of different periods and amplitudes to define a more realistic breathing waveform

By using the relationship between amplitude, tidal volume (V_t) and period shown earlier (see Eq. 4.2), the inspiratory phase amplitude (A_i), will be equivalent to $V_t\pi/2T_i$ and in a like manner, that of the expiratory phase (A_e) will be $V_t\pi/2T_e$ – noting that inspired volume is same as expired volume. In summary, a breathing waveform has been defined (Fig. 4.5, plot C) such that by specifying three parameters i.e. I:E ratio, period, and tidal volume, the T_i, T_e, A_i and A_e can be modulated in a more physiologically correct way. Herein, this modification incorporated into Model 1 will be referred to as Model 2. Using Model 2, the effect of NHF on rWOB, re-evaluated using I:E ratio of 0.74 - measured average of 47 young adults (mean

age = 28.6 years) by Tobin et al. (1983). Table 4.2 contains the rWOB and percentage change relative to ZT ($\delta ZT(\%)$) computed using Model 2.

Table 4.2 rWOB results using Model 2

NHF (L/min)	**NHF0 (ZT)**	**NHF20**	**NHF40**	**NHF60**
rWOB (J/min)	0.86	1.06	1.32	1.13
δZT (%)	-	24.54	66.54	93.40

Fig. 4.6 represents a summary of the progression of results obtained so far, starting with the Otis equation (PIF = PEF, I:E ratio = 1) followed by Model 1 (ZPIF effect included but I:E ratio = 1) and finally a definition of an adjustable waveform, Model 2 (PIF $\neq$ PEF, I:E ratio 0.74). Note that the inclusion of a more realistic I:E ratio produces an increase in

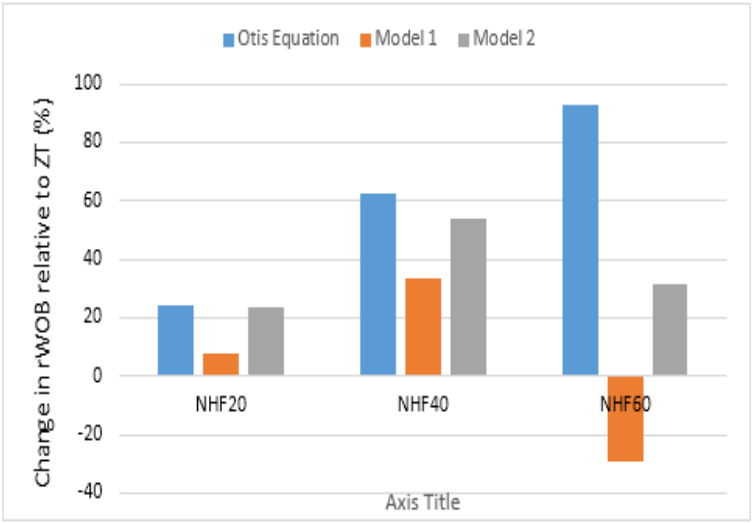

Fig. 4.6 Plots of WOBr for MCB comparing results of the Otis equation, Model 1 and Model 2

rWOB. This makes sense because I:E ratio less than unity means a shorter T_i and a longer T_e which in turn produces a greater peak inspiratory flow (PIF) and a lesser expiratory flow amplitude because V_t must be preserved. Note that the effect of the rising inspiratory flow amplitude overbalances the effect of falling peak expiratory flow (PEF) because the ZPIF effect is not applicable to the expiratory flow. It is concluded that rWOB rises with NHF if MV remains unchanged and the Otis equation can be used as a first approximation of rWOB for lower NHF (up to and including 20 L/min) under this condition (constant MV)

4.2.2 Subject in whom RR and V_t change with NHF

The observed respiratory response to NHF where there is a fall in RR (Corley et al. (2011); Riera et al. (2013); Sztrymf et al. (2011)) a rise in V_t (Corley et al. (2011); Riera et al. (2013)) but a general fall in MV (Bräunlich et al. (2013)) was considered. Bräunlich et al. (2013) reported that 20 L/min NHF reduced MV by approximately 1 L in 15 patients suffering from COPD (mean age = 67.7 years). Corley et al. (2011) studied 20 COPD patients (mean age = 65 years), who were prescribed 50 L/min NHF, and observed a 3.4 bpm reduction in RR. Based on these observations, MV was reduced by 1 L for every 20 L/min of NHF and RR was reduced by 3.4 bpm for every 50 L/min NHF. Though a waveform with adjustable I:E ratio has been defined, so far the assumption has been made that I:E ratio is not affected by NHF so its value of 0.74 (Tobin et al. (1983)) will be constant in this section. A mathematical expression which relates NHF to RR, MV and V_t such that an increase in NHF will reduce RR, increase V_t but decrease MV was found. This was done by defining the NHF-induced MV and V_t as linear functions of NHF (according to the clinical findings mentioned above) of the forms respectively shown in Eq. 4.13 and Eq. 4.14. M, as defined by Eq. 4.15 is the modifying function that reduces RR and increases V_t when NHF is applied. The parameters that define M are shown in Table 4.3.

$$MV = \left(\frac{1}{20}nhf + 7.5\right) \tag{4.13}$$

$$V_t = M(nhf) + V_{tZT} \tag{4.14}$$

$$M = -\left(\frac{1}{nhf}\right)\left(\frac{-dMV\frac{nhf}{nhf_{dMV}} + MV_{ZT}}{-dRR\frac{nhf}{nhf_{dRR}} + RR_{ZT}} - V_{ZT}\right) \tag{4.15}$$

The inclusion of these NHF-dependent adjustments in MV and V_t to Model 2 defines another model herein referred to as Model 3. The breathing flow predicted by Model 3 for ZT, NHF20, NHF40 and NHF60, assuming a constant I:E ratio (0.74) have been presented in

Table 4.3 Parameters defining modifying function, M

Symbol	Name	Value
nhf	nasal high flow	variable
dMV	change in MV	1 (L/min)
$\mathbf{nhf}_{dMV}$	NHF @ change in MV	20 (L/min)
$\mathbf{MV}_{ZT}$	MV @ ZT	7.5 (L/min)
dRR	change in RR	3.4 (bpm)
$\mathbf{nhf}_{dRR}$	NHF @ change in RR	50 (L/min)
$\mathbf{RR}_{ZT}$	RR @ ZT	15 (bpm)
$\mathbf{Vt}_{ZT}$	V_t @ ZT	0.5 (L)

Fig. 4.7, where RR falls (period rises) and V_t rises with NHF. The ZPIF corresponding to the applied NHF are also indicated.

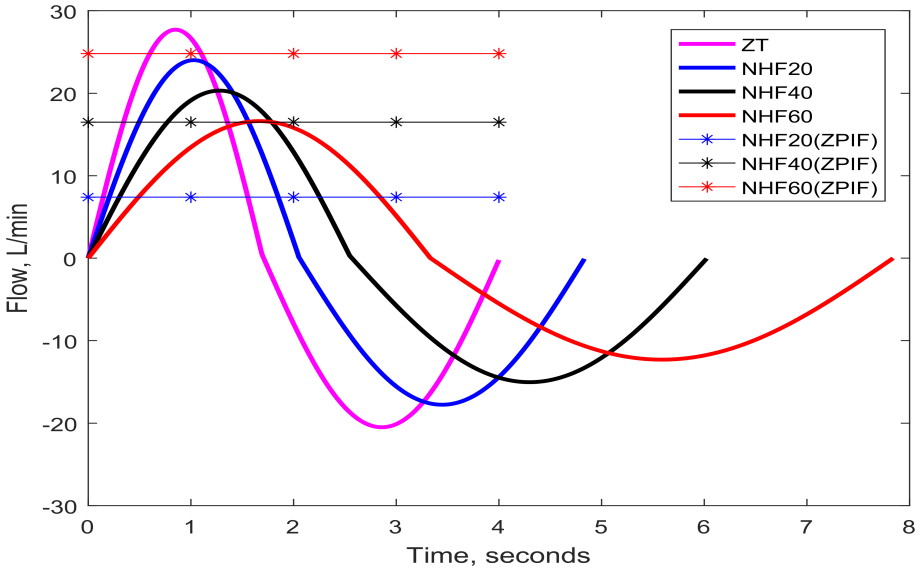

Fig. 4.7 Flow signals respectively representing ZT and NHF breathing at NHF20, NHF40, and NHF60 with NHF-adjusted MV

The percentage changes in rWOB relative to ZT, as predicted by Model 3 for NHF20, NHF40 and NHF60 are shown in Table 4.4. It is noticeable that Model 3 predicts a lower rWOB during NHF relative to rWOB at ZT. It is concluded that NHF increases rWOB when MV remains unchanged but it produces a significant fall in rWOB when MV falls. This is partly due to the ZPIF flow effect. Also, a fall in minute volume means a reduced V_t or RR

Table 4.4 rWOB results predicted by Model 3

NHF (L/min)	NHF0 (ZT)	**NHF20**	**NHF40**	**NHF60**
rWOB (J/min)	0.86	0.71	0.53	0.14
δ**ZT (%)**	-	-17.04	-38.64	-83.75

or both, either of which requires lower muscular activity (lower muscular contraction for reduced V_t and lower rate of muscular contraction for reduced RR).

4.2.3 Subject in whom RR, Vt and I:E ratio change

Fraser et al. (2016) found that administering NHF of 30 L/min caused a reduction in I:E ratio of about 13 % in 30 males. This is the only report of I:E ratio variation with NHF to date and was thus used to scale the I:E ratio with NHF (13 % fall in I:E ratio for every 30 L/min NHF) – defined by Eq. 4.16

$$IEratio = -0.0032nhf + 0.74 \tag{4.16}$$

The inclusion of NHF-induced I:E ratio in Model 3 defines Model 4. According to Eq. 4.16, NHF20, NHF40 and NHF60 will respectively reduce I:E ratio by 8.6 % , 17.3 % and 26 %. The rWOB and percentage change in rWOB relative to ZT as predicted by Model 4 is shown in Table 4.5. Fig. 4.8 compares the percentage changes in rWOB predicted by Model 3 to that of Model 4 during NHF. It is noticeable that Model 4 predicts a greater rWOB relative to Model 3 for all NHF except NHF60. This happens because the peak inspiratory flow (PIF) rises and peak expiratory flow (PEF) falls with I:E ratio to preserve V_t. Note that the rise in PIF due to a fall in I:E ratio is greater than the corresponding fall in PEF. Consequently, the energy loss due to the rise in PIF outweighs that due to the fall in PEF. The ZPIF however remains greater than the PIF at NHF60 in spite of the fall in I:E ratio so the energy required for inspiration remains zero whilst energy is saved due to the fall in PEF.

In summary, the rWOB for a situation where NHF is administered via the medium cannula has been investigated for close mouth breathing in the adult UAM by incorporating

Table 4.5 rWOB predicted by Model 4 for NHF20, NHF40 and NHF60

NHF (L/min)	NHF0 (ZT)	**NHF20**	**NHF40**	**NHF60**
rWOB (J/min)	0.86	0.77	0.66	0.09
δZT (%)	-	-9.61	-22.93	-89.42

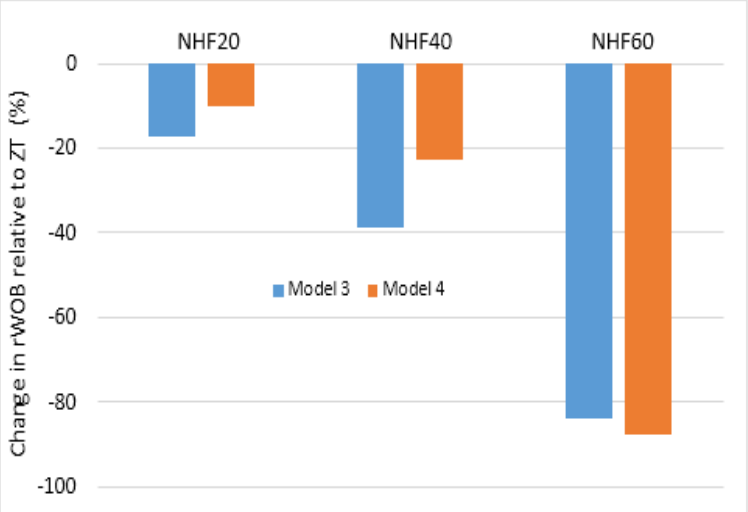

Fig. 4.8 Percentage reduction in rWOB: Model 3 vs. Model 4

clinically observed changes in breathing characteristics sequentially into the Otis' equation. This process produced four Models for computing rWOB with Model 4 being the most comprehensive. A flow chart summarizing the characteristics of each of the four models is shown in Fig. 4.9 with the key additions highlighted.

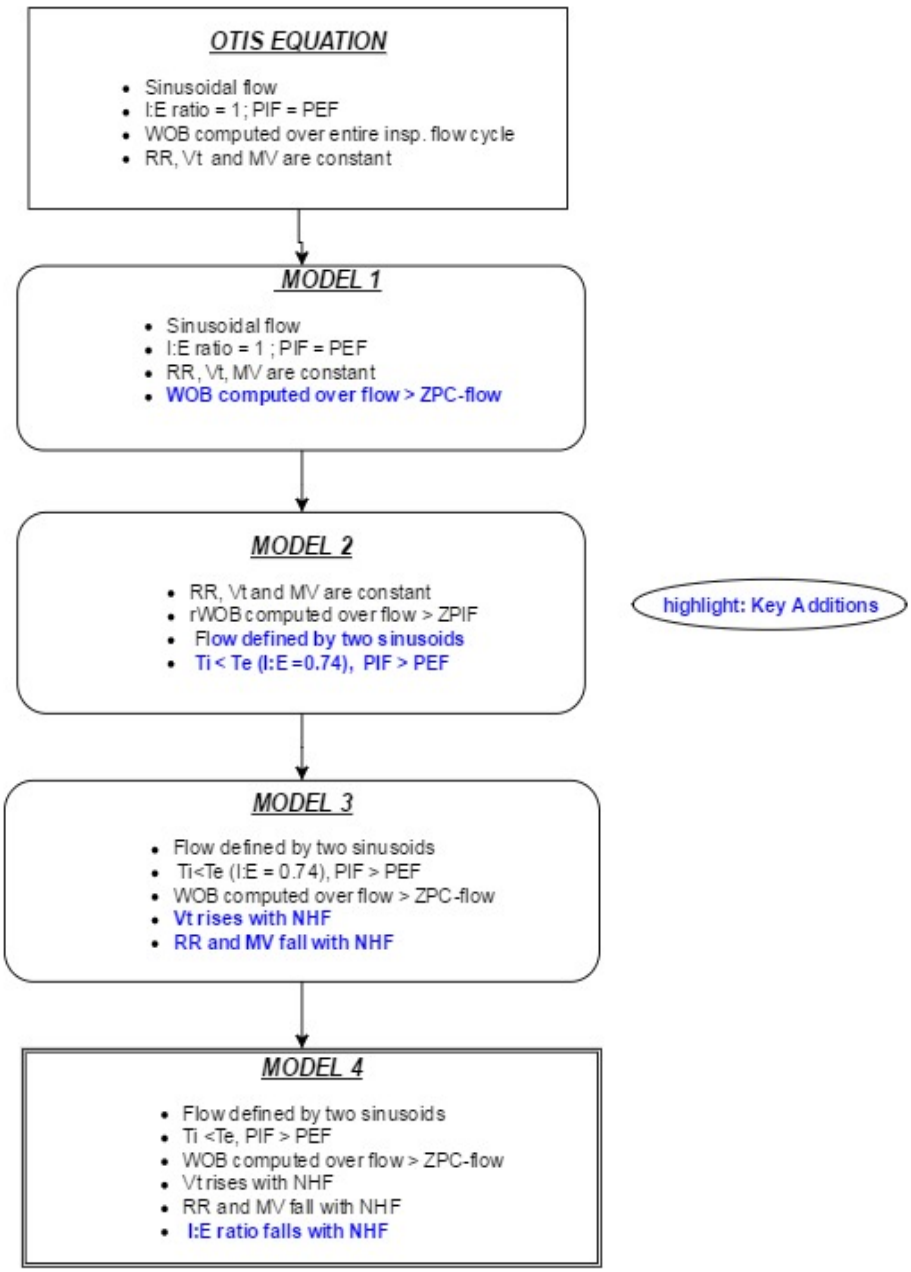

Fig. 4.9 Flow chart summarizing the rWOB Models

4.3 Results

4.3.1 I:E ratio effect

On Fig. 4.10, the dashed lines represent flow waveforms predicted by Model 4 (MV and I:E ratio reduces with NHF) and the continuous lines are those derived using Model 3 (MV reduces with NHF, I:E ratio is constant). The ZPIF for NHF20, NHF40 and NHF60 are also indicated. Reducing I:E ratio raises the PIF and lowers PEF.

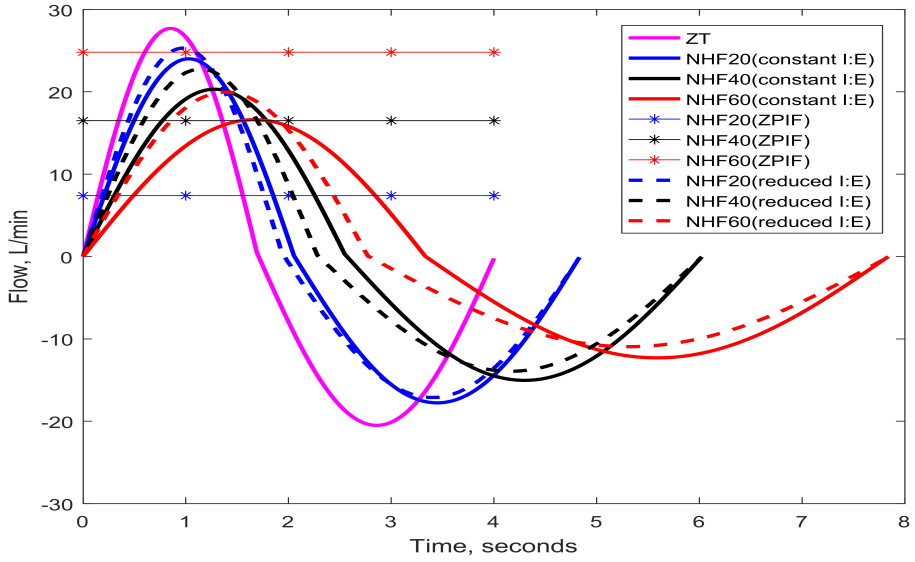

Fig. 4.10 Plots showing the effect of I:E ratio on PIF, PEF and period

At NHF60, the ZPIF remains greater than the PIF in spite of the changes in I:E ratio therefore inspiration will remain effortless and expiration will be relatively easier because of the fall in PEF. For NHF to reduce rWOB via changes in I:E ratio, it must affect the breathing flow characteristics in a way that raises the ZPIF above the PIF. Fig. 4.11 shows the changes in rWOB and PIF as I:E ratio increases at NHF60. I:E ratio is expressed as a percentage of the I:E ratio at ZT (I:Ezt) i.e. 100 % on the horizontal axis. The ZPIF for NHF60 i.e. 24.8 L/min is also indicated. It is noticeable that rWOB rapidly rises as I:E ratio falls below 60 % of I:Ezt but rWOB rises gently as I:E ratio rises above 60 % of I:Ezt. This is because below

60 % of I:Ezt, ZPIF (24.8 L/min) becomes lesser than the PIF. It can be concluded that the optimum value of I:E ratio in regards to a lower rWOB is around 60 % of I:Ezt.

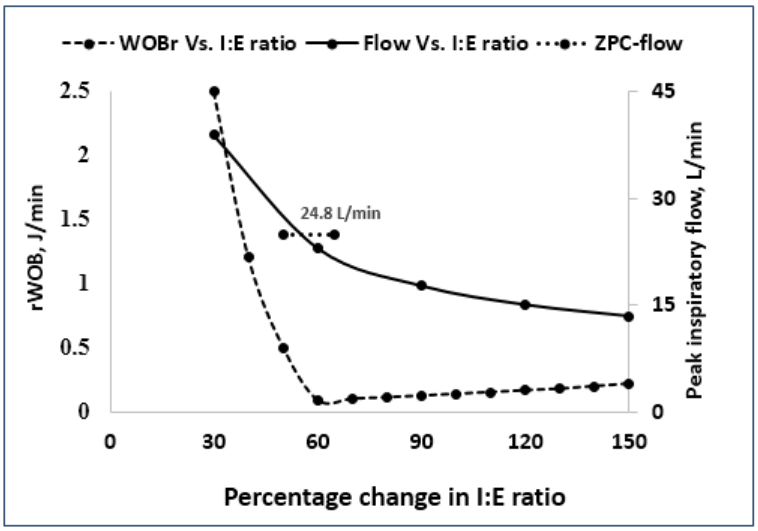

Fig. 4.11 Plot of changes I:E ratio with WOBr and PIF for mouth close breathing at NHF60

4.3.2 rWOB: mouth open versus closed state

So far the results presented have been obtained using the resistance coefficients derived from the adult upper airway model in mouth closed breathing (MCB) state with NHF administered via the medium cannula. The trends and conclusions reached are generally applicable to the small and large cannula. Measurement of RR amongst 18 healthy participants made by Ritchie et al. (2011) indicated that the RR during mouth open breathing (MOB) does not fall as much as it does during MCB, though a possible decrease in MV was intimated. The authors however did not measure variations in tidal volume. Information on the effect of MOB on MV under NHF conditions is lacking. In a report on the effect of mouth flow leakage on tidal volume and airway resistance during the administration of variable positive airway pressure therapy (VPAP), Tuggey et al. (2007) observed a decrease of about 12 % in tidal volume upon a switch from MOB to MCB. A direct comparison between VPAP and NHF is however untenable.

In what follows, the assumption was made that changes in V_t, RR and I:E ratio during MCB and MOB are the same. Model 4 was then used to estimate rWOB during MOB. The resistance coefficients as presented in Chapter 3 were used. The error propagated in rWOB estimates, drWOB, due to uncertainties in the estimation of the resistance coefficients (dK_1 and dK_2) (see Chapter 3) is defined by Eq. 4.17 which reduces to Eq. 4.18 when the equation for rWOB (Eq. 4.10) is substituted and further simplified.

$$drWOB = \frac{\partial d(rWOB)}{\partial dK_1} dK_1 + \frac{\partial d(rWOB)}{\partial dK_2} dK_2 \tag{4.17}$$

$$drWOB = \frac{d}{dK_1}\Big(\int_a^b K_1 \sin^2 T dt\Big) dK_1 + \frac{d}{dK_2}\Big(\int_a^b K_2 \sin^3 T dt\Big) dK_2 \tag{4.18}$$

To compute the uncertainty propagation error for inspiratory rWOB, T in Eq. 4.18 was replaced with T_i and dK_1 and dK_2 were respectively replaced with the uncertainties found for the estimates of inspiratory K_1 and K_2 in Chapter 3. The same was done for expiration. The uncertainty propagation error for total rWOB equals the sum of the inspiratory and expiratory propagation errors. Fig. 4.12 shows a superimposed plot of the rWOB values for MCB and MOB. MOB requires less muscular effort than MCB though rWOB for MCB and MOB are close at NHF60. The error bars represent the uncertainty propagation error (computed with Eq. 4.18) produced by the uncertainty in the estimation of the resistance coefficients (Chapter 3).

In Fig. 4.13, it can be seen that MOB at NHF20 and NHF40 cause a greater percentage fall in rWOB relative to ZT than MCB but lesser at NHF60. The inspiratory rWOB (iWOB), expiratory rWOB (eWOB) and breath cycle rWOB (tWOB) for both MCB and MOB have been presented in Table 4.6. The average (AVG) rWOB at a particular NHF, defined as the sum of the rWOB of the small, medium and large cannula divided by three is shown in Table 4.6, with the standard deviation (St.D) of these three values presented in brackets. Also, the coefficient of variation (CV) – defined as $\frac{standarddeviation}{averagerWOB}$ is also shown. This also indicates

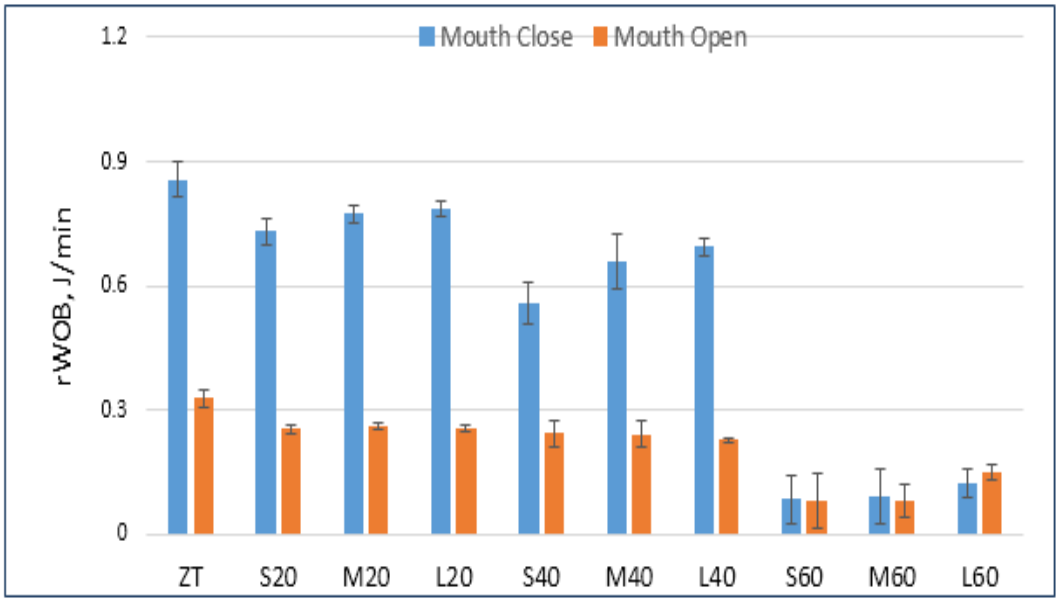

Fig. 4.12 Plots showing the effect of cannula size and breathing state (MCB or MOB) on rWOB. S20 indicate NHF20 via the small cannula. M and L respectively represent medium and large cannula. Error bars represent uncertainty propagation error in rWOB due to uncertainty in estimation of resistance coefficients.

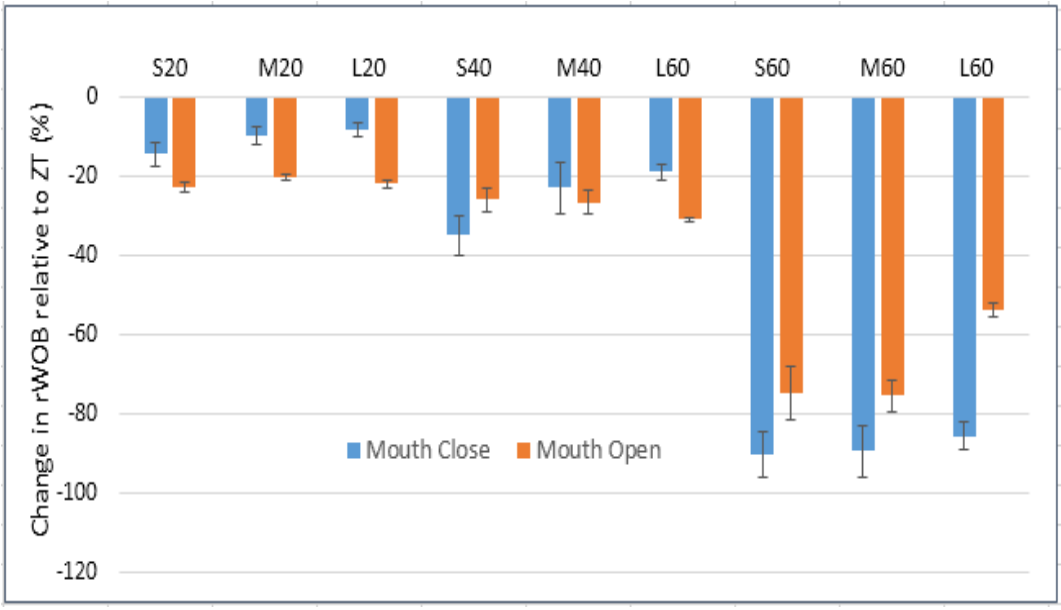

Fig. 4.13 Plot showing the percentage fall in rWOB due to NHF relative ZT for MCB and MOB. S20 indicate NHF20 via the small cannula. M and L respectively represent medium and large cannula

variability in rWOB due to cannula size. The uncertainty propagation errors in the estimation of rWOB due to uncertainties in the estimation of the resistance coefficients have also been presented along with the changes in rWOB relative to ZT (δZT (%)).

4.3.3 Effect of cannula size on rWOB

In Fig. 4.12, it is seen that for both MCB and MOB, changes in rWOB between the medium and large cannula are insignificant (due to overlap of error bars) but significant between the large and small cannula especially at NHF20 and NHF40. The coefficient of variation (standard deviation/average) (in Table 4.6) rises with NHF for MCB and MOB (falls at NHF60). In Chapter 3 it was observed that the error in tracheal pressure at NHF60 was greater pressure.

Table 4.6 Inpiratory, expiratory and cycle rWOB computed for ZT, NHF20, NHF40 and NHF60 during MCB and MOB. S20, M20, L20 respectively denote NHF20 via the small, medium and large cannula

Mouth Closed Breathing (MCB)

	iWOB	**eWOB**	**tWOB**	**Error**	δZT **(%)**
ZT	0.615	0.241	0.855	0.042	-
S20	0.574	0.158	0.732	0.031	14.5
M20	0.582	0.192	0.773	0.022	-9.6
L20	0.584	0.202	0.785	0.018	-8.2
AVG.	**0.580**	**0.184**	**0.763**	**0.024**	**-10.80**
(St.D)	**(0.005)**	**(0.023)**	**(0.028)**	**(0.007)**	**(3.30)**
CV			**3.7%**		
S40	0.448	0.109	0.557	0.051	-34.80
M40	0.498	0.161	0.659	0.067	-22.90
L40	0.532	0.162	0.694	0.020	-18.80
AVG.	**0.493**	**0.144**	**0.637**	**0.046**	**-25.50**
(St.D)	**(0.042)**	**(0.030)**	**(0.071)**	**(0.024)**	**(8.30)**
CV			**11.10 %**		
S60	**0.000**	**0.084**	**0.084**	**0.059**	**-90.20**
M60	**0.000**	**0.091**	**0.091**	**0.066**	**-89.40**
L60	**0.000**	**0.124**	**0.124**	**0.034**	**-85.60**
AVG.	**0.000**	**0.099**	**0.099**	**0.053**	**-88.40**
(St.D)	**(0.000)**	**(0.021)**	**(0.021)**	**(0.017)**	**(2.50)**
CV			**21.20 %**		

Mouth Open Breathing (MOB)

	iWOB	**eWOB**	**tWOB**	**Error**	δZT **(%)**
ZT	0.241	0.087	0.328	0.022	-
S20	0.191	0.063	0.254	0.012	-22.60
M20	0.197	0.065	0.261	0.009	-20.30
L20	0.191	0.065	0.256	0.009	-21.90
AVG	**0.193**	**0.064**	**0.257**	**0.010**	**-21.60**
(St.D)	**(0.096)**	**(0.032)**	**(0.129)**	**(0.005)**	**(10.84)**
CV			**5.0 %**		
S40	0.158	0.085	0.243	0.030	-25.80
M40	0.158	0.083	0.241	0.031	-26.60
L40	0.153	0.073	0.227	0.005	-30.80
AVG	**0.157**	**0.080**	**0.237**	**0.022**	**-27.7**
(St. D)	**(0.078)**	**(0.041)**	**(0.119)**	**(0.016)**	**(14.10)**
CV			**50 %**		
S60	0.000	0.083	0.083	0.066	-74.70
M60	0.000	0.081	0.081	0.041	-75.40
L60	0.086	0.065	0.151	0.019	-53.80
AVG	**0.029**	**0.076**	**0.105**	**0.042**	**-64.9**
(St.D)	**(0.048)**	**(0.010)**	**(0.040)**	**(0.023)**	**(12.3)**
CV			**38.1 %**		

A summary of the ratio of rWOB for MCB to MOB (for inspiration, expiration and total breathing cycle) is shown in Table 4.7. The ratios were computed using the average values of rWOB presented in Table 4.6. At ZT, the rWOB of MCB is a factor of 2.6 greater than during MOB. The ratio of the average rWOB (for MCB) to rWOB (for MOB) at NHF20, NHF40 and NHF60 equalled 3.0 , 2.7 and 0.94 respectively. In reality, these ratios may be lower than predicted as MOB will produce a lower fall in MV compared to MCB and therefore the corresponding rWOB may be greater.

Table 4.7 Work of breathing: MCB compared to MOB

Ratio of WOB (MCB) to WOB (MOB)

	Insp.	**Exp.**	**Total**
ZT	2.6	2.8	2.6
NHF20	3.0	2.9	3.0
NHF40	3.1	1.8	2.7
NHF60	-	1.3	0.9

4.3.4 Neonatal work of breathing

Saslow et al. (2006) used planimetric analysis (Fig. 4.1) to study the effect of NHF and CPAP during inspiration. 18 preterm neonates (average weight = 1.1 Kg) were studied. The mean V_t, RR and MV measured by the authors (Saslow et al. (2006)) have been presented in Table 4.8. The V_t has been matched to a 3.6 Kg neonate (weight of the neonate whose upper airway model was investigated in Chapter 3). It is observable that as NHF increases, RR reduces, V_t increases and MV decreases. This is consistent with the observation made by Bräunlich et al. (2013).

By fitting the data in Table 4.8 to a linear equation, Eq. 4.19 (relationship between NHF and RR) and Eq. 4.20 (relationship between NHF and V_t) were obtained.

$$RR = -3.2nhf + 81.167 \tag{4.19}$$

$$V_t = 0.0001nhf + 0.0109 \tag{4.20}$$

Table 4.8 Summary of V_t and RR data for neonates, adapted from Saslow et al. (2006)

NHF (L/min)	**V_t (ml/Kg)**	**V_t for a 3.6 Kg neonate**	**RR (bpm)**
3	3.15 ± 1.36	11.34 ± 4.90	$71.3 \pm 22..2$
4	3.08 ± 1.35	11.09 ± 4.86	68.9 ± 21.9
5	3.21 ± 1.31	11.56 ± 4.72	64.9 ± 23.4

These two equations were used in Model 3 (Effect of ZPIF included, I:E ratio = 0.64, MV varies with NHF) to predict the effect of MV changes on rWOB. Miedema et al. (2013) found the I:E ratio of 22 infants (gestational age =30 days, weight = 1.3Kg) to be 0.64. Model 4 was not used because information on the effect of NHF on I:E ratio is scarce for neonates. A sensitivity study was however performed using Model 4 in which I:E ratio was increased and decreased by 10 %. This changed rWOB by 6 %. Fig. 4.14 shows the rWOB due to the application of NHF3, NHF6 and NHF9 via the OPT314 and OPT316 cannula. The error bars represent the uncertainty propagation error in rWOB due to uncertainty in resistance coefficient estimates.

The overlap of error bars at NHF3 (Fig. 4.14) is an indication that cannula size does not make a significant difference. Cannula size has a statistically significantly effect on rWOB at NHF6 and NHF9 with OPT316 producing a lower rWOB.

The percentage changes in rWOB due to NHF3, NHF6 and NHF9 are shown in Fig. 4.15 and Table 4.9. In Chapter 3, it was found that OPT316 engendered a lower airway resistance. The lower resistance posed by the OPT316 and the NHF-induced fall in MV coupled with the ZPIF effect explains why the rWOB is lower with therapy than without (i.e. zero therapy, ZT) during NHF6 and NHF9. For OPT314, the rWOB is less with therapy than without (ZT) only at NHF9.

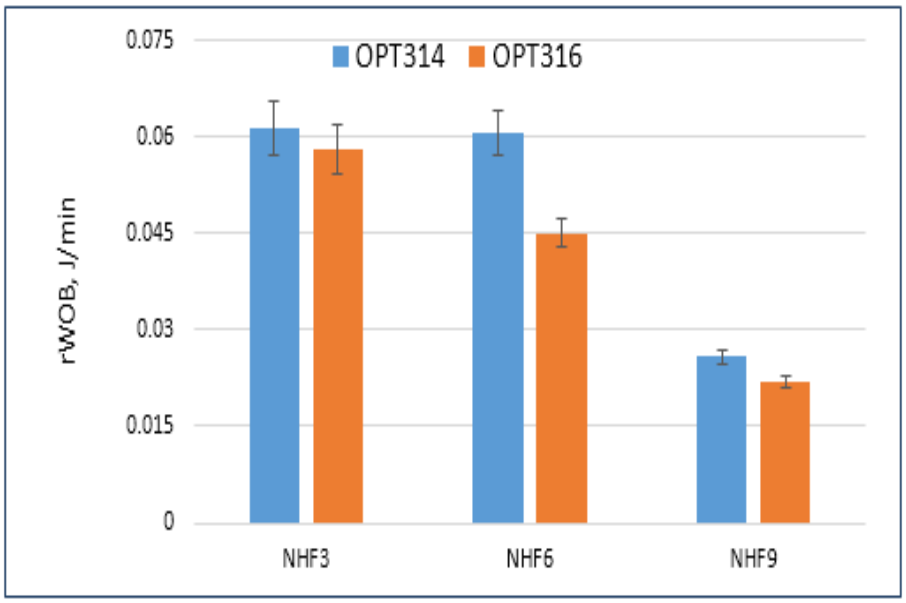

Fig. 4.14 Plot showing the effect of cannula size on neonatal rWOB

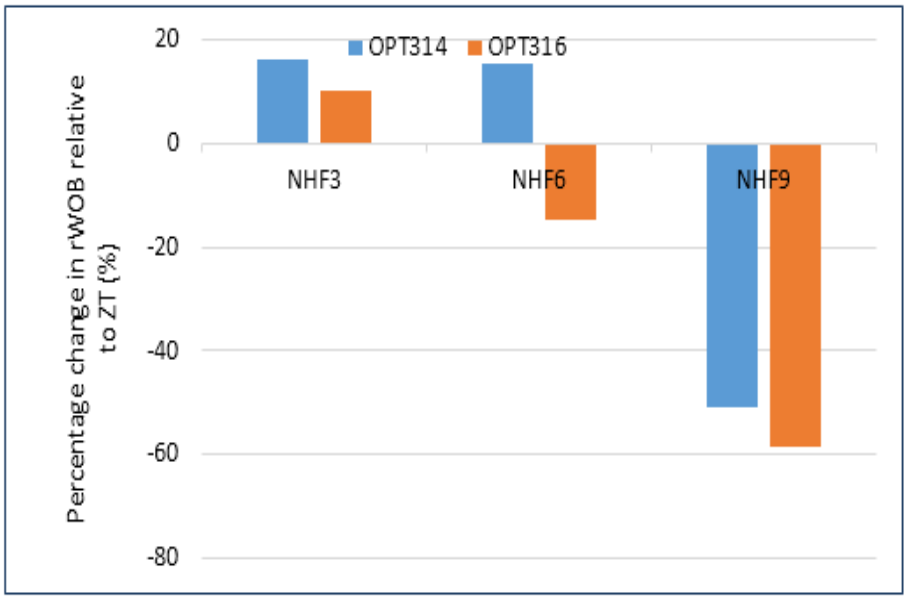

Fig. 4.15 Plot showing the percentage fall in rWOB due to NHF

Table 4.9 Summary of rWOB - neonate model

rWOB @ ZT	**0.053**		
NHF (L/min)	**NHF3**	**NHF6**	**NHF9**
OPT314			
rWOB	0.0613	0.061	0.026
$\delta ZT(\%)$	16.24	-15.28	-50.84
Error	0.0042	0.0035	0.0011
OPT316			
rWOB	0.0581	0.045	0.02
$\delta ZT(\%)$	10.23	-14.49	-58.42
Error	0.0028	0.0022	0.0009

4.4 Discussion

4.4.1 How NHF reduces work of breathing

Dysart et al. (2009) postulated that matching NHF with inspiratory flow demand may attenuate nasopharyngeal resistance and lead to a reduction of work of breathing. The nasal cannula is designed to reach past the nasal valve (which has significant resistance) leading to a reduction of inspiratory work of breathing. Information on expiratory effort against cannula jet is scarce in the literature (Dysart et al. (2009)). In the words of Lee et al. (2013a) "whether NHF reduces work of breathing by stenting the airway or by providing gas flows that matches or exceeds the patient's peak inspiratory flow as proposed by Dysart et al. (2009) remains to be determined".

Findings from the present study indicate that the fall in inspiratory work of breathing due to NHF can be explained in terms of the NHF-induced rise of the ZPIF (see Fig. 4.3), below which inspiration requires no respiratory effort. Since a greater ZPIF is related to NHF, the present finding lends credence to the theory that reduced work of breathing may be due to the matching of PIF and NHF. The expiratory flow must negate the cannula jet momentum, leading to a rise in static pressure towards stagnation pressure. It follows that the greater the NHF, the greater the jet stagnation pressure and the effort that will be required to overcome and reverse the jet flow. If NHF raises the total volume of air to be expelled, a rise in flow rate through the leak area and a consequent rise in expiratory pressure is expected.

If RR and V_t do not change, the overall work of breathing can be reduced only if the reduction in inspiratory work of breathing outweighs the NHF-induced rise in expiratory resistance. When RR and V_t remain unchanged, an increase in overall work of breathing is observed due to the increased expiratory resistance. However, the fall in RR and consequently MV (at a constant I:E ratio) produced a reduction in overall work of breathing in an NHF dependent manner in the adult model (Table 4.4). In the neonate model, the fall in rWOB occurred at NHF9 (Fig. 4.15). For both adults and neonates, the fall in work of breathing

was partly due to the rise in ZPIF with NHF. With variable I:E ratio, work of breathing will further reduce if the ZPIF remains above the peak inspiratory flow after a fall in I:E ratio. From Fig. 4.11, it seen that this may occur at 60 % of the I:E ratio prior to NHF.

It has been reported that chronic obstructive pulmonary disease (COPD) and airway restrictive diseases are characterised by a rise in RR (Loveridge (1984); Tobin et al. (1983)). Since COPD augments expiratory resistance, which in turn demands a greater breathing effort, the fall in RR (Bräunlich et al. (2013); Diab et al. (2015); Lara et al. (2016)) coupled with the possible decrease in work of breathing upon the application of NHF may provide a significant relief to the respiratory musculature of COPD patients.

4.4.2 Mouth open versus mouth closed breathing

The work of Groves and Tobin (2007) and Ritchie et al. (2011) remain the only published works where a comparison is made of airway pressure under mouth close breathing (MCB) and mouth open breathing (MOB) in the adult population. In both studies, mouth closed pharyngeal pressures were greater. Since the ZPIF rises with NHF-induced rise in pharyngeal pressure, the saved energy due to ZPIF is less during MOB. Note that MOB in itself requires relatively less effort compared to MCB because tracheal flow is supplied by the oral and nasal pathways in parallel, their effective resistance being less than either one. The contribution of cannula size to rWOB generally rises with NHF for MCB and MOB.

Particle imaging velocimetry experiments conducted by Spence (2011) show that all the expired volume exits via the oral passage during MOB when NHF of 30 L/min was administered to an adult upper airway model at a peak lung flow of 26 L/min. The nasal passage bore only the inward-directed therapy flow. When therapy was supplied and equal fall in MV was assumed for MCB and MOB, the average rWOB in the MCB state was found to be a approximately a factor of 3 greater compared to MOB state at NHF20 and NHF40 but almost unity at NHF60. This ratio can be less than 3 (at NHF20 and NHF40) as it is likely for the rWOB in MOB to be greater than predicted.

4.4.3 Adult versus neonate work of breathing

Cabello and Mancebo (2006) found the average (and range) work of breathing (resistive plus elastic, for entire airway) of 7 healthy adults (mean age = 29 years) to be 2.4 (1.7 - 3.1) J/min. Otis et al. (1950) concluded that the resistive component of work of breathing is about 30 % . In a study of 9 males (age = 38.3 years) by Ferris et al. (1960) the upper airway resistance was found to be about two-thirds of the total airway resistance during nose breathing. In regards to the findings of Cabello and Mancebo (2006), the rWOB will be two-thirds of 30 % of 2.4 (1.7 -3.1) J/min which equals 0.48 (0.34 - 0.61) J/min. This is lower than the rWOB (0.86 J/min) estimated in the present study for the adult upper airway model (mouth closed breathing state) at ZT. The difference could be attributed to variability in airway compliance and resistance.

Compared to the neonatal work of breathing at ZT (0.053 J/min) - estimated from the mean V_t (11 ml) and RR (81 bpm) for a 3.6 Kg neonate using the data of Saslow et al. (2006), the adult rWOB (0.86 J/min) is greater than the neonate by a factor of 16. The ratio of the work of breathing of an adult (70 Kg) to that of a neonate (3 Kg) as estimated from the report of Cook et al. (1957) is 11. Note that the corresponding body weight ratio (70 Kg /3 Kg) is 23.3.

The breathing parameters of neonates, even of the same weight and age vary significantly (Cook et al. (1957)). In the data reported by Cook et al. (1957) one of the neonates (age 22 hours, weight not indicated) had a RR of 136 bpm and V_t of 10 ml. In the same data, another neonate (weight = 3.6 Kg) had a V_t of 20 ml and RR of 28 bpm. If the same resistance coefficients determined experimentally are used in conjunction with a V_t of 20 ml and a RR of 81 bpm, the rWOB predicted by Model 3 is 0.285 J/min. This equals an adult to neonate rWOB ratio of 3. rWOB can thus vary significantly. Owing to the limited clinical data, greater variability in V_t and RR, and the use of only one neonate and adult model in the present work, it is unclear from the present work, which anthropometric parameter (e.g. weight, height, age etc.) scales best with rWOB

4.4.4 Limitation

The evaluation of the resistive component of mechanical WOB has been restricted to only the upper airway due to a lack of information on the effect of NHFT on lower airway resistance and lung compliance. For the same reason, the extra viscous component of mechanical WOB involved in deforming surrounding tissues during pulmonary excursions (estimated to be 12 % (Otis et al. (1950)) during ZT) has not been included here. The effect of NHF on lower airway needs further study.

4.5 Conclusion

Wakefulness and disease state complicate the influence of NHF on V_t and MV in adults. The rWOB at NHF20, NHF40 and NHF60 is 10 %, 25 % and 88 % less than the rWOB without NHF (ZT) during mouth closed breathing. At ZT, NHF20 and NHF40, the rWOB for MCB was found to be a factor of about 3 greater than that of MOB but close to unity at NHF60. This result assumes equal fall in MV for both states (MCB and MOB). The reduction in rWOB is due to the ZPIF rising with NHF coupled with a fall in MV. For MCB, the influence of NHF on I:E ratio may reduce rWOB if the new I:E ratio is greater than 60 % of the I:E ratio prior to NHF.

Generally, in the adult model, the large cannula produced the greatest rWOB and the small cannula produced the least. Variability in rWOB due to cannula size was found to be NHF-dependent with coefficient of variability (standard deviation/ average rWOB) rising up to 21.1% at NHF60 for MCB. In the MOB state, the coefficient of variability was up to 50 % at NHF40. In the neonate model, the larger cannula (OPT316) caused a greater fall rWOB relative to rWOB at ZT than did smaller cannula (OPT314). The ratio of the rWOB of adults to rWOB of neonates varies significantly due to variations in RR and V_t.

Because of the convincing body of evidence supporting a fall in RR, a rise in MV due to NHF will suggest a pronounced rise in V_t traceable to an increase in inspiratory flow.

Under such circumstances work of breathing may be higher with NHF than without. The interpretation of the therapeutic benefit of NHF to a patient must be comprehensive and not restricted to work of breathing alone as other parameters such as dyspnoea, mouth dryness, (Roca et al. (2010)) functional residual capacity (Corley et al. (2011); Diab et al. (2015)), end-tidal and blood arterial CO_2 concentration (Frizzola et al. (2011)) also indicate the wellbeing of patients in response to NHF.

Chapter 5

An Experimental and Numerical Investigation of CO_2 Distribution in the Upper Airways During Nasal High Flow Therapy

The material covered in Chapter 5 has previously been published in S.C Van Hove et al. (2016). Annals of Biomedical Engineering

This chapter was motivated by the desire to understand the effect of nasal high flow (NHF) on airway CO_2 concentration to scrutinize the postulate that NHF improves oxygenation by flushing nasopharyngeal dead space. In pursuing this goal, the present author used a bench-top experimental approach and Van Hove used a computational fluid dynamics approach. Van Hove used a segmented computed tomography images of the upper airway of a 44 year old man as a model for this study. A physical model of the same upper airway geometry was built using 3D-printing technology (printed in ABS plastic) for the experimental work. In this work, my contribution has been the measurement, interpretation and documentation of pressure and CO_2 experiments to validate the results of Van Hove's numerical models.

5.1 Introduction

Computational fluid dynamics (CFD) has been used to model airflow, temperature and particle deposition within the human nasal cavity. The majority of these simulations model unassisted breathing. Simplifications commonly made in such studies include the use of a single nasal passage (Keyhani et al. (1995); Martonen et al. (2002)), the use of a geometric re-construction instead of an anatomically accurate model (Elad et al. (1993)) and simulating steady inspiratory or expiratory flows (Weinhold and Mlynski (2004); Wen et al. (2008); Zubair et al. (2010)) instead of resolving the full time-dependent breathing pattern. Flow within the models is generally defined by specifying the velocity normal to the nostril opening (Keyhani et al. (1995); Wen et al. (2008)), or by specifying a pressure difference between the atmosphere and the nasopharynx/trachea end of the model (Ozlugedik et al. (2008)). The latter "pulls" air through the model in a similar way to natural breathing so is considered more physiologically accurate (Wen et al. (2008)).

NHF produces positive airway pressure which has been shown to improve oxygenation, ventilation-perfusion matching and respiratory rates (Groves and Tobin (2007); Parke et al. (2011)). Also findings by Dewan and Bell (1994); Frizzola et al. (2011); Tiep and Barnett (2002) and Spence (2011) support the proposition by Dysart et al. (2009) that NHF reduces the anatomical dead space and improves alveolar ventilation by making it a greater portion of the patient's minute ventilation (Dysart et al. (2009)).

CFD simulations with applied NHF have been performed by Kumar et al. (2015) who simulated steady inspiratory and expiratory flow with applied therapy between 20 and 60 L min^{-1} (Kumar et al. (2015); Spence (2011)). The pharyngeal pressure depended on airway geometry and increased nonlinearly with increasing therapy flow rate. Simulations of the CO_2 concentration in respiratory therapies have been performed inside infant face masks and oxygen hoods (Meyer (1989); Mundt et al. (2012)) but not for NHF and not within the nasal cavity. To better understand the dead space washout provided by NHF, it is necessary to understand the flow dependent nature of CO_2 distribution in upper airways. The present

Chapter describes an experimentally validated numerical study of the CO_2 distribution in the upper airway, with and without assisted ventilation, using experimentally measured breathing waveforms and tracheal CO_2 concentrations. How airway pressure varies with NHF is also investigated.

5.2 Materials and Methods

5.2.1 Model geometry

In precursor studies a medical computed tomography (CT) scan of a 44 year old male with mouth closed was used to create the upper airway model (Spence et al. (2011)). The model, which included both sides of the nasal cavity and extended to the beginning of the trachea, had no apparent airway abnormalities. The CT data was segmented and imported into ANSYS ICEM to create a computational mesh for the numerical simulations. An extended rectangular domain was placed around the nose of the CFD model thereby allowing air to enter the nares at a wide range of angles to accurately model the in vivo scenario.

The nasal cannula of the NHF device investigated in this study, (OptiflowTM Fisher & Paykel Healthcare Limited (F&PH), Auckland, New Zealand), consists of two prongs of elliptical cross-section and a manifold that rests on the upper lip. Stereolithographic (STL) files of the cannula geometry were inserted into the computational airway model. The cannula positioning was chosen to reflect the normal clinical use of NHF. The two cannula prongs in the CFD model were partially inserted into the nostril to approximately 74 % of their total length. The angle of the prongs opening surface was approximately 33° from the vertical and the cannula rested within 2 mm of the upper lip and the nostril junction. These measurements were unavailable for the experimental model.

It was assumed the airway was rigid and the mucosal layers effects could be ignored. The shape of the external nose was included as it is known to influence inspiration flow patterns (Doorly et al. (2008)).

5.2.2 CFD simulation

Meshes of the airway geometry were generated using an octree volume filling algorithm to create the tetrahedral volume mesh while a patch-independent method was used to produce a triangular surface mesh at the domain boundaries. A smaller element size was specified within the nasal cavity, in particular around the cannula prongs and within the nasal valve, to increase the accuracy of the computed solution in this area of rapid flow. Five inflation layers of prism elements, with a growth ratio of 1.1, were added to accurately capture the high velocity gradients occurring at the no-slip boundaries of the airway and cannula. The element quality of the surface and volume meshes were improved before and after the generation of the inflation layer.

ANSYS CFX 16.0 was used as the CFD solver. The total flow through the model consisted of two components, humidified air and CO_2, homogenously mixed with a reference pressure of zero atmospheres and a diffusivity of 1.41 x 10^{-5} m^2 s^{-1}. Humidified air was modelled as an ideal gas with a dynamic viscosity of 1.88 x 10^{-5} kg m^{-1} s^{-1} and density of 1.068 kg m^{-3}, while CO_2 was modelled with a dynamic viscosity of 1.45 x 10^{-5} kg m^{-1} s^{-1} and density of 1.977 kg m^{-3}. The model was solved isothermally with a total flow temperature of 37 °C as it was assumed the thermal effects on the flow were negligible (Hahn et al. (1993); Keyhani et al. (1995)). NHF was humidified to 99 % relative humidity and no supplementary oxygen was added. Unassisted breathing was simulated at the nasopharynx opening using a five term Fourier series (displayed in Fig. 5.1) which represented an experimentally measured in vivo breathing waveform.

An atmospheric boundary condition of 0.04 % CO_2 was applied to the exterior domain surrounding the nose. The airway domain was initialised with a relative pressure of zero atmospheres, zero velocity and the concentrations of humidified air and CO_2 set to 99.96 and 0.04 % respectively. All solid boundaries on the airway surfaces were specified as rigid, no-slip walls, and the k–ω Shear Stress Transport (SST) turbulence model (Menter (1994)) was applied to the domain with a turbulence intensity of 5% specified for all flow boundaries

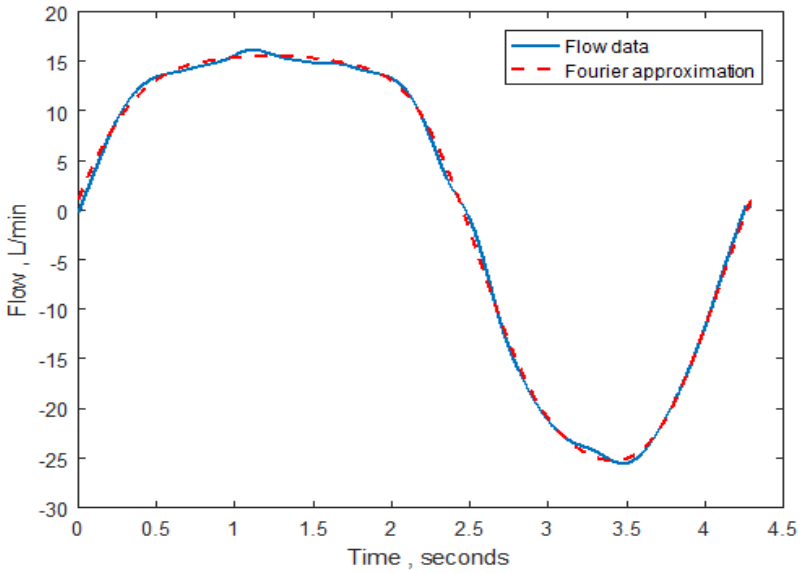

Fig. 5.1 : Breathing waveform (solid line) and Fourier approximation of the breathing waveform (dashed line) used to drive the stepper motor and used to specify the flowrate at the nasopharynx in the CFD simulations. Positive flows indicate expiration while negative flows indicate inspiration

and for initialisation. This turbulence model has previously been used in respiratory flow simulations (Elcner et al. (2016); Zubair et al. (2010)). Five spatially uniform flow rates between 10 and 60 L min^{-1} were specified normal to the cannula openings to simulate assisted breathing. Simulations over multiple breaths did not significantly alter the CO_2 volume fraction profiles, hence data for only the first breath are presented.

Three significantly different meshes (with 1.6 x 10^6, 4.2 x 10^6 and 10.6 x 10^6 nodes) were generated by reducing the global mesh density scale factor while maintaining the same meshing parameters. Steady state expiration (uniform tracheal inlet velocity of 2.5 ms^{-1}) during NHF therapy of 40 L min^{-1} was simulated to assess the convergence of the results with mesh size. The integrated force over the airway surface was used as an indicator of mesh quality. A Richardson extrapolation was used to obtain an estimate of the exact value of integrated force over the airway surface as the number of nodes in the mesh tends to infinity. This gave an approximate relative error of 1.1 % for the finest mesh which was used in all subsequent simulations.

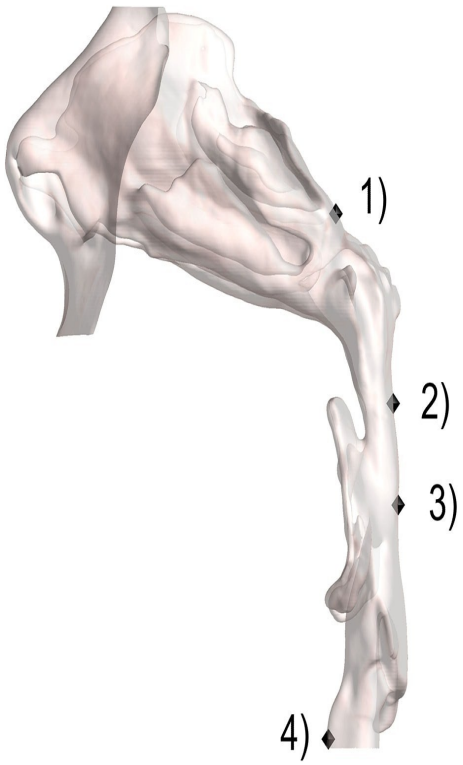

Fig. 5.2 Location of the four taps used to validate the numerical pressure and CO_2 results on the airway model of a 44 year old adult male

Transient simulations of the expiratory phase, with NHF therapy applied at 40 L min^{-1}, were initially performed using a range of time-steps (0.001, 0.002 and 0.004 s) to test numerical stability. For each point specified in Fig. 5.2, the CO_2 volume fraction at mid expiration did not differ significantly, however the Courant–Friedrichs–Lewy (CFL) number for the simulations increased with increasing time-step. The time-step used for all following simulations was 0.002 s and had a CFL number of approximately 30. The solution was considered to be converged once the RMS residuals for mass and momentum reached a value below 10^{-4} or a maximum of 20 coefficient loops were achieved for each time-step.

5.2.3 Experimental procedure

Experiments were conducted for validation of the CFD process as well as to provide tracheal boundary values for flow and CO_2 concentration. A life sized airway model was 3D-printed

in ABS plastic. The full experimental setup is outlined in Fig. 5.3. The breathing cycle used (Fig. 5.1) is based on an adult human breathing at rest. It was measured in vivo on a healthy 24 year old male and scaled to have tidal volume 450 ml, respiratory rate 14 breaths per minute, representative of an average adult (Tobin et al. (1983)). The breath waveform was reconstructed using the five term Fourier series shown in Fig. 5.1 and was physically replicated using a computer controlled piston pump. The physical model had a functional residual capacity (FRC) of 2400 ml created by the piston and piston barrel, and a dead space of 150 ml (typical of the human adult (Ritchie et al. (2011)) which comprised of the airway model (53 ml) and connecting tubing.

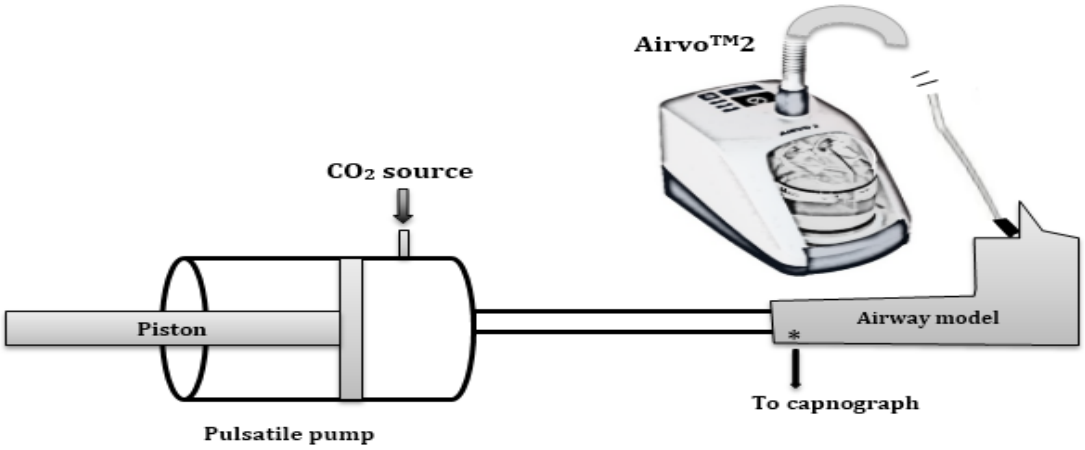

Fig. 5.3 A schematic of experimental apparatus used for CO_2 and pressure measurements. It comprises of a piston pump, CO_2 bleed system, capnograph and F&P Healthcare NHF nasal cannula

The capnograph, Oridion MiniMediCO2 Microstream (OEM CO_2 Module) was used to measure airway CO_2 concentration. Airway pressure was measured using the AMS 5915 pressure transducers (manufactured by Analog Microelectronics GmbH, Germany). The physical airway model had numerous 1 mm diameter tap holes (some shown in Fig. 5.2) where pressure and CO_2 concentration could be measured. For each therapy flow rate, the CO_2 concentration was measured at tap location 4 and a Gaussian distribution was fitted to the data. These functions were used to specify a time varying CO_2 volume fraction condition at the nasopharynx opening in the CFD simulations. The experimental measurement technique did not allow for spatial recording of the CO_2 concentration hence the spatially uniform

boundary condition used for nasopharyngeal CO_2 is a limitation of the study. CO_2 was bled from a compressed CO_2 tank into a pump cylinder via a pressure regulator and rotameter. A bleed rate of 98 scc min^{-1} with a 20 kPa back pressure was used to simulate a peak CO_2 partial pressure of about 40 mmHg (Hess (2011)) which corresponds to the end-tidal CO_2 of a healthy adult (Ritchie et al. (2011)).

The miniMediCO2 capnograph constantly samples CO_2 over a 400 mm conduit and therefore requires correction for transit time delays and signal dispersion. The reduction of signal intensities (dispersion) of sampled CO_2 may be attributable to diffusion and turbulent mixing as the gas travels along the conduit (Reischl and Beaucage (1986)). The datasheet of the MiniMediCO2 capnograph indicate a transit delay time and rise time of 2.7 s and 190 ms respectively. The measured signal can be thought of as a convolution of the original undispersed signal and a dispersion function. Extraction of the undispersed data requires a deconvolution process. The deconvolution algorithm implemented in Python 3.5 is shown in Appendix B.

5.3 Results

5.3.1 Pressure validation

Numerical simulations were performed using air at 20 °C to compare the static pressure at the locations specified in Fig. 5.2. The pressure time-series for a single breath are displayed in Fig. 5.4 for both unassisted breathing and for assisted breathing where the NHF rate was 40 L min^{-1}. The numerical results have been time-averaged to give the same sampling frequency as the experimental results. The experimental results are displayed with the standard deviation from the mean breath as error bars. The first 2.3 s represent the expiratory phase followed by 2 s of inspiration.

During unassisted inspiration the static pressure within the airway becomes sub-atmospheric with the points closest to the lungs reaching the most negative static pressure values. Ap-

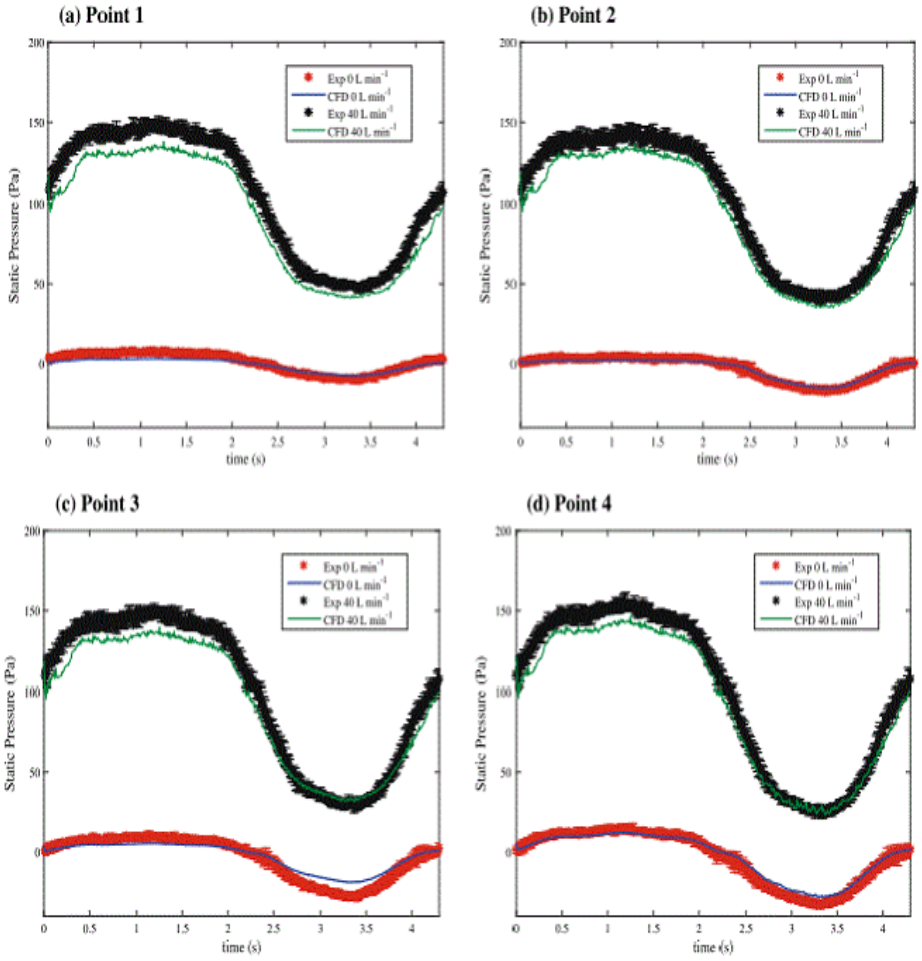

Fig. 5.4 Time-series of the static pressure at the four comparison points for unassisted breathing (red & blue) and for assisted breathing with applied NHF rate of 40 L min^{-1} (black & green)

plying NHF therapy raises the mean static pressure within the airway as shown in Fig. 5.4. For unassisted breathing the magnitude of the experimental results are consistently greater than the numerically obtained values suggesting that the experimental resistance to flow is greater than that simulated numerically. This could be due to pressure losses associated with the surface roughness of the printed model as well as a difference in airway resistance due to uncertainty in the placement of the nasal cannula in the experimental setups. A zero drift error of $\pm$ 5 Pa also affects the experimental results due to the sensor calibration. The results

broadly confirm that the numerical solution is a reasonable approximation of the flow in the airway model.

5.3.2 CO_2 validation

Fig. 5.5 compares the experimental and numerical time-series for the CO_2 volume fraction at each of the points displayed in Fig. 5.2, for unassisted breathing (blue) and for a NHF rate of 60 L min^{-1} (red). The experimental data was obtained by averaging several breaths over a 5 min period and the standard deviation is shown by the error bars. No synchronisation signal between the experimentally measured flow and CO_2 was recorded, thus the temporal initialisation of the experimental data is unknown. In order to compare the results a temporal shift was applied to the experimental data to maximise the correlation between the data sets.

Increasing the NHF rate diminishes the peak CO_2 volume fraction at each location because the larger flow rates input a larger amount of gas with a low CO_2 concentration into the nasal cavity. The expired gas within the airway is diluted by the NHF therapy and hence the therapy reduces the maximum CO_2 volume fraction level at the pharynx. The CO_2 concentration during NHF assisted breathing begins to decrease earlier than during unassisted breathing. This occurs because prior to flow reversal the air speed coming from the trachea slows sufficiently that NHF therapy causes a net flow of low CO_2 gas into the cavity before inspiration which does not occur during unassisted breathing. The numerical CO_2 concentration time series are consistently wider than the experimental profiles. This is due to the capnograph sensor rise time, (Langer et al. (1985)) which could not be corrected and which is greater than that recommended for clinical use (Rimensberger (2015)). Experimental errors could also have been introduced by CO_2 losses encountered in the experimental set-up, such as in the piston and connections, as well as temperature differences between the numerical and experimental model. The numerical simulations were performed isothermally at 37 °C whereas the air introduced at the trachea in the physical experiments was not maintained at this temperature.

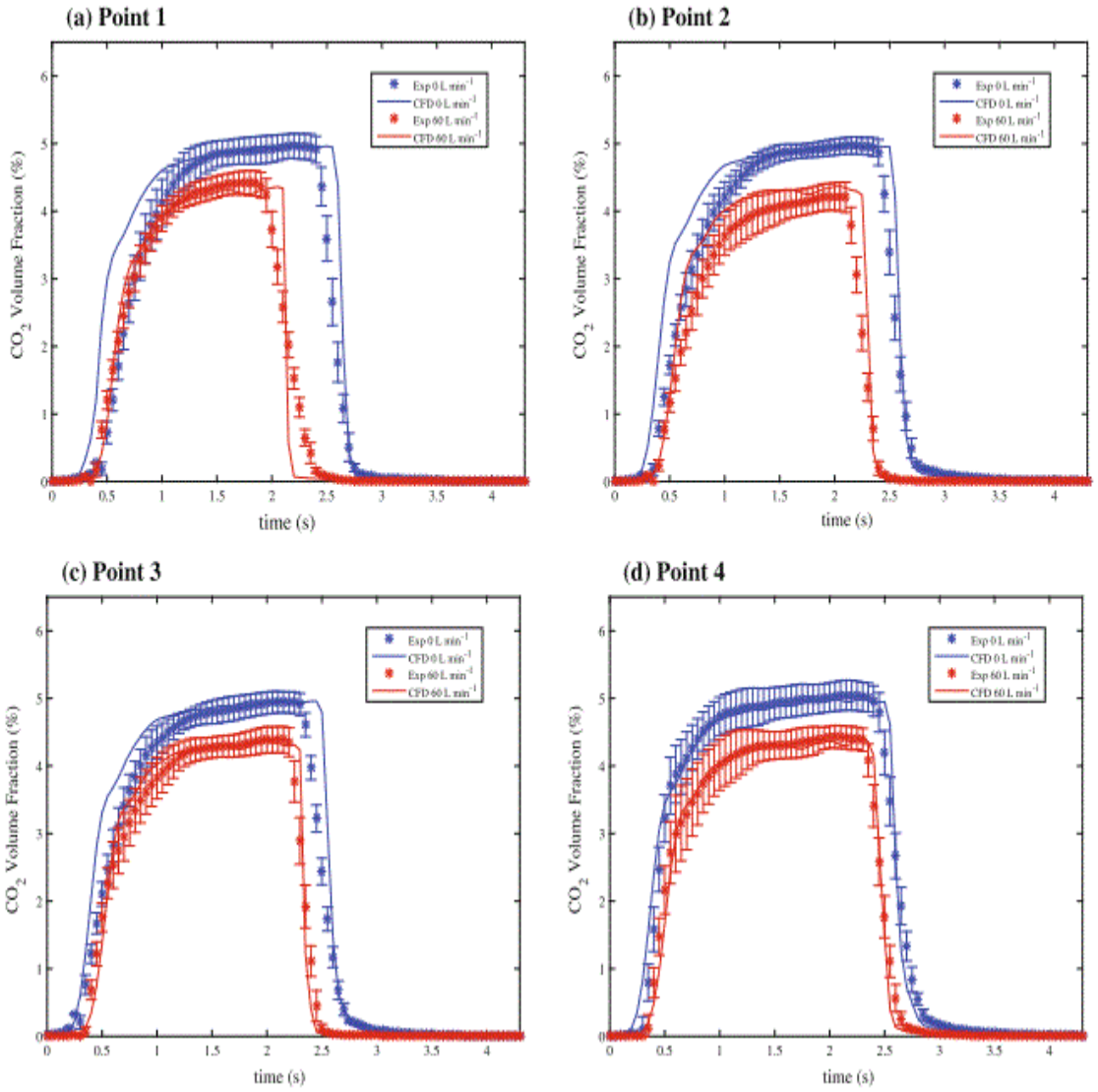

Fig. 5.5 Time-series of the CO_2 volume fraction at the four comparison points for unassisted breathing (blue) and assisted breathing with NHF flow rate of 60 L min-1 (red).

The numerical results are most similar to the experimental results at the inferior locations (such as point 4) as these locations are closest to the trachea where the CO_2 boundary conditions are specified. The agreement is satisfactory implying that the CO_2 distribution calculated numerically is a reasonable estimate to that present in the airway model.

5.4 Discussion

The numerical results for pressure and CO_2 in the upper airway are similar to the experimental validation data and are consistent with published in vivo measurements. Parke et al. (2009) reported the mean expiratory pharyngeal pressure of post-cardiac surgery patients on NHF rates of 35 L min^{-1} to be 2.7 $\pm$ 1.0 cmH_2O (264.8 $\pm$ 98.1 Pa) while Groves and Tobin (2007) measured a range of 5.5 – 8.8 cmH_2O (539.4 – 863.0 Pa) in healthy volunteer subjects to NHF rates of 60 L min^{-1}. The inspiratory and expiratory pharyngeal pressures during unassisted breathing simulated by Kumar et al. (2015) were - 30.9 and 7.1 Pa respectively. With NHF rate of 40 L min^{-1} the inspiratory and expiration pharyngeal pressures rose to 38.3 and 184.4 Pa respectively which is similar to the pressures at point 4 in the present simulations.

The current study shows that increasing NHF rate augments the mean nasopharyngeal pressure which is consistent with clinical studies that show that NHF therapy delivers small but significant positive airway pressure (Parke et al. (2009)). This positive airway pressure is believed to lower total pulmonary resistance and improve gas exchange by keeping alveoli open throughout ventilation (Dysart et al. (2009)). In the study by Kumar et al. (2015) reversal of flow direction and recirculation in the nasal valve region during NHF therapy are attributed to an adverse pressure gradient caused by negative pressures around the floor of the nasal valve. Spence et al. (2012) reported two recirculating features within the anterior portion of the nasal cavity during expiration. Such flow recirculation may cause the flushing of nasopharyngeal dead space.

The present study has demonstrated that NHF therapy produces a nasopharyngeal washout effect by simulating the concentration of CO_2 in the upper airway during natural and assisted breathing. Applying NHF provides the anterior of the nares with a source of air containing a lower CO_2 concentration than the expired air that would be found in the nasal cavity at the end of expiration during unassisted breathing. During expiration, the jet of low CO_2 air causes circulation of the expired air in the anterior nasal cavity hence some of the higher

CO_2 concentration air leaves the nasal cavity via the nostrils and the anatomical dead space is reduced. Frizzola et al. (2011) observed a flow dependent decrease in blood CO_2 partial pressure and increase in blood O_2 partial pressure in neonatal piglets on NHF therapy, suggesting that NHF therapy washes out the nasal cavity in a similar manner to tracheal gas insufflation (Frizzola et al. (2011)). The flushing action causes the following inspiration to have a greater proportion of air with a low CO_2 concentration. This in turn improves respiratory efficiency as the alveolar gas fractions are modified such that the CO_2 fraction is lower and the oxygen concentration is greater than during unassisted breathing (Frizzola et al. (2011)). However, Chatila et al. (2004) did not find that high flow oxygen therapy altered the arterial CO_2 partial pressure compared to low flow oxygen therapy (Chatila et al. (2004)). It is unknown whether nasopharyngeal washout translates into a decrease in alveolar CO_2 partial pressure significant enough to alter blood arterial CO_2 partial pressure.

The present model could be extended to incorporate the lower airways and gas transport between blood and alveoli in order to determine whether the decrease in inspired CO_2 observed is adequate to modify alveolar and blood gas compositions. In the present study, discrepancies exist between the numerical and experimental results for both pressure and CO_2. Experimental errors that may explain these discrepancies include the absence of synchronised experimental flow and CO_2 measurements. The lack of synchronisation between the experimental breathing flow and CO_2 measurements was a significant limitation.

The use of a rigid, mucous free and cilia free model are limitations to the correct modelling of the respiratory physiology. Both numerical and experimental models assumed a rigid airway however physiologically the soft palate, epiglottis and tongue are compliant structures compared to the remainder of the nasal cavity. At very high flow rates, such as during vigorous sniffing, the nasal valve is capable of collapsing but this is unlikely to occur during restful breathing hence a rigid wall assumption is appropriate for simulations of breathing at rest (Bailie et al. (2006); Keyhani et al. (1995)). The application of NHF is somewhat similar to sniffing in that a much higher flow rate passes through the nasal valve region. In the

present study, the Reynolds number (Re) at the cannula prong opening during NHF therapy of 40 L min-1 is approximately 4600 and the Re for sniffing is approximately 3050 (Keyhani et al. (1995)). Hence, the use of a rigid model may be a limitation of the present study. The models presented ignore the effects of the nasal mucous layer and assume a no-slip condition on the nasal cavity wall. This assumption is commonly applied in computational models of airflow in the upper airway because both the thickness of the mucus layer and the velocity of the mucociliary escalator are sufficiently small in comparison to the flow structures in the upper airway (Keyhani et al. (1995)). Finally, this study has only considered a single subject which may not represent the features of an entire population. The model was chosen because experiments have been published using the same nasal geometry (Spence et al. (2012)) hence comparison of flow fields was possible.

5.5 Conclusion

Numerical simulations of the flow and CO_2 concentration within the upper airway of a subject undergoing nasal high flow therapy have been performed. The numerical simulations were validated using an experimental model and the results are consistent with previously reported airway measurements. A nasopharyngeal washout phenomenon was observed and the amount of CO_2 cleared from the nasal cavity was found to increase in a flow dependent manner over the range of flows simulated.

Chapter 6

In-vitro Modelling of the Effect of Nasal High Flow Therapy on Tracheal CO_2 Tension During Episodes of Apnea

6.1 Introduction

There are three types of apnea namely obstructive sleep apnea, central sleep apnea and a complex sleep apnea (combination of CSA and OSA). CSA is a sleep disorder marked by intermittent cessation of breathing which lasts for 10 or more seconds at frequencies of 5 or more episodes per hour (Javaheri (2010, 1999)). CSA episodes can occur at up to 35 per hour (Javaheri (1999)).

CSA ensues when the pontomedulary pacemaker (breathing rhythm generator) is temporarily unable to send breathing rhythms to drive respiratory muscles (Javaheri (2010)). This instability in breathing may be accompanied by an increased sensitivity to CO_2 (Javaheri (1999)). The decrease in alveolar ventilation during sleep raises alveolar CO_2 tension which initiates hyperventilation and drives arterial CO_2 below the breath-stimulation threshold

(apnoeic threshold) hence cessation of breathing. After a finite time, CO_2 rises above the breath-stimulation threshold and breathing commences (Dempsey (2005); Javaheri (2010)).

CSA has been reported to occur in 30 - 40 % of patients recovering from heart failure (Cao et al. (2013); Javaheri et al. (2009); White (2005)). A retrospective study conducted by Javaheri et al. (2009) amongst 1286 patients receiving obstructive sleep apnea (OSA) treatment by continuous positive airway pressure (CPAP) titration indicated that the incidence of CSA ranged from 3 - 10 % monthly. CSA is reported to occur more frequently at high altitudes and in individuals on high doses of opioid drugs (White (2005))

The presence of adequate respiratory effort and reduced upper airway patency distinguishes obstructive sleep apnea (OSA) from CSA (Costanzo et al. (2015)). The reduced airway patency in OSA is thought to be caused by the ineffectiveness of the phayrngeal dilator muscles or a more negative pharyngeal pressure induced by an intense diaphragmatic contraction (White (2005)). CPAP is widely reported as the standard treatment modality for OSA patients (Aurora et al. (2012); Bradley and Floras (2003); Issa and Sullivan (1986)). Nasal high flow (NHF) therapy involves the administration of warmed (37 ^{o}C), humidified (100 % R.H) and oxygen-titrated air (>21 % O_2) at flow rates up to 8 L/min in neonates (Manley et al. (2013); Motojima et al. (2016); Ojha et al. (2013)) and 60 L/min in adults (Ward (2013)). Clinical studies indicate that NHF is effective in treating OSA (McGinley et al. (2009)). This work was motivated by the postulation that NHF flushes nasopharyngeal CO_2 (Dysart et al. (2009); Möller et al. (2015); Schneider et al. (2013)). These observations led to the hypothesis that NHF may attenuate the $EtCO_2$ during and after CSA. In the present work, tracheal $EtCO_2$ is measured in a physical model before, during and after CSA (without NHF) and compared to a situation where NHF is applied.

6.2 Methodology

6.2.1 Experimental setup

The adult upper airway model (UAM) used in Chapter 3 was used in the present work. See Fig. 6.1a. The UAM was connected to the programmable piston pump (PP) as shown in Fig. 6.1b. The apparatus setup (Fig. 6.1b) is same as used in Chapter 5. Tests conducted by placing a wire-gauze (to enhance mixing) at the entrance of the PP yielded no significant difference in end-tidal CO_2 concentration ($EtCO_2$) ($< \pm 3$ %) showing that CO_2 is adequately mixed in the chamber. NHF was administered using AIRVO™2 device and OPT844 medium cannula (Fisher & Paykel Healthcare Ltd, Auckland).

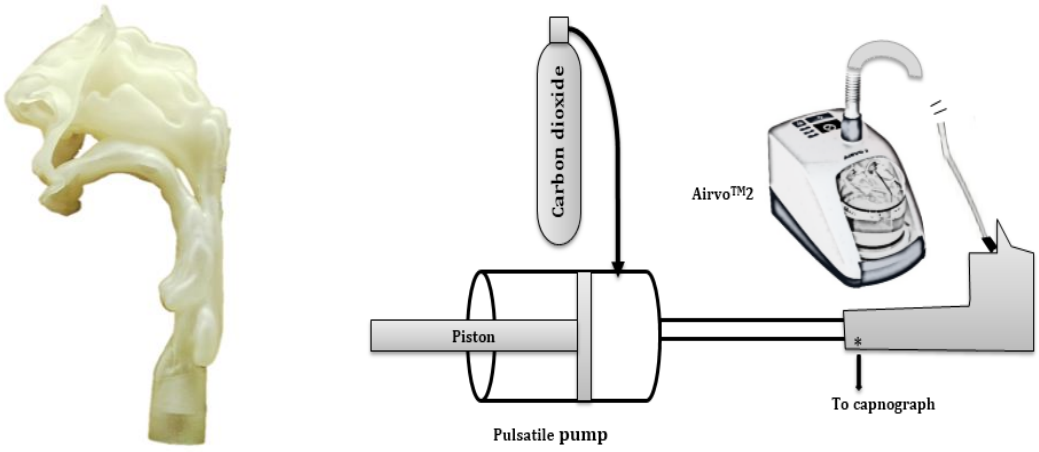

(a) Airway model (b) setup

Fig. 6.1 (a) Upper airway model (b) UAM is connected to the PP and AIRVO™2 device. CO_2 source is connected to PP for simulation of metabolic CO_2 production. CO_2 is sampled at the trachea during experiment

6.2.2 Experimental procedure

The PP was programmed to reproduce the breathing flow pattern of a 24 year old healthy male adult with a respiratory rate of 14 breaths per minute and I:E ratio of 0.72 (Fig. 6.2). Simultaneously, CO_2 was bled into the piston cylinder of the PP at a flow rate of 98 scc/min

(with CO_2 source pressure maintained at 20 KPa). At this bleed rate, the capnograph reported a capnogram that had an end-tidal CO_2 tension ($EtCO_2$) of 5.2 ± 0.3 (v/v) % (which represents the $EtCO_2$ of a spontaneously breathing healthy adult). Logging of the CO_2 data was commenced. Without NHF, central sleep apnea (CSA) lasting for 10 seconds (CSA-10) was simulated by stopping the PP for 10 seconds.

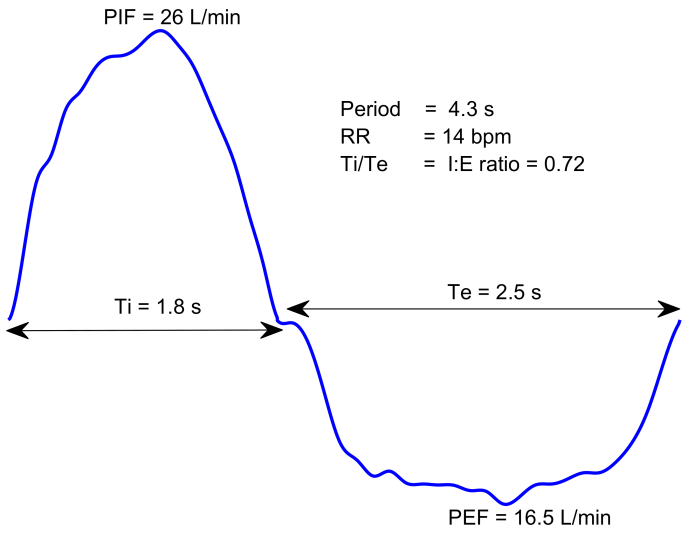

Fig. 6.2 The breathing flow pattern of a healthy 24 year male adult. Characteristics: inspiratory time (Ti) = 1.8 s, expiratory time (Te) = 2.5, I:E ratio (Ti/Te) = 0.72, peak inspiratory flow (PIF) = 26 L/min, peak expiratory flow (PEF) = 16.5 L/min, respiratory rate (RR) = 14 breaths per minute (bpm)

NHF of 10 L/min was then administered prior to the simulation of CSA-10 and a record was made of the capnogram. This was repeated for NHF up to 60 L/min in steps of 10 L/min. These two tests (with and without NHF) were repeated for CSA lasting up to 40 seconds in steps of 10 seconds.

6.3 Results

The capnograms for a 30 second CSA (CSA-30) with NHF ranging from 10 L/min to 60 L/min are presented in Fig. 6.3. With the PP operating ($0 <$ time < 50 s), a repeatable cycle

of CO_2 with a peak of 4 - 5 % ($[EtCO_2]_{steady}$) at the end of each expiration is seen. There are some variations in $[EtCO_2]_{steady}$ due to mixing from cycle to cycle. During apnea (50 $<$ time $<$ 80 s) CO_2 at the trachea may drop due to diffusion but generally rises by 0.1 %. When PP motion (breathing) resumes, the elevated level of CO_2 built up in the piston is forced out and registers in the trachea leading to the maximum $EtCO_2$ ($[EtCO_2]_{max}$) on the second breathing cycle. After this time, $[EtCO_2]_{max}$ decays to the original steady breathing value of 4 - 5 % ($[EtCO_2]_{steady}$) in a manner described by Eq. 1.

$$EtCO_2(t) = [EtCO_2]_{steady} + ([EtCO_2]_{max} - [EtCO_2]_{steady})exp^{(-\lambda t)} \tag{6.1}$$

The decay time constant (λ) estimated with 95 % confidence interval is 0.016 (0.0105 - 0.021 s^{-1}). A prediction of the decay of $[EtCO_2]_{max}$ using Eq. 6.1 is presented in Fig. 6.3a (see solid curve). It is observable that the $EtCO_2$ prior to CSA-30 falls with NHF up to NHF 40 L/min and then remains almost unchanged with NHF. The $[EtCO_2]_{max}$ after CSA-30 follows the same trend. The same trend was observed for all other CSA times.

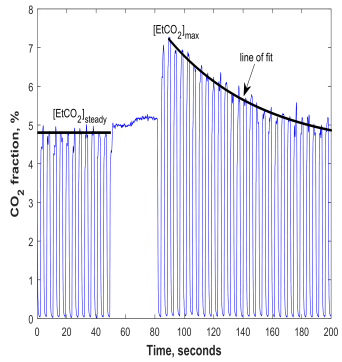

(a) NHF10

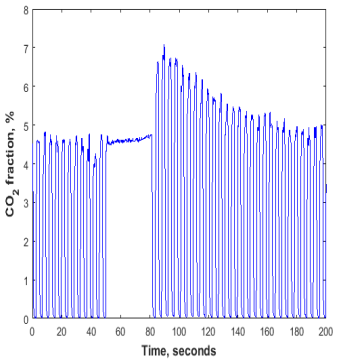

(b) NHF20

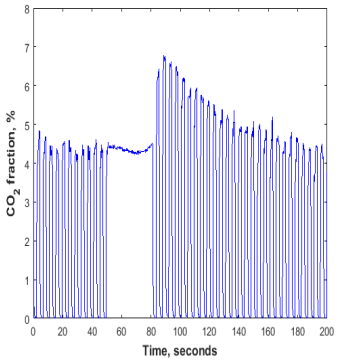

(c) NHF30

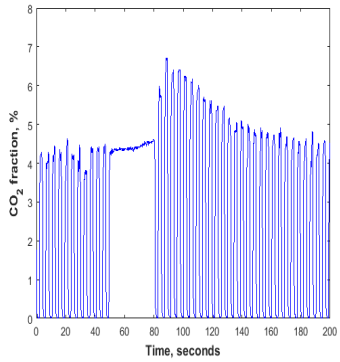

(d) NHF40

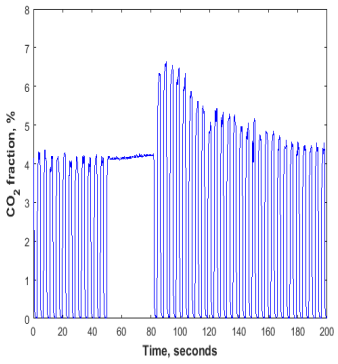

(e) NHF50

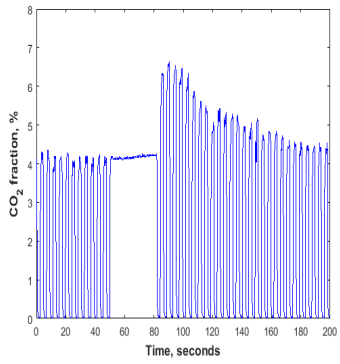

(f) NHF60

Fig. 6.3 Effect of NHF ranging from 10 L/min to 60 L/min on $EtCO_2$ after apnea

The $[EtCO_2]_{max}$ at all NHF (10 - 60 L/min), immediately after CSA, for all CSA duration times (10 - 40 seconds) have been plotted in Fig. 6.4. Data for spontaneous breathing (SB) - no CSA - is also presented in Fig. 6.4. The error bars represent 2 standard deviations in $EtCO_2$ measured over 5 separate experiments. At all NHF, $[EtCO_2]_{max}$ increases with CSA duration. The $[EtCO_2]_{max}$ at zero-therapy (ZT) (NHF = 0), NHF of 40 L/min and NHF of 60 L/min (NHF60) during CSA-10 are 6.18 %, 5.04 % and 4.94 % respectively. The $[EtCO_2]_{max}$ at ZT, NHF of 40 L/min and NHF60 during CSA of 40 seconds (CSA-40) are 8.25 %, 7.07 % and 7.00 % respectively. The $[EtCO_2]_{max}$ at NHF of 40 L/min and NHF of 60 L/min are close, indicating a plateau of $[EtCO_2]_{max}$ after NHF of 40 L/min (Fig. 6.4). In considering the CSA-10 plot for instance, the fall in $[EtCO_2]_{max}$ at ZT to the $[EtCO_2]_{max}$ at NHF of 60 L/min is about 18 %. The fall is the same for CSA-20, CSA-30 and CSA-40.

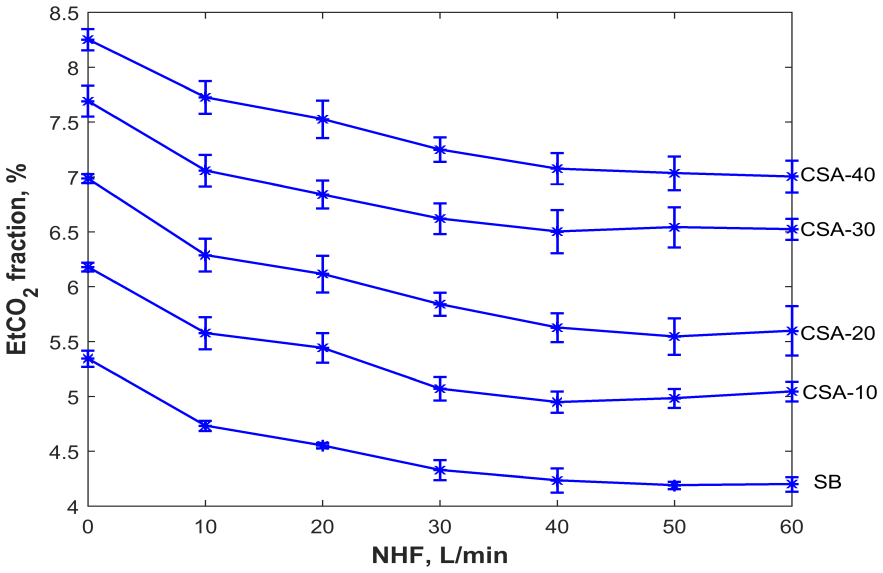

Fig. 6.4 Plot of $EtCO_2$ against NHF for CSA ranging from 10 to 40 seconds. The error bars represent two standard deviations in $EtCO_2$ measurement over 5 repetitions

Since the $EtCO_2$ of the tracheal sample approximates the average alveolar CO_2 tension (Levine et al. (1997)), it is concluded that NHF of 60 L/min may reduce alveolar CO_2 tension by 18 %. During spontaneous breathing (no CSA), $EtCO_2$ rises from 5.2 % (v/v) (39.2 mmHg) at NHF = 0 to 8.2 % (v/v) i.e. 62.3 mmHg at CSA of 40 seconds. This represents

a rise rate of 0.6 mmHg/second. In the physiological system, the flux of CO_2 into the alveolar space from the pulmonary capillaries is driven by diffusion gradients which means the amount of flux decreases as the alveolar CO_2 rises. As a limitation of the experimental setup, CO_2 was bled into the piston pump at a constant rate, which is not physiological.

6.4 Discussion

CSA occurs frequently in obstructive sleep apnea patients Javaheri et al. (2009)Cao et al. (2013) and can occur in healthy individuals Badr (2005). NHF has been reported to treat OSA but there is scarce information on how it could be beneficial to CSA patients (McGinley et al. (2009)). Findings from the present study indicate a rise in $EtCO_2$ from 5.2 % (v/v) (39.2 mmHg) up to 8.2 % (v/v) (62.3 mmHg) over an apnea time of 40 seconds. This equals a CO_2 concentration rise rate of 0.6 mmHg/second. In a group of 14 healthy adults (mean age = 36 years), anesthetized to simulate apnea, Stock et al. (1989) found a 0.2 mmHg/second rise in arterial CO_2 tension ($PaCO_2$) in the first minute and 0.06 mmHg/second thereafter. This is similar to the rate found in the current work, for the same duration (less than one minute). Stock et al. (1989) notes that the rise in $PaCO_2$ during apnea follows a logarithmic trend with the fastest rate of rise occurring in the first minute followed by a gradual asymptotic ascent towards a saturation point. In the work of Patel et al. (2011), the rise in $EtCO_2$ concentration, post apnea, from 5 % (v/v) (38 mmHg) to 8 % (v/v) (60.8 mmHg) occurred over an apnea time of 20 minutes (equivalent to an average rise rate of 0.03 mmHg/second), which is of the same order as found by Stock et al. (1989) after the first minute.

NHF of 60 L/min, which is tolerated well by patients (Ward (2013)) can reduce $EtCO_2$ and consequently alveolar CO_2 tension (P_ACO_2) by 18 %. This results supports the reported nasopharyngeal washout effect in which NHF reduces dead space and improves alveolar oxygen fraction (Dysart et al. (2009); Möller et al. (2015)).

In patients for whom apnea is triggered by hypercapnia, there is a narrow difference between the apnoeic threshold (P_ACO_2 below which apnea occurs) and the P_ACO_2 associated with spontaneous breathing (baseline-P_ACO_2). A broader difference produces greater breath-control stability and a reduced number of episodes per hour (Dempsey (2005)). Figure 4 shows that $EtCO_2$ during spontaneous breathing, $[EtCO_2]_{steady}$, (baseline-$EtCO_2$) reduces with NHF. The characteristics of the breath control system (central nervous system) may explain how the reduction in baseline-$EtCO_2$ influences susceptibility to apnea. Dempsey

(2005) used the breath control characteristics proposed by Cherniack and Longobardo (1974) and Khoo et al. (1982) to explain CSA occurrence. Figure 5 (adapted from Dempsey (2005)) illustrates how alveolar ventilation control may be influenced by NHF. The horizontal axis represents P_ACO_2 (in mmHg) and the vertical axis denotes alveolar ventilation (in L/min). The points x, y, and z are representative of different baseline-P_ACO_2 levels and the arrow

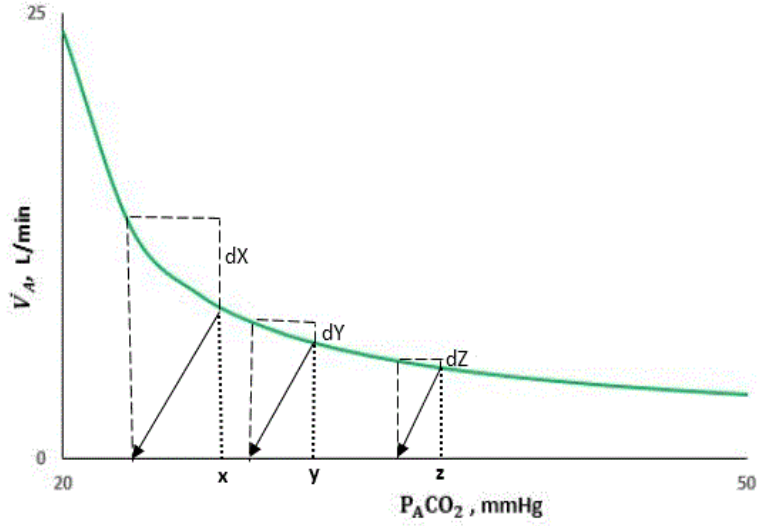

Fig. 6.5 Plant loop gain concept. The tips of the arrows represent apnoeic threshold and x, y, and z denote different baseline-P_ACO_2

heads point to their corresponding apnoeic thresholds. All arrows have the same slope to indicate a constant sensitivity of the breath control system to CO_2. dX, dY and dZ are the changes in alveolar ventilation required for x, y, and z to drop to their corresponding apnoeic threshold (tip of the arrow head). Note that apnea occurs when baseline-P_ACO_2 goes below the apnoeic threshold (Dempsey (2005); Javaheri (2010)). It is observable that as baseline-P_ACO_2 rises ($z > x$), the alveolar ventilation change required to cause apnea becomes smaller ($dZ < dX$) and the more likely it is for apnea to occur. This is known as the plant loop gain concept (Dempsey (2005)). This implies that a hypercapnic patient (higher baseline-P_ACO_2) will be more susceptible to apnea because small fluctuations in alveolar ventilation will cause their P_ACO_2 to fall below the apnoeic threshold (Hernandez and Patil (2016)).

Arguing from the plant loop gain concept, it may be inferred that a reduction in the baseline-P_ACO_2 and maximum $EtCO_2$ (immediately after apnea) - which can be up to 18 % at NHF of 60 L/min, may improve the stability of the breathing control system by widening the gap between the apnoeic threshold and baseline-P_ACO_2. Consequently, we speculate that NHF may be capable of reducing the number of apnea episodes per hour.

6.4.1 Limitations of this work

The experimental setup differs from the physiological system in terms of the rigidity of the piston cylinder (lung compliance is $\approx$ 200 mL/cmH_2O for healthy young adults (Galetke et al. (2007))), absence of gas diffusion across walls of the pump, lack of a bronchial tree and presence of a point CO_2 source. The constant release rate differs from the physiologically realistic system. In a human experiencing apnea, the rate of CO_2 diffusion from the blood to alveoli will reduce as CO_2 builds up in the lungs. The oscillatory air motion in the airway due to the heart motion moving the lung lobes (cardiogenic oscillations) have been observed to influence CO_2 mixing and clearance (Collier et al. (2015)). These were not included in the experimental setup.

6.5 Conclusions

In conclusion, the $EtCO_2$ before and after apnea reduces in an NHF dependent manner (0.15 mmHg/L/min) until NHF of 40 L/min where it reaches a plateau. The true plateau value may be lower if cardiogenic oscialltions in the air flow are present. The maximum $EtCO_2$ (immediately after apnea of 40 seconds) at zero therapy, can fall by 18 % with the application of 60 L/min of NHF. Following the plant loop gain model we speculate that the frequency of apnea per hour may be reduced by NHF.

Chapter 7

The Effect of Variation in the Breathing Flow Pattern in COPD Patients on End-tidal CO_2 Tension ($EtCO_2$)

7.1 Introduction

Previous studies have explored how CO_2 tension modulates ventilation via a feedback mechanism. It is reasonable to hypothesise that each breathing pattern (though influenced by disease state) is optimized in terms of shape, magnitude and frequency to effect a specific change in CO_2 tension. How tidal volume, dead space volume, respiratory frequency and metabolic CO_2 rate influence end-tidal CO_2 ($EtCO_2$) has been studied. In a study by Parot et al. (1980) the respiratory frequency and metabolic CO_2 production in hypercapnic and non-hypercapnic COPD patients were found to be similar however the hypercapnic group showed a lower tidal volume. In hypercapnic individuals, the $EtCO_2$ correlates well with the ratio of dead space volume to tidal volume (Blanch et al. (2006); Calverley (2003)). Clinical studies on how breathing flow pattern alone changes $EtCO_2$ are scarce due to the difficulty in

simultaneously maintaining the same tidal volume, peak airflow and I:E ratio over several breaths.

$EtCO_2$ has been reported to correlate well with arterial CO_2 tension (Nagler and Krauss (2009)) which can indicate hypercapnia. The capnogram of COPD patients is modulated by the degree of obstruction of the airways (Gluncic et al. (2015); Krauss and Hess (2007); You et al. (1994)) which causes the expiratory gas flow to be staggered and makes the capnogram 'shark finned' in shape (Mieloszyk et al. (2014)). Depending on the degree of obstruction, the COPD capnogram can be unique compared to those of healthy individuals (Jaffe (2006)). Nasal high flow is administered to COPD patients to improve ventilation (Bräunlich et al. (2013)) and prevent obstructive sleep apnea. An in-vitro study of the effect of breathing flow pattern, with and without NHF on $EtCO_2$ is explored to find if pattern of the waveform alone makes sufficient difference to $EtCO_2$ to affect the health of a patient. Also the influence of I:E ratio variation on $EtCO_2$ is explored.

7.2 Methodology

7.2.1 Waveform collection

Four breathing flow patterns obtained from COPD patients (age range = 19 - 77 years, FEV_1 % predicted range = 36 to 63 %) were collected from the literature. In three of these flow patterns (Colasanti et al. (2004); Dellaca et al. (2004); Williams et al. (2013)), flow was plotted against time. In the remainder (Dellacà et al. (2009)), the flow pattern was presented as a plot of tidal volume versus time which was numerically integrated (into flow vs. time plot) after acquisition. Together with a healthy adult breathing flow waveform, which was previously used by Van Hove et al. (2016) five waveforms were used in all.

A plot of all the collected flow waveforms is shown in Fig. 7.1 (a). Note that positive flow represents inspiration and negative flow, expiration. The COPD flow waveforms have a sharp concavity in the expiratory phase. The four COPD waveforms are designated as WF1, WF2,

WF3 and WF4 with the healthy waveform labelled as WF5 (dotted plot). It is noticeable that they vary in frequency and amplitude.

7.2.2 Normalization of waveforms

All the waveforms were normalized to the same tidal volume and respiratory rate via a linear rescaling of time axis followed by a linear rescaling of the flow rate axis using different scaling factors for inspiratory and expiratory phases. Also, the inspired volume was matched to the expired volume. Two groups of breathing flow waveforms were obtained by scaling each breathing flow to two different I:E ratios i.e. 0.67 (IE1-group) and 0.43 (IE2-group), which corresponded to inspiratory time fractions of 40 % and 30 %. The fall in I:E ratio from 0.67 to 0.43 is 35 %. The breathing flow patterns in the IE1-group and IE2-group are respectively shown in Fig. 7.1b and Fig. 7.1c. Two different I:E ratios were needed to investigate the effect of I:E ratio on $EtCO_2$. I:E ratio difference > 30 % was hypothesized to be sufficient to elicit a change in $EtCO_2$. The choice of I:E ratios were not without justification as Tobin et al. (1983) reported an I:E ratio of 0.72 ± 0.031 for healthy adults and 0.53 ± 0.046 for adult COPD patients.

7.2.3 Experimental setup

The experimental set-up is identical to that shown in Fig. 6.1b (Chapter 6). The same adult upper airway model (Fig. 6.1a, Chapter 6) - in closed mouth state - was used. A mixing test was conducted by placing a wire-gauze (to enhance mixing) at the entrance of the PP. This yielded no significant difference in $EtCO_2$ ($< \pm 3$ %). The volume of the piston chamber at the end of expiration (functional residual capacity) was maintained at 2500 ml for all experiments.

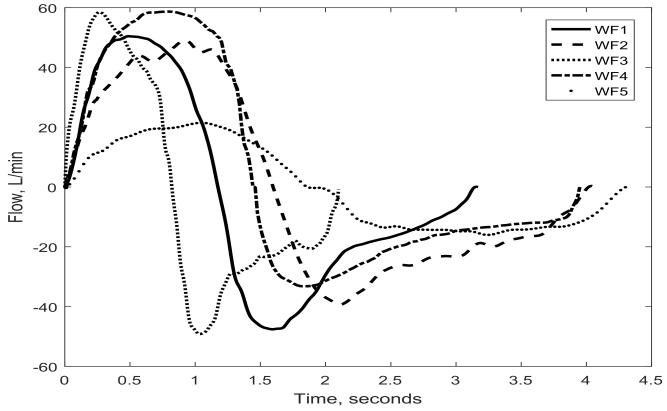

(a) All breathing flow patterns (before scaling)

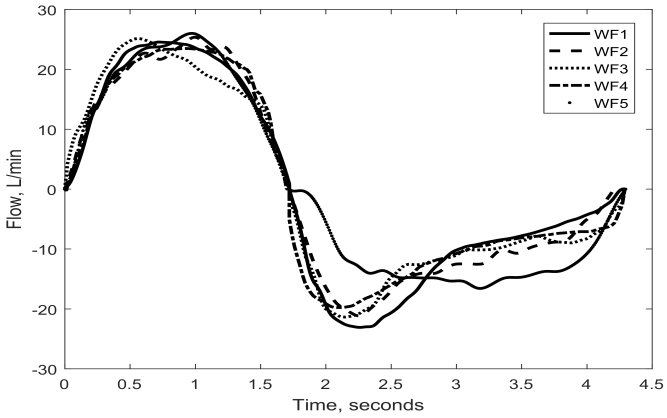

(b) All breathing flow patterns normalized to IE1

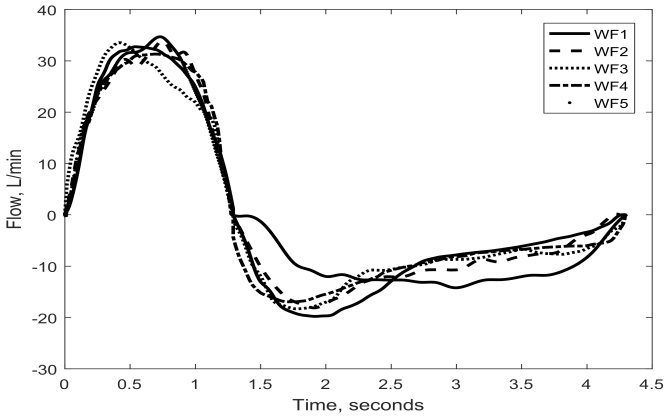

(c) All breathing flow patterns normalized to IE2

Fig. 7.1 (a) All waveforms before scaling (b) IE1-group of flow waveforms (c) IE2-group of flow waveforms

7.2.4 Experimental procedure

The healthy adult breathing flow (in IE1-group) was reproduced in the UAM. Metabolic CO_2 production was simulated by bleeding CO_2 at a flow rate of 98 scc/min (at a 20 KPa CO_2 source pressure) into the piston chamber of the PP. The end-tidal ($EtCO_2$) at this setting was 5.4 % $\pm$ 0.3, which is comparable to the $EtCO_2$ of a resting healthy adult. CO_2 data was recorded before (zero-therapy, ZT) and during the application of 30 L/min of NHF. An identical procedure was performed for all other waveforms with 6 repetitions for each.

7.3 Results

7.3.1 $EtCO_2$ with and without NHF

The capnogram was recorded for 20 consecutive breathing cycles for each experimental repeat. The 20 cycles of capnogram in repeat one (for healthy waveform (WF5) in IE1-group) have been superimposed and cascaded with those of the other repetitions as shown in Fig. 7.2a. The variations in $EtCO_2$ from cycle to cycle is due to mixing. Fig.7.2b shows the average of all 120 capnograms (20 cycles in each of the 6 repeats) for the WF5 (in IE1-group) with and without NHF. An identical plot is shown in Fig. 7.2c for the WF4 waveform (COPD waveform). Note the characteristic 'shark fin' shape of the COPD waveform (which is due to airway obstruction (Mieloszyk et al. (2014))). The spontaneous breathing plots for a no NHF condition in Fig. 7.2b and Fig. 7.2c show a minimum CO_2 concentration of about 0.2 % which is due to rebreathing of dead space CO_2 during inspiration. Note how this falls to 0.04 % (atmospheric CO_2 concentration) when NHF of 30 L/min is applied. This indicates a reduction in re-inspired dead space CO_2 by NHF, which is in line with findings in Chapters 5 and 6, and together support the washout mechanism of NHF proposed by Dysart et al. (2009). In Fig.7.2b and Fig. 7.2c the $EtCO_2$ falls by approximately 20 % when NHF of 30 L/min is applied.

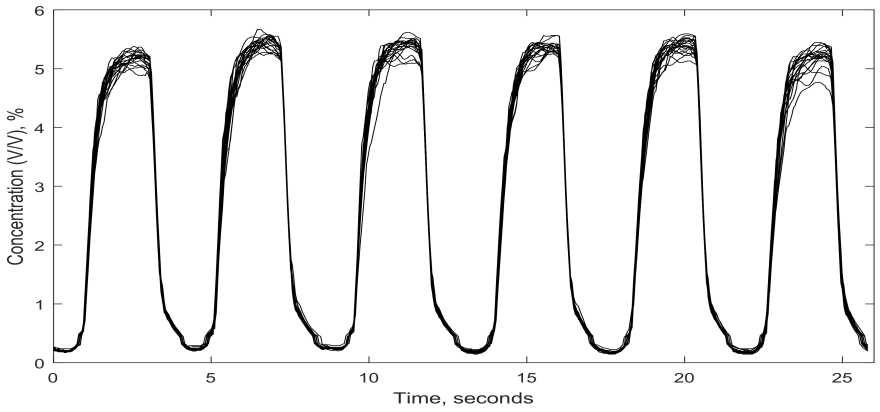

(a) A train of 6 capnograms for WF5, 20 cycles in each

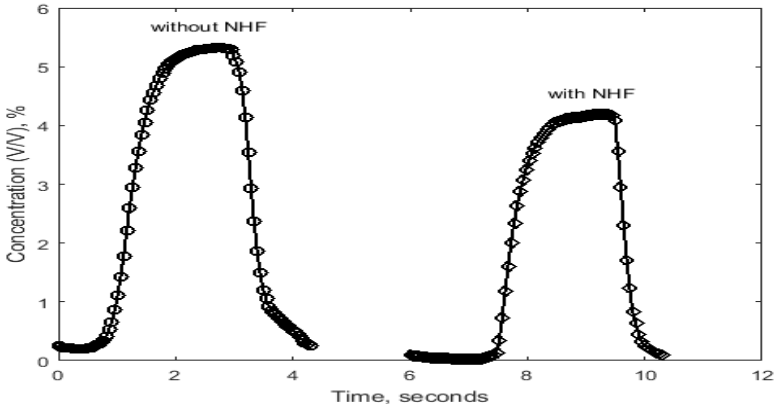

(b) Average of 120 capnograms with and without 30 L/min of NHF for WF5

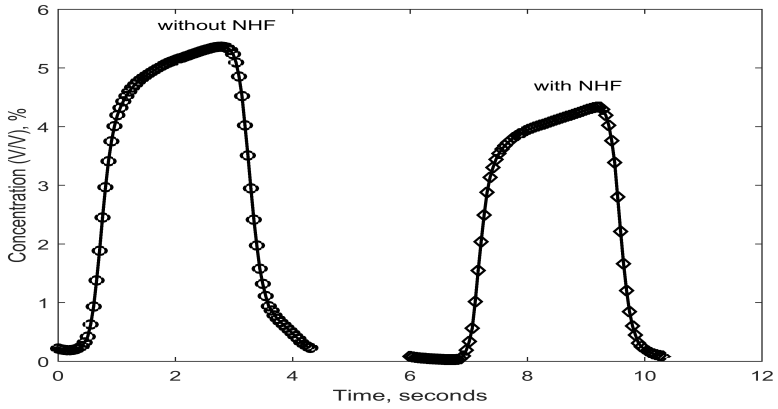

(c) Average of 120 capnograms with and without 30 L/min of NHF for WF4

Fig. 7.2 (a) A train of 6 capnograms for the healthy waveform (WF5) (b) Average of 120 capnograms for WF5 (c) Average of 120 capnograms for WF4

The average $EtCO_2$ (of 120 capnograms) for each waveform (in both IE1-group and IE2-group) have been presented in Fig. 7.3. The error bars represent two standard deviations in $EtCO_2$. In Fig. 7.3, the $EtCO_2$ vary slightly between waveforms (e.g. see IE1-group waveforms) however the error bars overlap. Also, a difference in $EtCO_2$ and error bar overlap is seen in the pairs of plots belonging to the same waveform (e.g. see label WF4 - IE1-group and IE2-group pair).

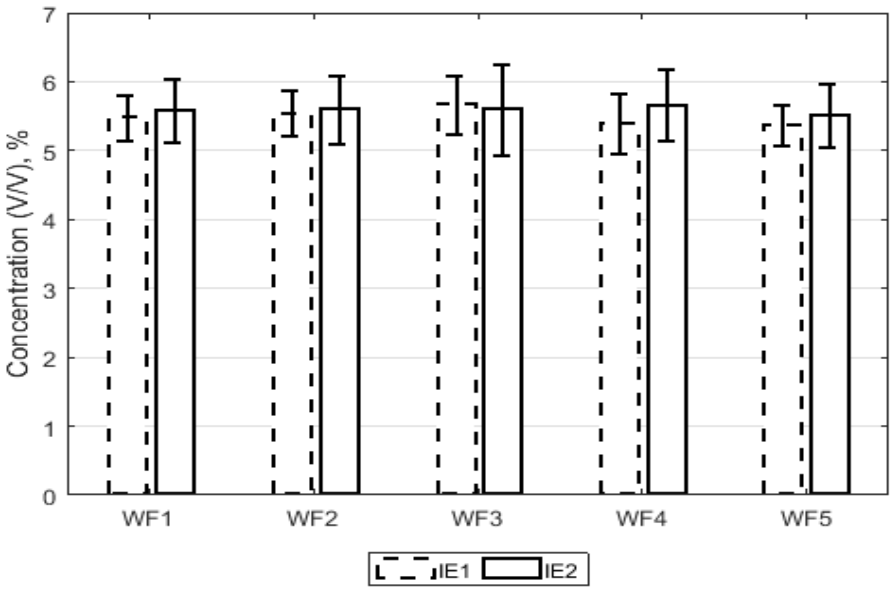

Fig. 7.3 A plot of the average $EtCO_2$ of 120 capnograms associated with flow waveforms in both groups (IE1-group and IE2-group). The errorbars represent two standard deviations in $EtCO_2$ over the 120 capnograms

The present finding shows that the characteristic shape of the COPD capnogram ('shark fin') - due to airway obstruction - can be reproduced from the corresponding breathing flow pattern. This supports the clinical reports that the breathing flow pattern is modified by airway obstruction (Williams et al. (2013)) which in turn affects the shape of the capnogram (Mieloszyk et al. (2014)). Though error bar overlap in $EtCO_2$ are observed amongst flow patterns of the same I:E ratio it is not conclusive if this means no statistically significant difference in $EtCO_2$. In what follows a test of statistical difference in $EtCO_2$ is performed.

7.3.2 Test of statistical significance

A single factor Anova test was performed to find if the difference in $EtCO_2$ was statistically significant amongst waveforms of the same I:E ratio. Further, a two-sample t-test (assuming unequal variances) on pairs of $EtCO_2$ belonging to the same waveform but differing in I:E ratio was performed. In both tests, the critical value to confirm the null hypothesis was set to 0.02. The results are presented in Table 7.1, which shows evidence of statistically significant difference in $EtCO_2$ (p-value < 0.02) within the same group of I:E ratio (single factor Anova test, Table 7.1). Except for WF4, I:E ratio made a statistically significant difference in $EtCO_2$ (p-value < 0.02) in pairs belonging to the same I:E ratio (two-sample t-test, Table 7.1). WF4 was not distinct in characteristics from the other waveforms.

Table 7.1 Results of a single factor Anova test and a two-sample t-test

single factor Anova test

Groups (IE1 and IE2)	**Sum of squares**	**df**	**Mean square**	**F**	**P-value**
IE1	259	4	65	20	0.0001
IE2	84	4	21	5	0.0006

two-sample t-test

	WF1	**WF2**	**WF3**	**WF4**	**WF5**
p-value	0.003	0.0001	0.002	0.05	0.002

Another two-sample t-test was performed for each I:E ratio group to find the specific pairings of flow waveforms that showed statistically significant difference in $EtCO_2$. Note that 5 flow waveforms will yield 10 pairs in each I:E ratio group. The results are presented in Table 7.2 in which 7 pairs (70 % of 10 pairs) - in bold ink - show statistically significant difference in $EtCO_2$ (p-value < 0.02) within the IE1-group. Only 4 pairs (40 % of 10 pairs) in the IE2-group have statistically significant differences in $EtCO_2$.

It is concluded that the differences in $EtCO_2$ of waveforms that are similar in all but pattern are statistically significant (p-value < 0.02) (a single factor Anova test, Table 7.1).

Table 7.2 Two-sample t-test to identify specific pairings of flow waveforms that showed statistically significant difference in $EtCO_2$

p-value	**WF1/ WF2**	**WF1/ WF3**	**WF1/ WF4**	**WF1/ WF5**	**WF2/ WF3**
IE1	0.068	**0.000**	0.048	**0.017**	**0.000**
IE2	0.030	0.105	**0.000**	**0.000**	0.32
p-value	**WF2/ WF4**	**WF2/ WF5**	**WF3/ WF4**	**WF3/ WF5**	**WF4/ WF5**
IE1	0.08	**0.000**	**0.000**	**0.000**	**0.000**
IE2	0.036	0.031	**0.015**	**0.013**	0.49

Also, EtCO_2 is sensitive to I:E ratio as 4 out of 5 flow waveforms (WF1, WF2, WF3 and WF5 but not WF4) showed a statistically significant difference in $EtCO_2$ (p-value < 0.02) (two-sample t-test, Table 7.1). Furthermore, it is deduced from Table 7.2 that though statistically significant disparities in EtCO_2 was found in each group (Table 7.1), intragroup differences in EtCO_2 in the higher I:E ratio group (IE1-group, I:E ratio = 0.67) was greater (70 %) than in the lower I:E ratio group (IE2-group, I:E ration = 0.47) - only 40 % of the pairs showed a significant difference in EtCO_2.

7.3.3 Shape parameter and $EtCO_2$

Harmonic distortion (Hd) describes the degree to which a periodic signal deviates from a sinusoid (Frey et al. (2001)). It is mathematically expressed as:

$$Hd = \frac{\sqrt{H_2^2 + H_3^2 + H_4^2 + ...}}{H_1} \tag{7.1}$$

where H_n is the root-mean-square amplitude of the n^{th} harmonic (found using Fourier decomposition) of the waveform. $n = 25$ was used as beyond this, changes in Hd was found to be insignificant. Hd was computed for the entire breathing cycle, for the inspiratory phase and then the expiratory phase. $EtCO_2$ correlated better with a product of the inspiratory

Hd and the peak inspiratory flow. This product is designated as IDf. The $EtCO_2$ and their corresponding IDf are presented in Fig. 7.4. The Spearman's correlation coefficient (ρ) and error (2 standard deviations) in the measurement of $EtCO_2$ are also shown in Fig. 7.4. The coefficient of determination (R^2) (0.75 and 0.88) and ρ (0.9 and 1) indicate a strong correlation between IDf and $EtCO_2$ (see Fig. 7.4). It is not clear what implication this has for breathing.

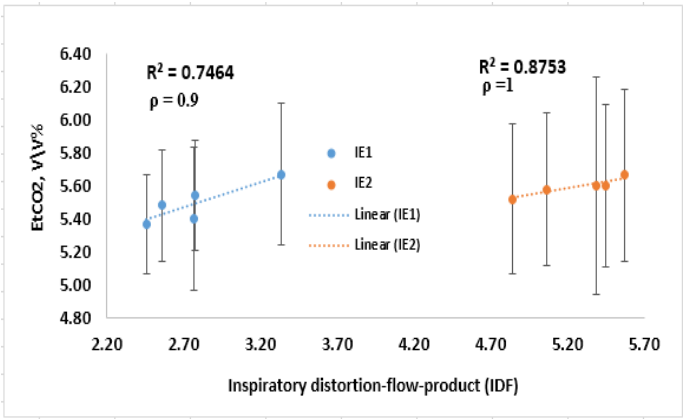

Fig. 7.4 plot of $EtCO_2$ against IDf

In Eq. 7.2, $average[EtCO_2]_{IE2}$ and $average[EtCO_2]_{IE1}$ are respectively, the average $EtCO_2$ in the IE1-group and IE2-group. Using the formula in Eq. 7.2 the average $EtCO_2$ of the IE2-group was found to be 2 % greater than that of the IE1-group. It is concluded that a 35 % fall in I:E ratio (percentage difference between the I:E ratio of 0.67 (IE1-group) and 0.43 (IE2-group)) produces a very little rise in $EtCO_2$.

$$\frac{average[EtCO_2]_{IE2} - average[EtCO_2]_{IE1}}{average[EtCO_2]_{IE1}} \tag{7.2}$$

The coefficient of variability, defined as the ratio of the standard deviation in $EtCO_2$ within the group to the average $EtCO_2$ was found to be 2 % and 1% respectively for the IE1-group and IE2-group.

7.4 Discussion

7.4.1 Effects of waveform shape

NHF reduces physiological dead space and respiratory frequency, and improves gas exchange (Dysart et al. (2009); Mündel et al. (2013); Riera et al. (2013)). The fall in $EtCO_2$ ($\approx$ 20 %) upon the application of 30 L/min of NHF supports the report that NHF improves gaseous exchange by reducing the proportion of CO_2 in re-inspired dead space air (Dysart et al. (2009)). The present data suggests that breathing flow waveforms of different patterns, but similar in tidal volume, period and I:E ratio show statistically significant differences in $EtCO_2$. Further, the results indicate that two breathing waveforms that differ only in I:E ratio can produce different $EtCO_2$. It is more probable (70 %) to find a statistically significant difference in $EtCO_2$ between a group of waveforms (differing only in pattern) which have a greater I:E ratio than those of a lower I:E ratio (40 %).

To preserve tidal volume, a fall in I:E ratio (longer expiration, shorter inspiration) is matched by a rise in peak inspiratory breathing flow and a fall in peak expiratory breathing flow. It is reasonable to expect a higher $EtCO_2$ with a lower I:E ratio as a longer expiratory time suggests more CO_2 retention. In Fig. 7.3, the $EtCO_2$ corresponding to the lower I:E ratio i.e. 0.46 (IE2-group) tended to be greater. Tobin et al. (1983) observed that the inspiratory time (T_i) of 28 COPD subjects (mean age = 67.5 years) was 1 second less than that of healthy adults. Sorli et al. J et al. (1978) concluded that CO_2 retention (marked by higher $EtCO_2$) in COPD patients is due to shallow breathing, which arises from reduced T_i. This is in unison with the observation by Gorini et al. (1996) who found the highest arterial partial pressure of CO_2 amongst COPD patients with the smallest T_i. IE1-group and IE2-group differed in T_i by 0.43 seconds. In the present data, a fall in I:E ratio by 35 % (0.67 to 0.43) corresponded to 2 % rise in $EtCO_2$. Though the present results agrees qualitatively with findings in the literature (Gorini et al. (1996); J et al. (1978); Tobin et al. (1983)) it is concluded that the fall

in $EtCO_2$ due to a fall in I:E ratio by 35 % is small (2 %). The variability in $EtCO_2$ due to flow pattern difference was 1 - 2 %, though statistically significant, it is also small.

The product of inspiratory flow and inspiratory harmonic distortion (IDf) correlate appreciably with $EtCO_2$. The expiratory breathing flow has been reported to be modulated by the inspiratory flow pattern (Frey et al. (2001)) and inspiratory muscle dysfunction has been observed to increase $EtCO_2$. Bégin and Grassino (1991) found that airway resistance correlated well with arterial CO_2 tension (also correlates well with $EtCO_2$). In a study by Loveridge (1984) healthy subjects were observed to show a greater variability in breathing pattern than COPD subjects. Since airway obstruction during COPD influences the flow pattern (by changing its shape and height) and $EtCO_2$, IDf is speculated to be an index related to the ventilatory response to CO_2 tension.

7.4.2 Limitations of this work

The piston chamber is rigid, unlike the physiologic lung which is compliant (lung compliance is $\approx$ 200 mL/cmH_2O for healthy young adults). Note that a constant bleed rate differs from the physiologically realistic system in which CO_2 flow is distributed over time. Also, this work is limited by the number of breathing flow patterns used.

7.5 Conclusion

Breathing patterns similar in tidal volume, respiratory rate, and I:E ratio but differing in shape can produce statistically significant difference in $EtCO_2$ however the variability can be small (1 - 2 %). Further a 35 % fall in I:E ratio of breathing waveform with no change in tidal volume and respiratory rate produce only a 2 % rise in $EtCO_2$. NHF reduces $EtCO_2$ by 20 %.

Chapter 8

Effect of NHF on CO_2: A Mathematical Model

8.1 Introduction

Gray (1951) introduced the multiple factor ventilation control theory in which pulmonary ventilation was independently modulated by O_2, CO_2 and blood pH, unlike earlier models where only one of these was thought to be the primary stimulant of ventilation. Gray's model was limited to steady state ventilation. Grodins et al. (1967), Defares et al. (1960), Milhorn et al. (1965) and other workers extended the work of Gray (1951) by including equations which described "chemical transport, concentration equilibria and blood flow behavior" to predict the dynamic changes in ventilation (Grodins et al. (1967)).

Quite simple models (no respiratory control dynamics, steady state assumed) have also been used to explain respiratory phenomenon. For instance, Chilton and Stacy (1952) used a one compartment (lungs only) model in which the mass balance equations of CO_2 and O_2 in the lung and lumped pulmonary blood capillaries were used to predict alveolar CO_2 tension. Also, Swanson and Sherrill (1983) and Benallal et al. (2002) used a two compartment model (dead space and lung control volumes), assuming a steady CO_2 and O_2 exchange rates, to

predict end-tidal ($EtCO_2$) and arterial CO_2 gradient during rest and exercise. In these models instantaneous mixing of CO_2 with pulmonary air was assumed. Unlike the one compartment model, the two compartment model allows for the prediction of CO_2 tension in the dead space and the examination of how the dead space volume influences both alveolar and dead space CO_2.

To date, the numerical study by Van Hove et al. (2016) (see Chapter 5) and Kumar et al. (2015) represent the only attempts to describe the mechanism of action of NHF using computational fluid dynamics (CFD). Both studies investigated the influence of NHF on airway pressure but Van Hove et al. (2016) further investigated NHF-induced CO_2 flushing from the nasal cavity. These numerical studies were limited to a healthy adults' tracheal flow and did not consider particular disease cases.

The present work was motivated by the desire to predict changes in alveolar and dead space gas fractions when NHF is applied, with a simple model and without computationally expensive iterative calculations. The speed of solution and flexibility of such a model was thought to offer a useful tool for explaining how NHF may be beneficial to central sleep apnea and COPD patients. The results for the dead space CO_2 simulation were then compared to the bench-top experimental results reported in Chapter 6.

8.2 Method

8.2.1 Model setup

A two compartment model identical to that used by Swanson and Sherrill (1983) and Benallal et al. (2002), but refined (addition of NHF and compartmentalized dead space unit) for the present purpose, was used. The model comprises two compartments, a dead space unit and the alveolar unit (Fig. 8.1). The dead space unit represents the volume of all airway regions where gaseous exchange does not occur whilst the alveolar unit represents the combined volume of lung regions that exchange gas with pulmonary capillaries. A major addition to

the present model is the sub-division of the dead space volume into several control volumes (numbering 1, 2, 3 ... N-1, N), forming a one-dimensional mesh (of size N) on which fluxes are calculated using the finite volume approach. Compartmentalization allows for the study of gas concentration in specific areas (e.g. the trachea) and makes the model more physical as it takes a finite time and volume for CO_2 to mix with air. The labels, fd_{CO_2}, f_{ACO_2}, V_A (t), V_d and F (Fig. 8.1) respectively represent dead space CO_2 fraction, alveolar CO_2 fraction, alveolar volume, dead space subcompartment volume and breathing airflow. F_{nhf} is the applied NHF flow rate. The volume of the dead space (all subcompartments together) is denoted as V_D.

8.2.2 Gas exchange equations

The pulmonary capillaries are also lumped into one unit, which exchanges O_2 and CO_2 with the alveolar compartment. The system of equations which describe gas exchange (Eq. 8.1 to Eq. 8.7) assume the following:

- There is no gas diffusion across the walls of the dead space
- There is instantaneous mixing of gas within the alveolar unit
- Metabolic CO_2 production and O_2 exchange occur at a constant rate.

$\dot{V}_{O_2}$ and $\dot{V}_{CO_2}$ (Fig. 8.1) are the O_2 and CO_2 fluxes across the blood gas interface and have values of 0.0035 L/s and 0.005 L/s (Benallal and Busso (2000)) respectively at steady state.

The rate of accumulation of CO_2 fraction in the first dead space unit, the one nearest the nose (n = 1) during inspiration is defined in Eq. 8.1. (Benallal et al. (2002))

$$\left(\frac{dfd_{CO_2}}{dt}\right)_1 = \frac{F[fi_{CO_2} - (fd_{CO_2})_1]}{V_d} \tag{8.1}$$

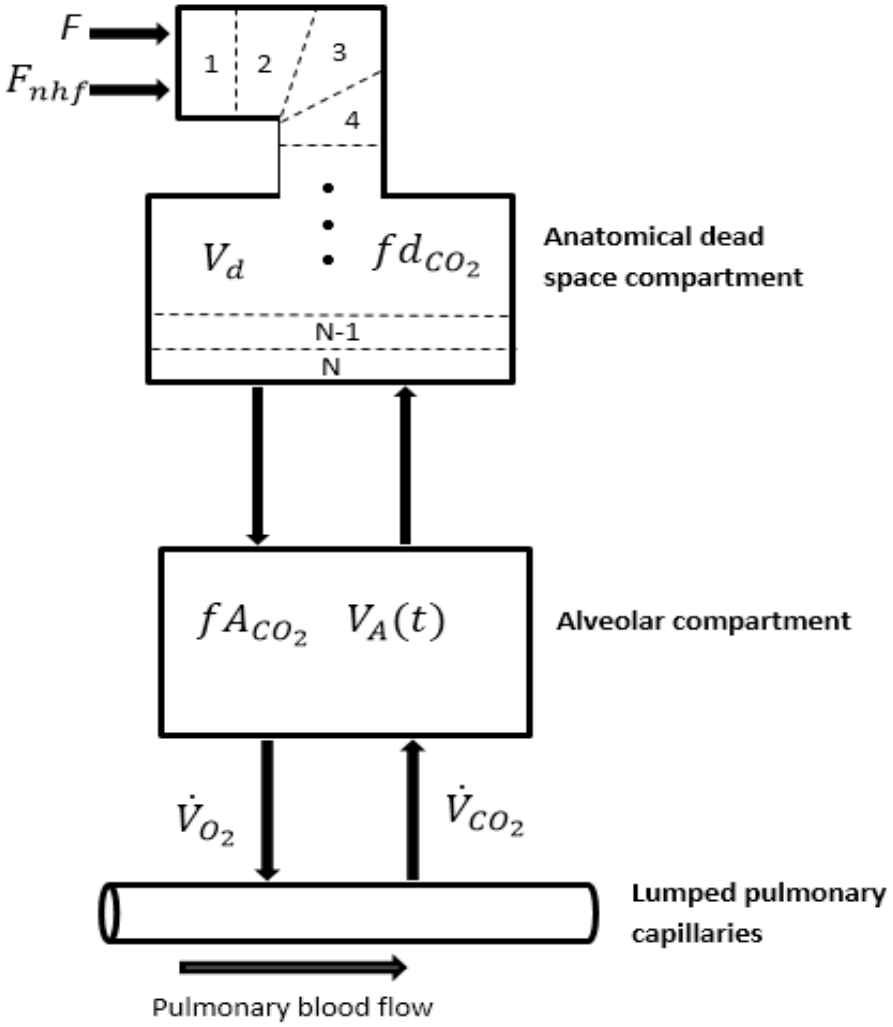

Fig. 8.1 A two-compartment model of the respiratory system (adapted from Benallal et al. (2002))

where fi_{CO_2} is the inspired CO_2 fraction from the atmosphere. The accumulation of CO_2 fraction in the subsequent dead space compartments and the alveolar unit are respectively described by Eq. 8.2 and Eq. 8.3

$$\left(\frac{dfd_{CO_2}}{dt}\right)_{n+1} = \frac{F[(fd_{CO_2})_n - (fd_{CO_2})_{n+1}]}{V_d} \tag{8.2}$$

$$\frac{dfA_{CO_2}}{dt} = \frac{\dot{V}_{CO_2} + F[fd_{CO_2}]_N - f_{ACO_2}Q_A}{V_A(t)} \tag{8.3}$$

where the index n = 1,2,3…N respectively represent the first, second, third up to the last dead space control volume (N). Q_A is the total gas flux into the alveolar unit at any given time and is defined by the conservation of mass (Eq. 8.4). Eq. 8.1 - 8.3 represent convective fluxes from one subcompartment to the next with diffusion assumed to be negligible in the dead space.

$$Q_A = F - \dot{V}_{O_2} + \dot{V}_{CO_2} \tag{8.4}$$

The rate of change of CO_2 fraction in the alveolar unit, the dead space compartment closest to the alveolar unit, and the subsequent dead space compartments during expiration are accordingly described by Eq. 8.5, Eq. 8.6 and Eq. 8.7.

$$\frac{df_{ACO_2}}{dt} = \frac{\dot{V}_{CO_2} - F[fd_{CO_2}]_N - fA_{CO_2}QA}{V_A(t)} \tag{8.5}$$

$$\left(\frac{dfd_{CO_2}}{dt}\right)_N = \frac{F[fA_{CO_2} - (fd_{CO_2})_{N-1}]}{V_d} \tag{8.6}$$

$$\left(\frac{dfd_{CO_2}}{dt}\right)_n = \frac{F[(fd_{CO_2})_n - (fd_{CO_2})_{n-1}]}{V_d} \tag{8.7}$$

where n = N, N-1, N-2,….3, 2, 1. The equations describing O_2 transport are identical in form to Eq. 8.1 through Eq. 8.7 (which are for CO_2 transport).

The volume of the airway from the nostril up to the end of the trachea is about 80 ml (which is about half of the dead space volume of 150 ml) (Leader et al. (2004); Zheng et al. (2000)). Gas was sampled from the model trachea (n = 20). In the experimental work conducted to validate the results from the present model, gas was sampled at the tracheal. Note that mixing is essentially instantaneous in each subcompartment and this can lead to unphysically high transport rates unless sufficient compartments are used. By having too few compartments and instantaneous mixing throughout a compartment, the rate at which changes in CO_2 concentration are communicated downstream is unphysically high, though the overall transport rate will be correct (injected CO_2 will be transported too fast, but also

diluted too much). Where reference is made to the nostril it is in regards to the first dead space control volume (n=1).

8.2.3 Lung mechanics

In the setup of the lung mechanics, the following assumptions were made:

- The rate of change of lung volume is equal to the breathing flow i.e. the air is incompressible
- The pleural pressure is equally distributed over the lung
- The lung is homogenous and has equally distributed elastance

Alveolar volume (V_A (t)) varies with the driving function, which is the pleural pressure (P_{pl}). The P_{pl}, which is defined in terms of other lung parameters (of the form used by Ben-Tal (2006)) as shown here in Eq. 8.8 was used in this model.

$$P_{pl} = P_{atm} - R\left(\frac{V_t}{2}\right)\sin(wt) - E(FRC - \left(\frac{V_t}{2}\right)\cos(wt)) \tag{8.8}$$

where P_{atm}, R, V_t, E and FRC respectively denote the atmospheric pressure, linear airway resistance, tidal volume, lung elastance and functional residual capacity for which estimates are available. The values of these parameters are specified in Table 8.2.

The flow of air, F during breathing is defined as the rate of change of alveolar volume, V_A (t) as shown in Eq. 8.9.

$$F = \frac{dV_A(t)}{dt} \tag{8.9}$$

Inspiratory flow commences when the alveolar pressure (P_A) is lower than the atmospheric pressure (P_{atm}). A higher P_A is however required to drive expiration. The relationship between the forcing function of the system, P_{pl} and P_A (as in Ben-Tal (2006)) is presented in Eq. 8.10.

$$\frac{dP_A}{dt} = \frac{P_{atm}E}{P_A} + \frac{dP_{pl}}{dt} \tag{8.10}$$

The system of ordinary differential equations (ODEs) defined by Eq. 8.1 through Eq. 8.10 were solved using the ODE solver, odeint , implemented in python 3.5. A timestep of 0.05 seconds was used for the simulation (no significant change in CO_2 was observed with lower values). Table 8.1 summarizes all the quantities that can be predicted with the present model. All parameters used in the present model along with their values are presented in Table 8.2.

Table 8.1 A list of quantities predicted by the model

Quantity	**Parameter**
Gas exchange	
$\mathbf{fd}_{O_2}$	Dead space O_2 fraction
$\mathbf{fA}_{O_2}$	Alveolar O_2 fraction
$\mathbf{fd}_{CO_2}$	Dead space CO_2 fraction
$\mathbf{fA}_{CO_2}$	Alveolar CO_2 fraction
$\mathbf{V}_A$ **(t)**	Alveolar volume
Lung mechanics	
F	Breathing flow
$\mathbf{P}_A$	Alveolar pressure

Table 8.2 Inputs to the model

Quantity	Symbol	value	Reference
O_2 exchange flux	D_o	0.005 L/s	Benallal et al. (2002)
Metabolic CO_2 flux	D_c	0.004 (L/s)	Benallal et al. (2002)
Initial alveolar O_2 concentration	iC_{o_2}	0.136	Ben-Tal (2006)
Initial alveolar CO_2 concentration	iC_{co_2}	0.052	Ben-Tal (2006)
Atmospheric pressure	P_{atm}	760 (mmHg)	Ben-Tal (2006)
Atmospheric O_2 concentration	$Patm_{O_2}$	21 %	Ben-Tal (2006)
Atmospheric CO_2 concentration	$Patm_{CO_2}$	0.04 %	Benallal et al. (2002)
Vapor pressure of H_2O @ 37°	pw	47 mmHg	Ben-Tal (2006)
Dead space volume	V_d	0.15 L	Benallal et al. (2002)
Tidal volume	V_t	0.5 L	Tobin et al. (1983)
Breathing period	T	4.35 s	Tobin et al. (1983)
Functional residual capacity	FRC	2.5 L	Benallal et al. (2002)
Lung elastance	E	8 cmH_2O/L	Otis et al. (1950)
Linear resistance	R	2 cmH_2O/L/s	Sharp et al. (1964)
Nasal high flow	NHF	0-60 L/min	Ward (2013)

8.3 Results

8.3.1 Healthy adult breathing

The P_{Pl} and P_A for a healthy state are presented in Fig. 8.2. P_{Pl} starts falls from -7.3 cmH_2O at the start of inspiration to -12.7 cmH_2O at the end of inspiration (Fig. 8.2) and over this period, alveolar pressure falls to a peak of -1.5 cmH_2O, returning back to (atmospheric pressure) by the close of inspiration. The breathing flow pattern, tidal volume profile and

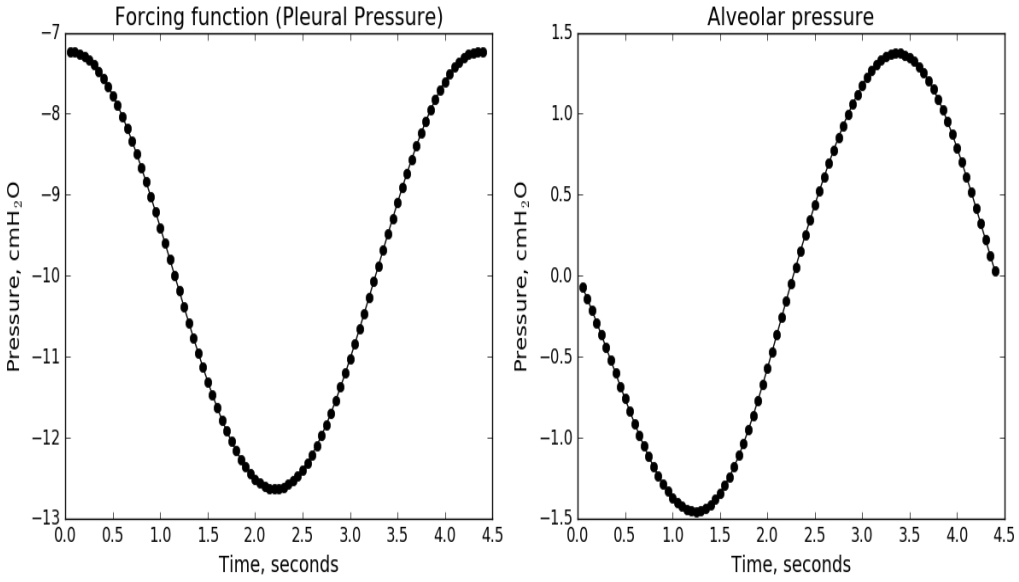

Fig. 8.2 Forcing function (pleural pressure) and the predicted alveolar pressure

P_{Pl} versus tidal volume loop are shown in Fig. 8.3. It is seen that the breathing flow has an I:E ratio of 1 which is unphysical. This is recognised as a limitation which can be addressed by defining a pleural pressure (driving function) which can produce a breathing flow with physiological I:E ratio. This limitation may affect $EtCO_2$ as seen in Chapter 7. It is however observable that the breathing flow and alveolar pressure patterns are similar. The tidal volume profile reaches a peak of 0.44 L by the end of inspiration. The area enclosed by the P_{Pl} versus tidal volume loop denote the total work of breathing (elastic plus resistive).

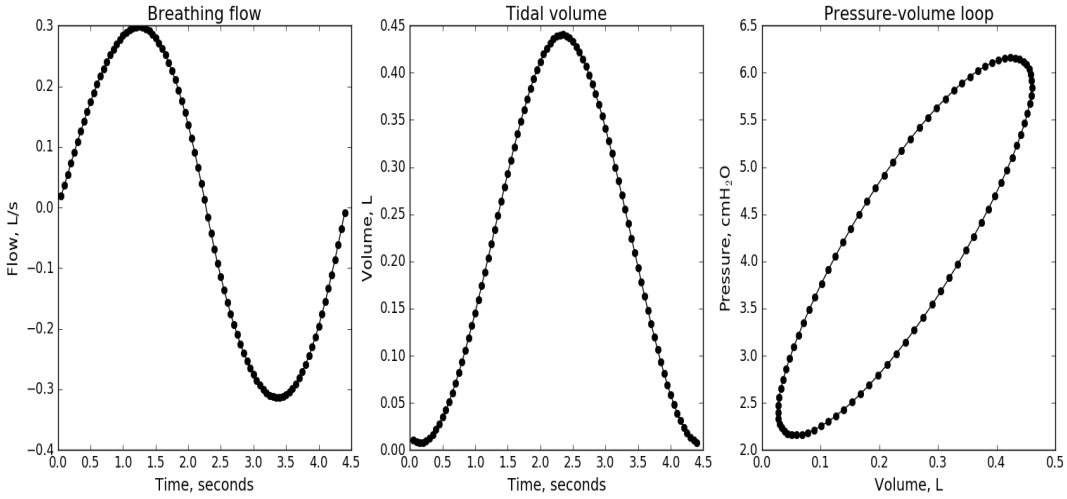

Fig. 8.3 Breathing flow, tidal volume profile and pressure-volume curve

The dependency of the O_2 and CO_2 partial pressures (sampled from the trachea, n = 20) on dead space mesh size (number of control volumes of the dead space) was explored. The capnograms obtained by setting the mesh size (N) to 2, 10, 20, 30 and 40 are indicated in Fig. 8.4. The difference in peak CO_2 concentration between N = 30 and N = 40 is 0.02 %. Note that the plateau phase of a capnogram (Chapter 1, Fig. 1.8) indicates the expulsion of mixed alveolar and dead space air. The increase in flatness of the plateau region (1.5 s $<$ time $<$ 3 s) with mesh size shows that finer mesh increases rate of mixing of alveolar and dead space gas. N = 30 was used.

In Fig. 8.5 the O_2 (Fig. 8.5a) and CO_2 (Fig. 8.5b) gas tensions in the alveolar unit, the trachea (n = 16) and the nostril (n = 1) are shown for 25 breathing cycles. The model is initialized to assumed CO_2 and O_2 concentrations which converge to a steady cycle after 50 seconds (12 cycles). Tracheal and nasal O_2 peak values are equal to that in atmosphere (150 mmHg). The minimum tracheal and nasal O_2 tension approaches the mean alveolar O_2 tension (97 mmHg). The maximum alveolar O_2 tension is about 100 mmHg and never reaches the atmospheric value (760 mmHg). The tracheal and nasal CO_2 peaks near alveolar CO_2 peak (pure lung air reaching trachea unmixed with fresh air) but do not reach it (42

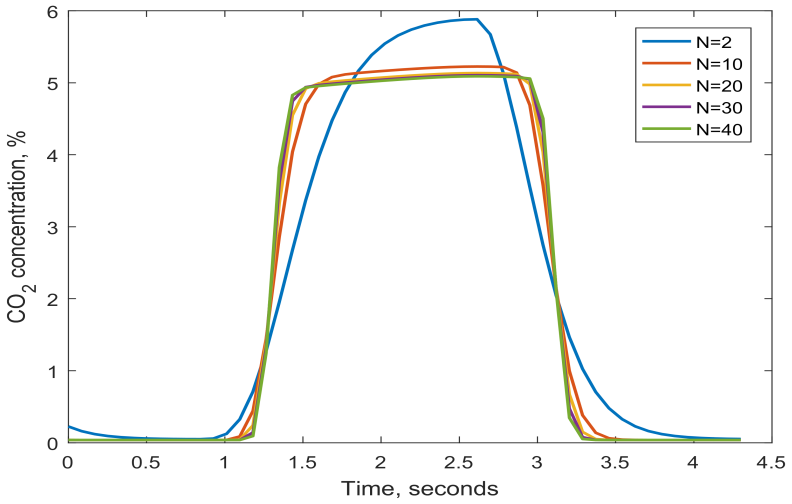

Fig. 8.4 Effect of mesh size on CO_2 concentration

mmHg). The minimum tracheal and nasal CO_2 tension nears atmospheric value (0.3 mmHg) but the alveolar CO_2 concentration never reaches this low.

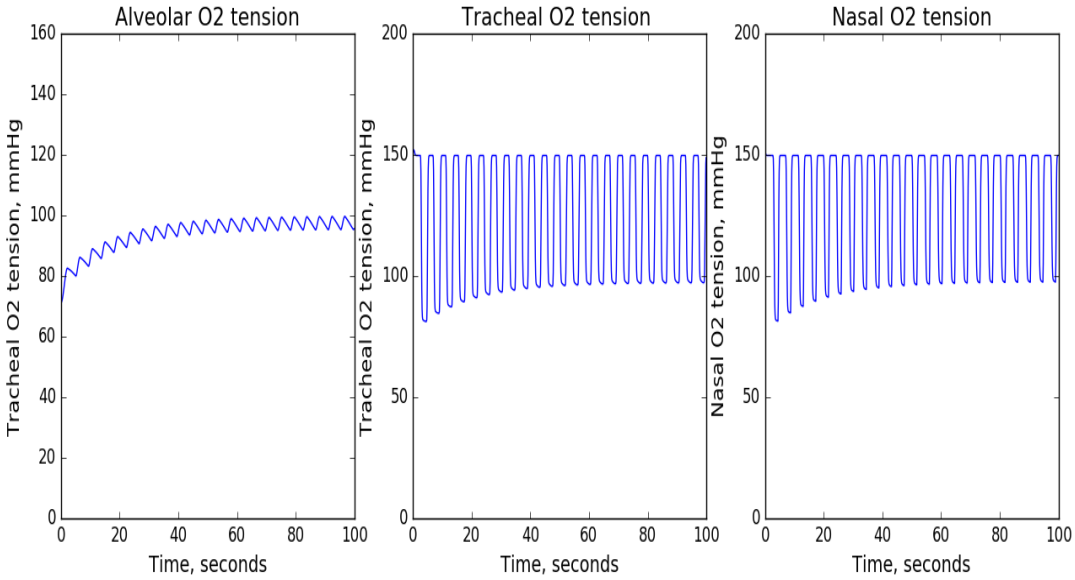

(a) Alveolar, tracheal and nasal O_2 tension

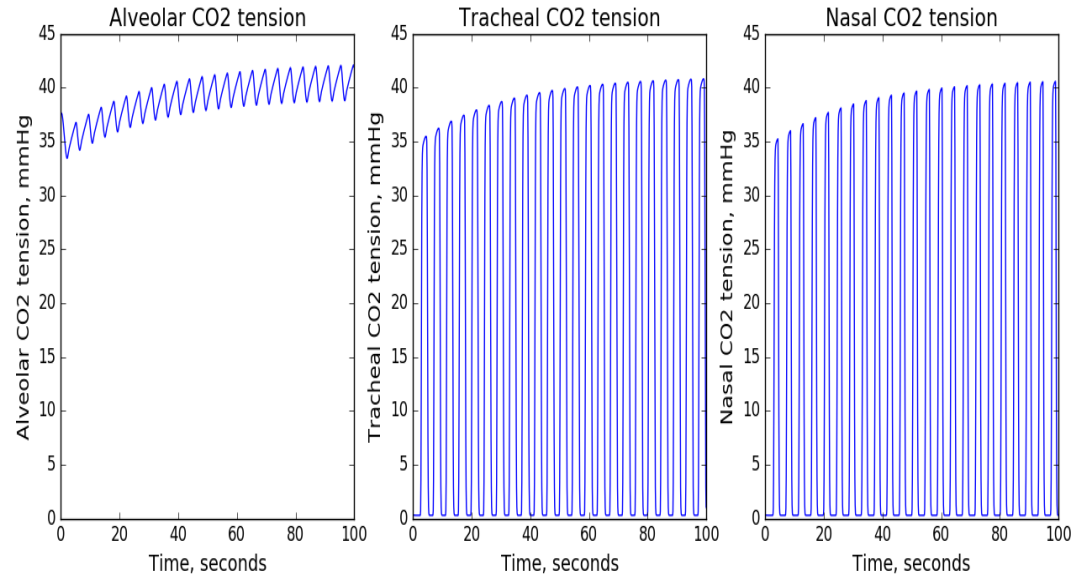

(b) Alveolar, tracheal and nasal CO_2 tension

Fig. 8.5 Peak alveolar, tracheal and nasal O_2 are 97 mmHg, 150 mmHg and 150 mmHg. Corresponding values for CO_2 are 42 mmHg, 40.5 mmHg and 39 mmHg

8.3.2 Validation

The tracheal concentration of CO_2 obtained from the model has been compared to bench-top experimental results conducted with the setup shown in Chapter 6. In the experiment, CO_2 was bled at a rate of 98 scc/min (with CO_2 source pressure maintained at 20 KPa) to produce a CO_2 concentration of 5.3 % in the trachea (equivalent to 40.3 mmHg).

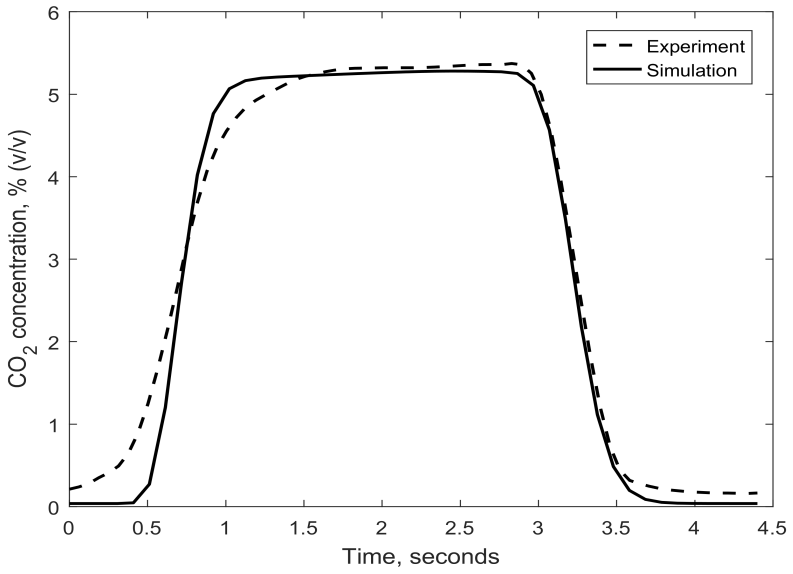

Fig. 8.6 Simulated and experimental CO_2 profiles during spontaneous breathing

The model and experimental capnograms were compared (Fig. 8.6). It is seen that the $EtCO_2$ concentration of both experiment and simulation agree and their rise and fall times also agree. The CO_2 profile of the model has a sharper rising phase than the experimental CO_2 profile though the slope of the falling phase are same for both. The instantaneous mixing in the model and difference in metabolic CO_2 flow rate between model and experiment may account for this difference. The difference in flow patterns (See Fig. 8.7) may also be a factor.

Table 8.3 shows a summary of quantities pertinent to the healthy state, derived from the plots shown in Fig. 8.3 and Fig. 8.5. Published data on these quantities are also presented. Note that some of the references are from restricted populations and may vary for individuals.

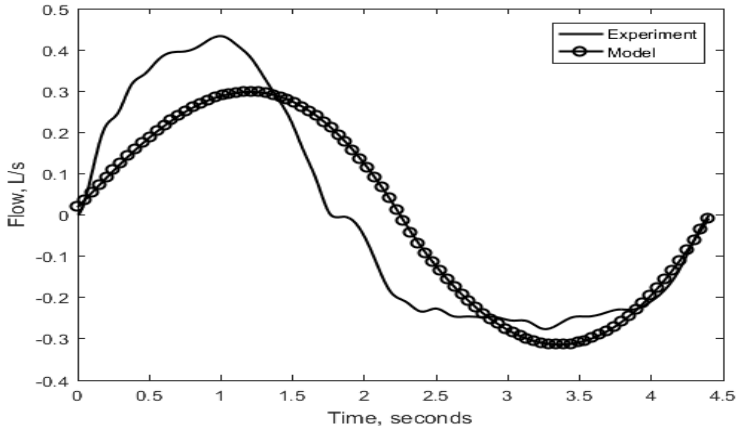

Fig. 8.7 Simulated and experimental flow profiles during spontaneous breathing

It is seen that the model results are realistic and comparable to simulated and physiological findings of other workers.

Table 8.3 A comparison of model results to published data

Parameters	Simulation	Published data	References
Gas exchange			
Peak tracheal O_2 (mmHg)	150	153	Ferris et al. (1946)
end-tidal CO_2 (mmHg)	38.6	36	Veronez et al.(2010)
Peak alveolar O_2 tension (mmHg)	100.5	103.5	Busso and Robbins (2000) (simulation)
Peak alveolar CO_2 tension (mmHg)	42.4	39	Benallal and Busso (2000) (simulation)
Lung mechanics			
Peak alveolar pressure (cmH_2O)	1.5	1.2	Sondergaard et al. (2003)
Pleural pressure (cmH_2O)	-7.2 to -12.5	-5 to -8	Guyton and Hall, 2006
Tidal volume (L)	0.44	0.5	Tobin et al. (1983)
Work of breathing (J/breath)	0.28	0.24	Cabello and Mancebo (2006)

8.3.3 Application of nasal high flow

In the lung, gas exchange occurs via molecular diffusion however expulsion of CO_2 from the lungs into the atmosphere predominantly occurs via advection. It has been experimentally observed that when NHF therapy is applied, 'the cannula jet drives the flow backward through the upper portion of the nasal cavity until the flow turns in the nasopharynx and flows forwards along the nasal cavity floor' (Spence (2011)). The recirculation of air in the nasal cavity augments mixing and the clearance of CO_2 from the anatomic dead space (Spence (2011)). This prevents the rebreathing of CO_2-rich gas into the lungs. In a previous collaborative work, Chapter 5 (see Van Hove et al. (2016)) a more sophisticated CFD model was used to predict CO_2 tension in the trachea. Here, a simple idea was explored. Spence (2011) found that the velocity of the cannula flow decreases with distance from the nostril towards the nasopharynx. Consequently, it was thought that only a fraction of the cannula jet reached the nasopharynx, turned around, moved forward along the nasal cavity floor and exited through the nostril. The remaining fraction exited via the nostril without reaching the nasopharynx. This condition was modelled by adding a specified amount of the NHF rate (3 %, 5 %, and 10 % were investigated) to the lung flow reaching the nasopharynx during expiration (i.e. F+ F_{nhf}) and substituting this into Eq. 8.9 (as shown in Eq. 8.11). NHF was not added to the inspiratory flow as this would increase tidal volume. In the bench-top model NHF doe not increase tidal volume.

$$\left(\frac{dfd_{CO_2}}{dt}\right)_n = \frac{(F + \%F_{nhf})[(fd_{CO_2})_n - (fd_{CO_2})_{n-1}]}{V_d} \tag{8.11}$$

8.3.4 Validation

The $EtCO_2$ for NHF of range 0 - 60 L/min, as sampled from the trachea (n = 20) is compared with corresponding experimental results (Chapter 6) in Fig. 8.8. It is noticeable that modelling the jet flow which flushes the nasopharynx as 3 % of NHF best agrees with the experimental results for all NHF. The point-by-point deviation of the model results from the experimental

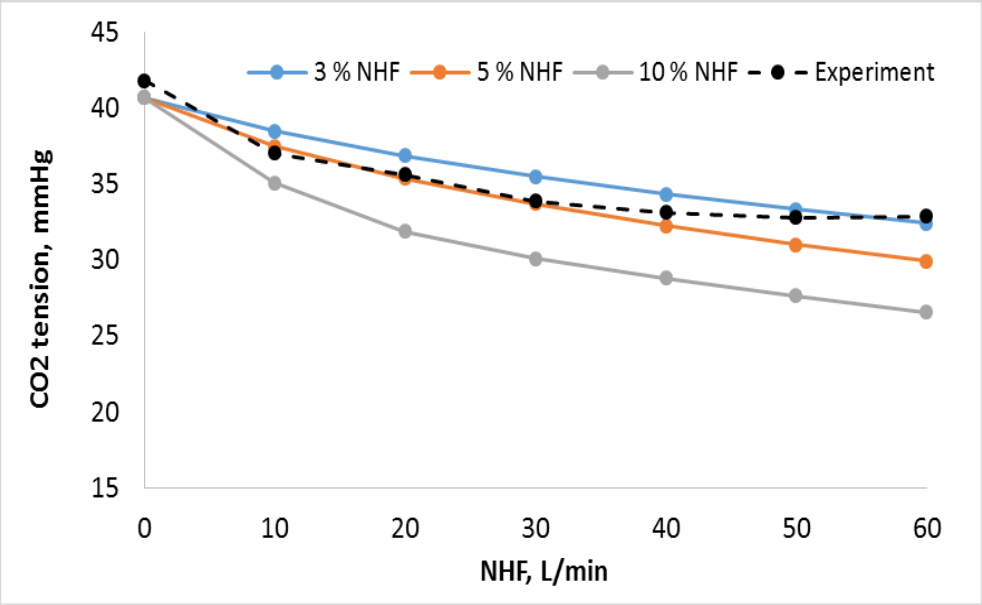

Fig. 8.8 Prediction of $EtCO_2$ during NHF. Continuous lines represent model predictions and dashed line represents experimental observation

values was quantified using the root mean square deviation (RMSD) defined by Eq. 8.12

$$RMSD = \sqrt{\frac{\sum_{i=1}^{j} Experiment_i^2 - Simulation_i^2}{j}} \tag{8.12}$$

where J and i are the number of data points and data index respectively. The RMSD using 3 % NHF, 5 % and 10 % of NHF were found to be 8.4, 8.6, and 15.5 respectively. 3 % of NHF flow was used. It is noted that the NHF geometry of the airway at certain points in the physical upper airway may promote turbulence and enhance mixing. Such a property is missing in the present model. Also, modelling of turbulent mixing between the cannula jet and surrounding air is absent.

In Fig. 8.9, the model and experimental capnograms at NHF of 30 L/min are shown. The experiment and simulation agree in terms of $EtCO_2$ (0.1 % (v/v) difference), and rise and fall times. The sharp rise of the model capnogram relative to experiment is due to difference in mixing.

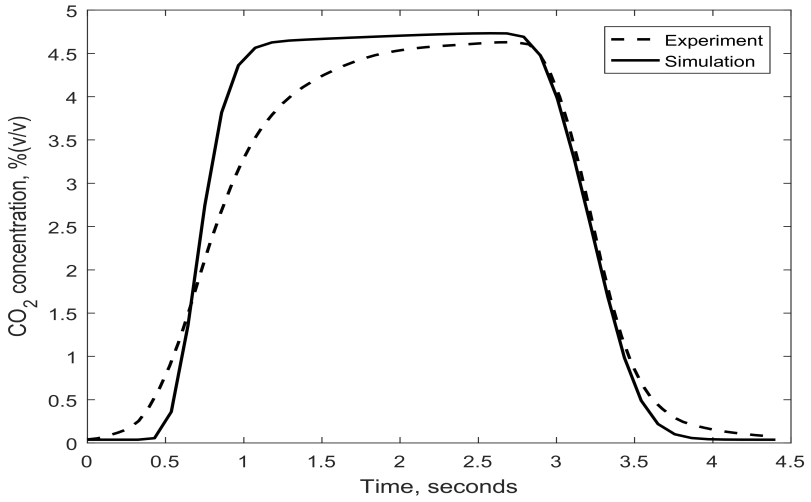

Fig. 8.9 Simulated and experimental CO_2 profiles for 30 L/min NHF

8.3.5 Central sleep apnea

Central sleep apnoea is the cessation of breathing when the blood CO_2 tension falls below the breath-activation threshold. This may occur for several seconds. In Chapter 6, the maximum $EtCO_2$ for CSA of durations of 10 seconds (CSA10), 20 seconds (CSA20), 30 seconds (CSA30) and 40 seconds (CSA40) were investigated for no NHF and NHF ranging from 10 L/min to 60 L/min using a bench-top setup. A similar results obtained from the mathematical model is presented in Fig. 8.10. The alveolar and tracheal $EtCO_2$ reach a steady state at time = 50 seconds (12 cylces). The initiation of apnea at time = 170 seconds (Fig. 8.10) produces a steady rise in alveolar CO_2 tension with the peak value depending on the duration of the CSA. When breathing resumes, the maximum $EtCO_2$ is produced by the first breath. The $EtCO_2$ then falls steadily and reaches the steady value prior to CSA.

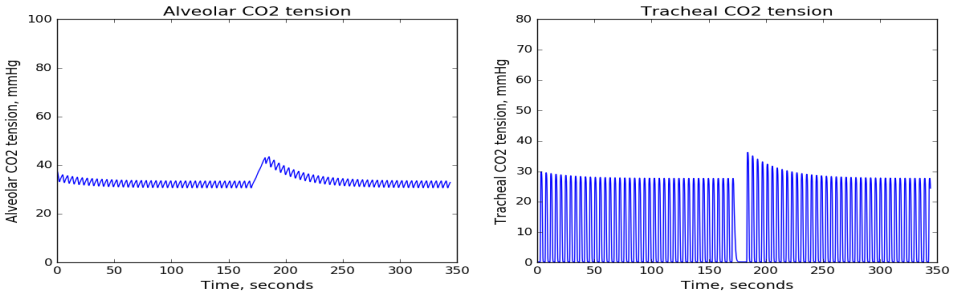

(a) Alveolar and tracheal CO_2 profiles during CSA10

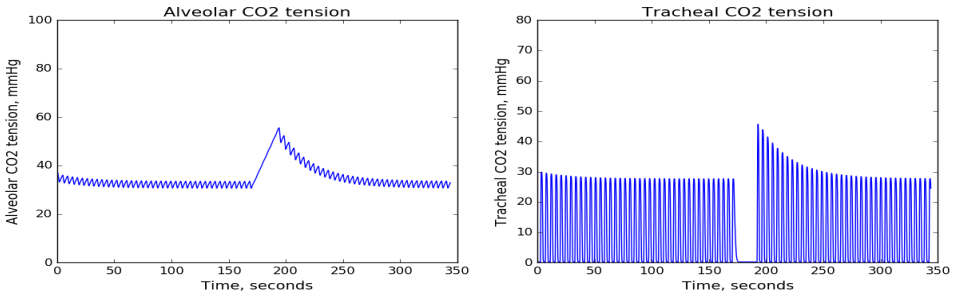

(b) Alveolar and tracheal CO_2 profiles during CSA20

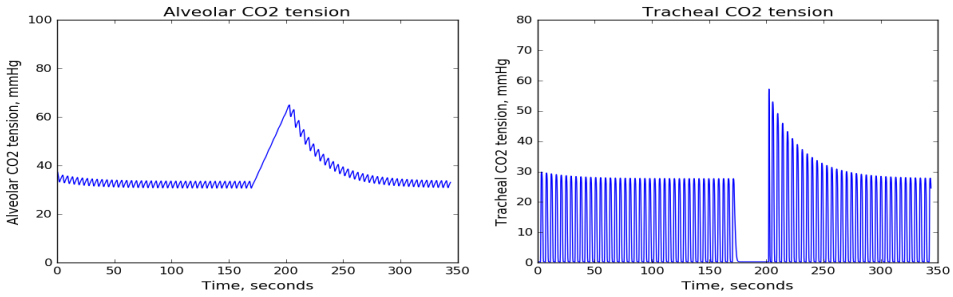

(c) Alveolar and tracheal CO_2 profiles during CSA30

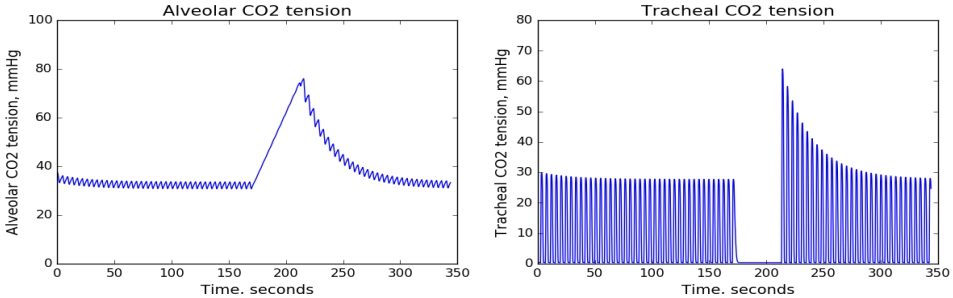

(d) Alveolar and tracheal CO_2 profiles during CSA40

Fig. 8.10 Alveolar and tracheal capnograms during CSA of 10 to 40 seconds

8.3.6 Validation

A plot of the maximum $EtCO_2$ for CSA10 to CSA40 at NHF of 0 - 60 L/min have been superimposed on the experimental results (Fig. 6.4 of Chapter 6) as shown in Fig. 8.11. The error bars represent 2 standard deviations in measurement of maximum $EtCO_2$ over 120 cycles. The results from the mathematical simulation agree in trend with the experimental results

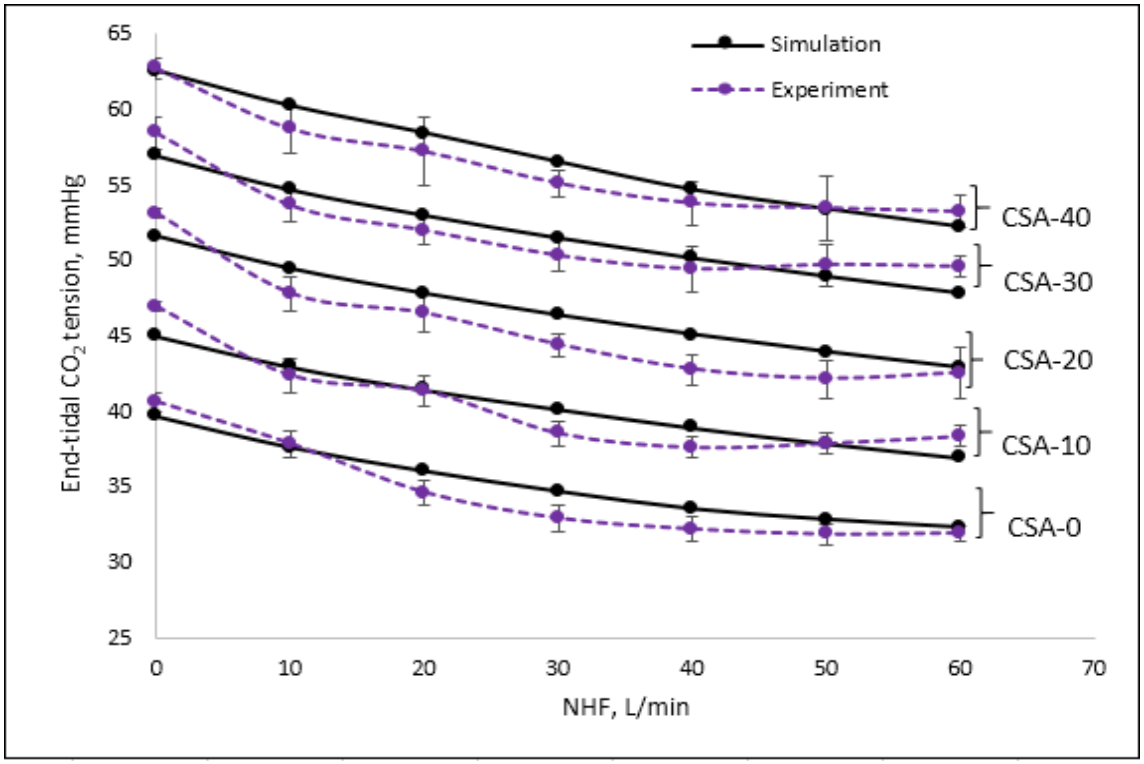

Fig. 8.11 Peak CSA CO_2 tension versus NHF obtained via simulation and experiment

(maximum $EtCO_2$ reduces with NHF). Quantitatively, the mathematical model predicts the experimental results quite well. The amount of NHF reaching the nasopharynx was assumed to be 3% for all NHF.

At NHF = 0 (Fig. 8.10) $EtCO_2$ is noted to rise from 40 mmHg to 62 mmHg during CSA-40 (over 40 seconds) which corresponds to a rise rate of 0.6 mmHg/second. CO_2 rise rates have been reported to range from 0.001- 0.2 mmHg/second (Patel et al. (2011); Stocks and Godfrey (1978)). It is however reported during apnea, arterial CO_2 rises sharply in the first minute after which it gradually plateaus towards a saturation value (Stock et al. (1989)).

The difference may be due to buffering of arterial CO_2 by bicarbonates (absent in the present model) and constant CO_2 flow rate used in the present model unlike the diffusion-driven flow in the physiological system.

8.4 Discussion

The need to predict the $EtCO_2$ tension when NHF is applied was a motivation for this work. The capnogram predicted by the mathematical model and experiment (for both spontaneous and NHF breathing) agreed in $EtCO_2$, morphology and rise and fall times. The slope of the falling edge also agreed however due to mixing the slope of the rising edge was sharper for the model capnogram. The mathematical model assumes instantaneous mixing in alveolar chamber.

The experiment and mathematical model produced $EtCO_2$ tensions of about 37 mmHg (5 % concentration) during spontaneous breathing. This value is within the physiological range (35 - 40 mmHg) for healthy adults (Ritchie et al. (2011)). The mean alveolar CO_2 fraction of 40 mmHg falls within the reported physiological range of 35 mmHg to 45 mmHg (Allen and Jones (1984)). During spontaneous breathing, the mean arterial CO_2 partial pressure (P_aCO_2) approximates the mean alveolar CO_2 partial pressure (P_ACO_2) (Benallal et al. (2002)).

A simple assumption was made that a fraction of NHF flow (3 %) reaches the nasopharynx, returns and adds to the expiration flow to flush the nasopharynx and nasal cavity of CO_2 convectively. The predictions of $EtCO_2$ made by the model (during NHF administration) appreciably agreed with experimental results. The model predicted the maximum $EtCO_2$ during apnea quite well for apnea of durations 10, 30 and 40 seconds. The rise rate of $EtCO_2$ over an apnea time of 40 seconds was found to be the same order of magnitude as clinically observations (Patel et al. (2011); Stock et al. (1989); Stocks and Godfrey (1978)). A mathematical model for turbulence diffusion in the nasal cavity may improve the present

results. Limited time did not allow the inclusion of such a model. Addition of such a model will eliminate the current value of 3 % of NHF reaching the nasopharynx.

8.4.1 Limitations of the model

The alveolar partial pressure of CO_2 depends on alveolar ventilation and metabolic CO_2 production. In both experimental and mathematical models, the CO_2 bleed rate was assumed to be constant though in the physiological system it varies depending on the bodies metabolism. Also, in the physiologic system, the alveolar CO_2 is influenced by CO_2 gradient between pulmonary capillaries and the alveolar unit. Furthermore, blood transport delays from the heart to the alveoli, and equations describing, biocarbonate chemistry, oxygen binding and dissociation with haemoglobin have not been included. Also, an abnormality in airway geometry in the form of a protrusion can reduce dead space and introduce turbulence which may improve mixing. The influence of geometry is however not incorporated into the model.

8.5 Conclusion

The two-compartment model predicts the CO_2 profiles observed during spontaneous breathing. Breathing under NHF conditions was modelled by adding 3 % of NHF flow to the expiratory flow. The model $EtCO_2$ results for apnea NHF ranging from 10 L/min to 60 L/min were close to in vitro experimental results. Over an apnea time of 40 seconds, $EtCO_2$ rose at a rate of 0.6 mmHg/seconds, which agrees with clinical observations.

Chapter 9

Conclusions and Future Work

9.1 Conclusions

Nasal high flow (NHF) therapy has been reported to increase airway pressure and tidal volume (V_t) but reduce respiratory rate (RR). How these findings affect the work done to overcome airway resistance has been unclear. To fill this gap in literature, NHF was applied via three different cannula sizes to 3-D printed neonate and the adult upper airway models (in mouth closed and open state). Pressure drop and flow rate were measured and used to estimate inspiratory and expiratory resistances. The resistance information was used to compute the muscular work required to overcome the resistance to flow.

Airway pressure was found to increase with NHF in both neonate and adult models. The large cannula produced the greatest tracheal pressure in the mouth closed breathing state (adult model) corresponding to to a rise of 6 - 14 % (depending on flow direction and NHF) relative to the small cannula. The medium and large cannula produced comparable tracheal pressure. In the mouth open state (adult model), the small cannula produced the greatest tracheal pressure in the range of 9 - 23 % (depending on NHF flow) relative to the large cannula. The medium and small cannula produced comparable tracheal pressure. At all NHF and all breathing flows, the tracheal pressure for mouth closed breathing was found to

be about 3 times that of mouth open breathing. Mouth open breathing requires air leakage via the oral passage and nasal passage (greater leakage area) which is accompanied by less molecular gas collision (lower pressure) unlike mouth open breathing where all the flow exits via the nasal passage (small leakage area, greater pressure). The upper airway resistance in the inspiration direction was greater than during expiration. This was due to a greater rate of change in pressure during inspiration. The ratio of expiratory to inspiratory tracheal pressure increased with NHF for both mouth closed and open states. In mouth closed state, tracheal pressure in expiration was higher than that of expiration by 9 %, 72 % and 103 % respectively for NHF20, NHF40 and NHF60. In mouth open state, 11 %, 88 % and 125 % corresponded to NHF20, NHF40 and NHF60. The upper airway resistance of the neonate model was a factor of 4 greater than the adult model at peak inspiratory flow of 5 L/min and 30 L/min repectively for the neonate and adult.

NHF can provide part or all of the pressure required to drive the inspiration breathing flow through the upper airway. This known as the ZPIF effect. This reduces inspiratory work of breathing. Expiratory work of breathing increases with NHF as the momentum of the NHF jet must be negated by the expiratory flow. Total work of breathing (inspiration plus expiration) increases if minute volume does not change when NHF is applied. Work of breathing reduces in NHF dependent manner if the RR and minute volume fall with NHF. NHF has been observed to do so in COPD patients (Braunlich et al, 2013). A fall in minute volume by 40 % reduced rWOB/min by 90 % (at NHF of 60 L/min) compared to a no NHF condition. Work of breathing may fall further with a fall in I:E ratio. Mouth closed breathing demanded 3 times the work of breathing as mouth open breathing (if minute volume is assumed to for by the same amount for both mouth states). Neonatal work of breathing also falls with minute volume.

A CO_2 flushing mechanism (reduction in dead space CO_2 concentration due to NHF) is believed to be responsible for the observed increase in oxygenation when NHF is applied. An in vitro experiment using an anatomically accurate airway model and a physiological

breathing waveform to find the change in end-tidal CO_2 concentration with and without NHF. The results showed that end-tidal CO_2 decreased in an NHF-dependent manner until NHF of 40 L/min and plateaus. The CFD results of others (Van Hove et al. (2016)) show recirculation in the anterior portion of the nasal cavity. This causes the CO_2 rich gas to vent from the nostrils reducing the CO_2 concentration in the dead space and lowering the inspired CO_2 volume (by 65 % at NHF of 60 L/min). This explains the fall in end-tidal CO_2 concentration in the in vitro experiment.

NHF is used to treat obstructive sleep apnea but its efficacy in relieving central sleep apnea (CSA) patients has not been reported. It was thought that a reduction in end-tidal CO_2 tension ($EtCO_2$) during apnea can mitigate the frequency of apnea occurrence. A piston pump drove a realistic breathing flow pattern through an upper airway model. Apnea intervals of 10 - 40 seconds were mimicked with and without NHF. The maximum $EtCO_2$ rose with apnea duration, and at zero NHF its value for CSA of 10 and 40 seconds were 6.2 % (v/v) and 8.2 % (v/v) respectively, which correspondingly reduced to 4.9 % (v/v) and 7 % (v/v) when NHF of 60 L/min was applied. Note that the physiological $EtCO_2$ for a healthy adult is about 5.3 % (v/v). NHF of 60 L/min reduced $EtCO_2$ (at CSA of 40 seconds) by 18 %. Since $EtCO_2$ reflects alveolar CO_2 tension and a lower $EtCO_2$ prior to CSA reduces the susceptibility of individuals to CSA, it is concluded that NHF may reduce the spate of CSA in patients. The rate of rise of $EtCO_2$ (33 mmHg/min at CSA of 40 seconds) is noted to be an order of magnitude higher than the rise rate reported in the literature (5 mmHg/min) (Patel and Nouraei (2015); Stock et al. (1989)).

A rise in alveolar CO_2 leads to a rise in ventilation which in turn reduces alveolar CO_2 (negative feedback mechanism). It was speculated that, aside from breathing frequency and tidal volume, the shape of the breathing waveform may be optimized to change $EtCO_2$. Thus, the goal was to find out if the breathing flow pattern alone can modify end-tidal CO_2 ($EtCO_2$) and if so, to what extent. Four breathing flow patterns belonging to Stage III COPD patients and one healthy breathing flow pattern were collected. These were scaled to the

same tidal volume, respiratory rate and I:E ratio, leaving flow pattern as the only varying parameter. In vitro measurement of $EtCO_2$ with and without NHF revealed that breathing flow patterns varying only in shape can produce statistically significant difference in $EtCO_2$. The variability in $EtCO_2$ was however found to be small (1 - 2 %). A 35 % fall in I:E ratio (all other parameters kept the same) corresponded to a 2 % rise in $EtCO_2$. It is concluded changes in $EtCO_2$ due to shape and I:E ratio are small.

A two compartment mathematical model was used to predict the airway capnogram, with and without NHF. The capnogram predicted by the model agree in shape, $EtCO_2$ and rise and fall times. The effect of NHF was modelled by adding a fraction of the NHF flow reaching the nasopharynx. The maximum $EtCO_2$ due to apnea as measured from an in vitro studies generally agreed with the model results.

9.1.1 Original contributions

- First estimation of upper airway resistance during NHF in an anatomically realistic upper airway model (in the inspiration and expiration direction) which is impossible to measure in vivo.
- First quantitative estimation of resistive work of breathing during NHF in an anatomically realistic upper airway model using clinically reported NHF-induced changes in breathing parameters.
- First estimation of the effect of cannula size on airway resistance in an anatomically realistic upper airway model. Such estimates are difficult to make in vivo.
- A predictive model for fall in end-tidal CO_2 concentration with NHF. This estimates alveolar CO_2 concentration rate of rise during apnea, and rate of fall after breathing recommences under NHF conditions.

9.2 Future work

In the present study, the characterization of tracheal pressure was restricted to one airway geometry of an adult and a neonate. The insight into how NHF affects airway resistance has been profound, nonetheless a study looking into the variation of resistance across a human age spectrum will be interesting as an anthropometric quantity (e.g. body mass, metabolic rate or a linear dimension) that scales well with resistance coefficients may be found. This will involve repeating the methods used in Chapter 3 and 4 for upper airway models of different geometries and sizes. Also, the model would benefit from the inclusion of a wet lining to mimic mucus, compliance in soft palate and tongue would be a benefit. It will also be interesting to find how resistance varies in models of the same geometry but different sizes. Further, identifying areas of the airway that provide the most variation in resistance in disease state will be insightful. This can be accomplished by making measurements in a range of geometries including different obstructive and resistive disease states.

In a future study, instead of using separate sinusoids for inspiration and expiration, the development of a single mathematical equation which describes breathing flow, and whose parameters can modify I:E ratio, tidal volume and respiratory rate will be sought. Where this equation is found to have a direct integral, it will be easy to deduce a simple approximate algebraic mathematical formula that predicts work of breathing under NHF conditions given the resistance coefficients. Such a simple formula will be preferred to using the Fourier decomposition of the breathing pattern and solving it numerically.

In the present work, the tracheal pressure and upper airway resistance during mouth close and open breathing were investigated. In the mouth open breathing state, the nasal and oral resistance act as two resistors in parallel configuration. In a future work, it will be insightful to know the relative contribution of the oral resistance to the total.

The present work supports the conclusions of Groves and Tobin (2007); Parke et al. (2009) that the upper airway pressure rises with NHF but it is unclear how this translates to and increase in end-expiratory volume (functional residual capacity) (Gotera et al. (2013)).

The rise in lung impedance in the work of Corley et al. (2011) and Riera et al. (2013) who used the electrical lung impedance tomography was interpreted as a rise in end-expiratory volume. It is however unclear how impedance is related to end-expiratory volume. It will be interesting to know the amount of positive distension pressure in the different generations of the small airways. In this regard, joining a 3-D printed bronchial tree to the trachea of the upper airway model used in this work may be a good starting point. Using the estimated compliance and surface tension of an aveolus, pressure data from such an experiment can be useful in exploring the degree to which NHF prevents alveolar atelectasis. Such an in vitro setup can allow for the measurement of lower airway resistance under NHF conditions.

In tests associated with the measurement of tracheal CO_2, CO_2 was metered via a bleed valve in the piston pump chamber at a constant flow rate. It will be physiologically more accurate to drive CO_2 bleed rate via diffusion such that a rise in piston chamber CO_2 tension will modulate the rate of flow. This can be achieved with a microcontroller-operated solenoid valve. With such a setup, a nonlinear rise in CO_2 may be observed instead of the linear rise in CO_2 tension with apnea duration. Conclusions drawn from Chapters 5 through Chapter 7 may remain same qualitatively but not quantitatively as the end-tidal CO_2 with and without CO_2 are likely to change. As a limitation only 5 waveforms were used to investigate the effect of flow pattern on end-tidal CO_2 tension in chapter 7. The use of more waveforms will be desirable as it will improve the quality of the findings.

In Chapter 8, NHF was modelled by assuming that 3 - 5 % of jet flow reaches the nasopharynx and adds to the expiratory breathing flow. This assumption can be dispensed by including a mathematical model of turbulent diffusion into the system of equations developed for the dead space volume where recirculation current (which promotes turbulent mixing) have been observed (Spence (2011)). In the current model, CO_2 influx into the alveolar space was fixed at a constant rate as was done in the in vitro experiment. To make the model physiologically more accurate a metabolic CO_2 diffusion flux (driven by concentration

gradient), blood transport delays from the heart to the alveoli, and equations describing, biocarbonate chemistry, oxygen binding and dissociation with haemoglobin must be included.

References

RM Agius, J Nee, B McGovern, and A Robertson. Structure activity hypotheses in occupational asthma caused by low molecular weight substances. *Annals of Occupational Hygiene*, 35(2):129–137, 1991. ISSN 0003-4878.

Nadia Aït-Khaled, Donald A. Enarson, Salah Ottmani, Asma El Sony, Mai Eltigani, and Ricardo Sepulveda. Chronic airflow limitation in developing countries: burden and priorities. *International journal of chronic obstructive pulmonary disease*, 2(2):141, 2007.

Christopher J. Allen and Norman L. Jones. Rate of change of alveolar carbon dioxide and the control of ventilation during exercise. *The Journal of physiology*, 355(1):1–9, 1984.

R. Nisha Aurora, Susmita Chowdhuri, Kannan Ramar, Sabin R. Bista, Kenneth R. Casey, Carin I. Lamm, David A. Kristo, Jorge M. Mallea, James A. Rowley, Rochelle S. Zak, and others. The treatment of central sleep apnea syndromes in adults: practice parameters with an evidence-based literature review and meta-analyses. *Sleep*, 35(1):17–40, 2012.

M. Safwan Badr. Central Sleep Apnea. *Primary Care: Clinics in Office Practice*, 32(2): 361–374, 2005. ISSN 0095-4543, 1558-299X. doi: 10.1016/j.pop.2005.02.003.

Neil Bailie, Brendan Hanna, John Watterson, and Geraldine Gallagher. An overview of numerical modelling of nasal airflow. *Rhinology*, 44(1):53, 2006. ISSN 0300-0729.

Peter J. Barnes. New concepts in the pathogenesis of bronchial hyperresponsiveness and asthma. *Journal of allergy and clinical immunology*, 83(6):1013–1026, 1989.

Peter J. Barnes. Pathophysiology of asthma. *Br J Clin Pharmacol*, 42(1):3–10, 1996. ISSN 0306-5251. doi: 10.1046/j.1365-2125.1996.03721.x.

Paul Bégin and Alejandro Grassino. Inspiratory Muscle Dysfunction and Chronic Hypercapnia in Chronic Obstructive Pulmonary Disease. *American Review of Respiratory Disease*, 143(5_pt_1):905–912, 1991. ISSN 0003-0805. doi: 10.1164/ajrccm/143.5_Pt_1.905.

Alona Ben-Tal. Simplified models for gas exchange in the human lungs. *Journal of Theoretical Biology*, 238(2):474–495, 2006.

H. Benallal and T. Busso. Analysis of end-tidal and arterial PCO2 gradients using a breathing model. *European journal of applied physiology*, 83(4-5):402–408, 2000.

Habib Benallal, Christian Denis, Fabrice Prieur, and Thierry Busso. Assessment of arterial gas pressures and cardiac output using a breathing lung model. *Medicine and science in sports and exercise*, 34(11):1750–1756, 2002.

L. Blanch, P. V. Romero, U. Lucangelo, and others. Volumetric capnography in the mechanically ventilated patient. *Minerva anestesiologica*, 72(6):577–586, 2006.

T. Douglas Bradley and John S. Floras. Sleep Apnea and Heart Failure. *Circulation*, 107 (13):1822–1826, 2003. ISSN 0009-7322, 1524-4539. doi: 10.1161/01.CIR.0000061758.05044.64.

Bill B. Brashier and Rahul Kodgule. Risk factors and pathophysiology of chronic obstructive pulmonary disease (COPD). *J Assoc Physicians India*, 60:17–21, 2012.

Jens Bräunlich, Denise Beyer, David Mai, Stefan Hammerschmidt, H. J. Seyfarth, and Hubert Wirtz. Effects of nasal high flow on ventilation in volunteers, COPD and idiopathic pulmonary fibrosis patients. *Respiration*, 85(4):319–325, 2013.

D. Brodovsky, J. A. Macdonell, and R. M. Cherniack. The respiratory response to carbon dioxide in health and in emphysema. *J Clin Invest*, 39(5):724–729, 1960. ISSN 0021-9738.

Buchajczyk. *The effect of compliance in the upper airway*. PhD thesis, University of Canterbury, New Zealand, 2017.

Belen Cabello and Jordi Mancebo. Work of breathing. *Intensive Care Medicine*, 32(9): 1311–1314, 2006. ISSN 0342-4642, 1432-1238. doi: 10.1007/s00134-006-0278-3.

JM Cairo. Administering medical gases: regulators, flowmeters, and controlling devices. *Respiratory Care Equipment, 6th Edition. Mosby's, Inc., New York*, 66, 1999.

P. M. A. Calverley. Respiratory failure in chronic obstructive pulmonary disease. *European Respiratory Journal*, 22(47 suppl):26s–30s, 2003. ISSN 0903-1936, 1399-3003. doi: 10.1183/09031936.03.00030103.

Michelle Cao, Christian Guilleminault, and Chen Lin. Central Sleep Apnea: Effects on Stroke Volume in Heart Failure. *American Journal of Respiratory and Critical Care Medicine*, 187 (4):340–341, 2013. ISSN 1073-449X, 1535-4970. doi: 10.1164/rccm.201212-2250ED.

Wissam Chatila, Tom Nugent, Gwendolyn Vance, John Gaughan, and Gerard J. Criner. The effects of high-flow vs low-flow oxygen on exercise in advanced obstructive airways disease. *CHEST Journal*, 126(4):1108–1115, 2004.

Neil S Cherniack and Guy S Longobardo. Cheyne-Stokes breathing: an instability in physiologic control. *Survey of Anesthesiology*, 18(2):109–111, 1974. ISSN 0039-6206.

Arthur B. Chilton and Ralph W. Stacy. A mathematical analysis of carbon dioxide respiration in man. *The bulletin of mathematical biophysics*, 14(1):1–18, 1952.

F. Chung, N. Barnes, M. Allen, R. Angus, P. Corris, A. Knox, J. Miles, A. Morice, J. O'Reilly, and M. Richardson. Assessing the burden of respiratory disease in the UK. *Respiratory medicine*, 96(12):963–975, 2002.

SW Clarke, JG Jones, and DR Oliver. Resistance to two-phase gas-liquid flow in airways. *Journal of applied physiology*, 29(4):464–471, 1970. ISSN 8750-7587.

Ric L. Colasanti, M. Jocelyn Morris, Richard G. Madgwick, Linda Sutton, and E. Mark Williams. ANalysis of tidal breathing profiles in cystic fibrosis and copd*. *Chest*, 125(3): 901–908, 2004. ISSN 0012-3692. doi: 10.1378/chest.125.3.901.

PW Collett, C Perry, and LA Engel. Pressure-time product, flow, and oxygen cost of resistive breathing in humans. *Journal of Applied Physiology*, 58(4):1263–1272, 1985. ISSN 8750-7587.

Guilhem J. Collier, Helen Marshall, Madhwesha Rao, Neil J. Stewart, David Capener, and Jim M. Wild. Observation of cardiogenic flow oscillations in healthy subjects with hyperpolarized 3he MRI. *Journal of Applied Physiology*, 119(9):1007–1014, November 2015. ISSN 8750-7587. doi: 10.1152/japplphysiol.01068.2014.

C. D. Cook, J. M. Sutherland, S. Segal, R. B. Cherry, J. Mead, M. B. McIlroy, and C. A. Smith. Studies of Respiratory Physiology in the Newborn Infant. III. Measurements of Mechanics of Respiration1. *Journal of Clinical Investigation*, 36(3):440–448, 1957. ISSN 0021-9738.

A. Corley, L. R. Caruana, A. G. Barnett, O. Tronstad, and J. F. Fraser. Oxygen delivery through high-flow nasal cannulae increase end-expiratory lung volume and reduce respiratory rate in post-cardiac surgical patients. *British Journal of Anaesthesia*, 107(6): 998–1004, 2011. ISSN 0007-0912, 1471-6771. doi: 10.1093/bja/aer265.

Maria Rosa Costanzo, Rami Khayat, Piotr Ponikowski, Ralph Augostini, Christoph Stellbrink, Marcus Mianulli, and William T. Abraham. Mechanisms and Clinical Consequences of Untreated Central Sleep Apnea in Heart Failure. *Journal of the American College of Cardiology*, 65(1):72–84, 2015. ISSN 0735-1097. doi: 10.1016/j.jacc.2014.10.025.

J. G. Defares, H. E. Derksen, and J. W. Duyff. Cerebral blood flow in the regulation of respiration.(Studies in the regulation of respiration. I. *Acta physiologica et pharmacologica Neerlandica*, 9:327–360, 1960.

R. L. Dellaca, P. Santus, A. Aliverti, N. Stevenson, S. Centanni, P. T. Macklem, A. Pedotti, and P. M. A. Calverley. Detection of expiratory flow limitation in COPD using the forced oscillation technique. *European Respiratory Journal*, 23(2):232–240, 2004.

R. L. Dellacà, P. P. Pompilio, P. P. Walker, N. Duffy, A. Pedotti, and P. M. A. Calverley. Effect of bronchodilation on expiratory flow limitation and resting lung mechanics in COPD. *European Respiratory Journal*, 33(6):1329–1337, 2009. ISSN 0903-1936, 1399-3003. doi: 10.1183/09031936.00139608.

Jerome A Dempsey. Crossing the apnoeic threshold: causes and consequences. *Experimental physiology*, 90(1):13–24, 2005. ISSN 1469-445X.

Naresh A Dewan and C William Bell. Effect of low flow and high flow oxygen delivery on exercise tolerance and sensation of dyspnea: a study comparing the transtracheal catheter and nasal prongs. *Chest*, 105(4):1061–1065, 1994. ISSN 0012-3692.

Karla Maree Dey. Anatomic Dead Space Washout and Flow Effects during Breathing with Nasal High Flow Therapy. 2014.

S. Diab, K. Dunster, A. Spooner, A. Corley, and J. Fraser. Nasal high flow oxygen therapy reduced respiratory rate, tissue CO2 and increased tidal volumes in COPD patients. *Australian Critical Care*, 28(1):41, 2015. ISSN 1036-7314, 1036-7314. doi: 10.1016/j.aucc.2014.10.012.

DJ Doorly, DJ Taylor, and RC Schroter. Mechanics of airflow in the human nasal airways. *Respiratory physiology & neurobiology*, 163(1):100–110, 2008. ISSN 1569-9048.

Philip J. Dorman, W. James Sullivan, and Robert F. Pitts. The renal response to acute respiratory acidosis. *Journal of Clinical Investigation*, 33(1):82, 1954.

Arthur B. DuBois, Stella Y. Botelho, and Julius H. Comroe. A new method for measuring airway resistance in man using a body plethysmograph: Values in normal subjects and in patients with respiratory disease 1. *J Clin Invest*, 35(3):327–335, 1956. ISSN 0021-9738.

K. Dysart, T. L. Miller, M. R. Wolfson, and T. H. Shaffer. Research in high flow therapy: mechanisms of action. *Respir Med*, 103(10):1400–5, 2009. ISSN 1532-3064 (Electronic) 0954-6111 (Linking). doi: 10.1016/j.rmed.2009.04.007.

D Elad, R Liebenthal, BL Wenig, and S Einav. Analysis of air flow patterns in the human nose. *Medical and Biological Engineering and Computing*, 31(6):585–592, 1993. ISSN 0140-0118.

Jakub Elcner, Frantisek Lizal, Jan Jedelsky, Miroslav Jicha, and Michaela Chovancova. Numerical investigation of inspiratory airflow in a realistic model of the human tracheobronchial airways and a comparison with experimental results. *Biomechanics and modeling in mechanobiology*, 15(2):447–469, 2016. ISSN 1617-7959.

Andres Esteban, Antonio Anzueto, Inmaculada Alia, Federico Gordo, Carlos Apezteguia, Fernando Palizas, David Cide, Rosanne Goldwaser, Luis Soto, and Guillermo Bugedo. How is mechanical ventilation employed in the intensive care unit? An international utilization review. *American Journal of Respiratory and Critical Care Medicine*, 161(5): 1450–1458, 2000. ISSN 1535-4970.

Gabriela P Ferreyra, Iacopo Baussano, Vincenzo Squadrone, Lorenzo Richiardi, Giovana Marchiaro, Lorenzo Del Sorbo, Luciana Mascia, Franco Merletti, and V Marco Ranieri. Continuous positive airway pressure for treatment of respiratory complications after abdominal surgery: a systematic review and meta-analysis. *Annals of surgery*, 247(4): 617–626, 2008. ISSN 0003-4932.

B. G. Ferris, L. Opie, and J. Mead. Partitioning of respiratory resistance in man. volume 19, pages 377–377. FEDERATION AMER SOC EXP BIOL 9650 ROCKVILLE PIKE, BETHESDA, MD 20814-3998, 1960.

W. F. Fincham and F. T. Tehrani. A mathematical model of the human respiratory system. *Journal of biomedical engineering*, 5(2):125–133, 1983.

B. Fleury, D. Murciano, C. Talamo, M. Aubier, R. Pariente, and J. Milic-Emili. Work of Breathing in Patients with Chronic Obstructive Pulmonary Disease in Acute Respiratory Failure 1–3. *American Review of Respiratory Disease*, 131(6):822–827, 1985.

John F Fraser, Amy J Spooner, Kimble R Dunster, Chris M Anstey, and Amanda Corley. Nasal high flow oxygen therapy in patients with COPD reduces respiratory rate and tissue carbon dioxide while increasing tidal and end-expiratory lung volumes: a randomised crossover trial. *Thorax*, 71(8):759–761, 2016. ISSN 1468-3296.

Urs Frey, Michael Silverman, and Bela Suki. Analysis of the harmonic content of the tidal flow waveforms in infants. *Journal of Applied Physiology*, 91(4):1687–1693, 2001. ISSN 8750-7587, 1522-1601.

Meg Frizzola, Thomas L. Miller, Maria Elena Rodriguez, Yan Zhu, Jorge Rojas, Anne Hesek, Angela Stump, Thomas H. Shaffer, and Kevin Dysart. High-flow nasal cannula: Impact on oxygenation and ventilation in an acute lung injury model. *Pediatric pulmonology*, 46 (1):67–74, 2011.

W. Galetke, C. Feier, T. Muth, K. H. Ruehle, E. Borsch-Galetke, and W. Randerath. Reference values for dynamic and static pulmonary compliance in men. *Respiratory Medicine*, 101 (8):1783–1789, 2007. ISSN 0954-6111. doi: 10.1016/j.rmed.2007.02.015.

I. Galvin, G. B. Drummond, and M. Nirmalan. Distribution of blood flow and ventilation in the lung: gravity is not the only factor. *British Journal of Anaesthesia*, 98(4):420–428, 2007. ISSN 0007-0912, 1471-6771. doi: 10.1093/bja/aem036.

P. H. Geoghegan, N. A. Buchmann, C. J. T. Spence, Steve Moore, and Mark Jermy. Fabrication of rigid and flexible refractive-index-matched flow phantoms for flow visualisation and optical flow measurements. *Experiments in fluids*, 52(5):1331–1347, 2012.

Patrick Henry Geoghegan. *In vitro experimental investigation into the effect of compliance on models of arterial hemodynamics: a thesis presented for the degree of Doctor of Philosophy in Mechanical Engineering at the University of Canterbury, Christchurch, New Zealand*. 2012.

Janneke Gisolf, Ronald Wilders, Rogier V. Immink, Johannes J. Van Lieshout, and John M. Karemaker. Tidal volume, cardiac output and functional residual capacity determine end-tidal CO2 transient during standing up in humans. *The Journal of Physiology*, 554(2): 579–590, 2004. ISSN 1469-7793. doi: 10.1113/jphysiol.2003.056895.

Tajana Jalušic Gluncic, Latinka Basara, Ljiljana Konecki, Slavica Tomic, Miroslav Samarzija, and Marko Jakopovic. Capnographic measurement as a screening method for respiratory obstructive diseases. *European Respiratory Journal*, 46(suppl 59):PA1039, 2015. ISSN 0903-1936, 1399-3003. doi: 10.1183/13993003.congress-2015.PA1039.

M. Gorini, G. Misuri, A. Corrado, R. Duranti, I. Iandelli, E. De Paola, and G. Scano. Breathing pattern and carbon dioxide retention in severe chronic obstructive pulmonary disease. *Thorax*, 51(7):677–683, July 1996. ISSN , 1468-3296. doi: 10.1136/thx.51.7.677.

C. Gotera, S. Díaz Lobato, T. Pinto, and J. C. Winck. Clinical evidence on high flow oxygen therapy and active humidification in adults. *Revista Portuguesa de Pneumologia*, 19(5): 217–227, 2013. ISSN 0873-2159. doi: 10.1016/j.rppneu.2013.03.005.

Alan S. Graham, Girish Chandrashekharaiah, Agop Citak, Randall C. Wetzel, and Christopher J. L. Newth. Positive end-expiratory pressure and pressure support in peripheral airways obstruction. *Intensive Care Medicine*, 33(1):120–127, 2006. ISSN 0342-4642, 1432-1238. doi: 10.1007/s00134-006-0445-6.

John S Gray. Pulmonary ventilation and its physiological regulation. *Southern Medical Journal*, 44(11):1086, 1951. ISSN 0038-4348.

Fred S Grodins, June Buell, and Alex J Bart. Mathematical analysis and digital simulation of the respiratory control system. Report, DTIC Document, 1967.

Nicole Groves and Antony Tobin. High flow nasal oxygen generates positive airway pressure in adult volunteers. *Australian Critical Care*, 20(4):126–131, 2007. ISSN 1036-7314. doi: 10.1016/j.aucc.2007.08.001.

Anthony J. Guarascio, Shauntá M. Ray, Christopher K. Finch, and Timothy H. Self. The clinical and economic burden of chronic obstructive pulmonary disease in the USA. *ClinicoEconomics and Outcomes Research: CEOR*, 5:235–245, 2013. ISSN 1178-6981. doi: 10.2147/CEOR.S34321.

Intaek Hahn, PETER W Scherer, and Maxwell M Mozell. Velocity profiles measured for airflow through a large-scale model of the human nasal cavity. *Journal of Applied Physiology*, 75(5):2273–2287, 1993. ISSN 8750-7587.

Adam B Hernandez and Susheel P Patil. Pathophysiology of central sleep apneas. *Sleep and Breathing*, 20(2):467–482, 2016. ISSN 1520-9512.

Dean Hess. *Respiratory care: principles and practice*. Jones & Bartlett Learning, 2011. ISBN 0-7637-6003-X.

Faiq G. Issa and Colin E. Sullivan. Reversal of central sleep apnea using nasal CPAP. *Chest*, 90(2):165–171, 1986.

Sorli J, Grassino A, Lorange G, and Milic-Emili J. Control of breathing in patients with chronic obstructive lung disease. *Clinical science and molecular medicine*, 54(3):295–304, 1978. ISSN 0301-0538. doi: 10.1042/cs0540295.

Michael B. Jaffe. Volumetric Capnography, The Next Advance in CO2 Monitoring. *Respironics Inc (Critical Care)*, 2006.

S. Javaheri. Central Sleep Apnea. *Clinics in Chest Medicine*, 31(2):235–248, 2010. ISSN 0272-5231. doi: 10.1016/j.ccm.2010.02.013.

Shahrokh Javaheri. A mechanism of central sleep apnea in patients with heart failure. *New England Journal of Medicine*, 341(13):949–954, 1999.

Shahrokh Javaheri, Jason Smith, and Eugene Chung. The Prevalence and Natural History of Complex Sleep Apnea. *Journal of Clinical Sleep Medicine : JCSM : Official Publication of the American Academy of Sleep Medicine*, 5(3):205–211, 2009. ISSN 1550-9389.

J. Johansson, T. Curstedt, and B. Robertson. The proteins of the surfactant system. *European Respiratory Journal*, 7(2):372–391, 1994.

Gustavo Juan, Peter Calverley, Carlos Talamo, Jeff Schnader, and Charis Roussos. Effect of carbon dioxide on diaphragmatic function in human beings. *New England Journal of Medicine*, 310(14):874–879, 1984.

Jodie Kernick and Judy Magarey. What is the evidence for the use of high flow nasal cannula oxygen in adult patients admitted to critical care units? A systematic review. *Australian Critical Care*, 23(2):53–70, 2010. ISSN 10367314. doi: 10.1016/j.aucc.2010.01.001.

KPWMM Keyhani, PW Scherer, and MM Mozell. Numerical simulation of airflow in the human nasal cavity. *TRANSACTIONS-AMERICAN SOCIETY OF MECHANICAL ENGINEERS JOURNAL OF BIOMECHANICAL ENGINEERING*, 117:429–441, 1995. ISSN 0148-0731.

MCK Khoo, Richard E Kronauer, Kingman P Strohl, and Arthur S Slutsky. Factors inducing periodic breathing in humans: a general model. *Journal of Applied Physiology*, 53(3): 644–659, 1982. ISSN 8750-7587.

Baruch Krauss and Dean R. Hess. Capnography for Procedural Sedation and Analgesia in the Emergency Department. *Annals of Emergency Medicine*, 50(2):172–181, 2007. ISSN 0196-0644. doi: 10.1016/j.annemergmed.2006.10.016.

Z. J. Kubicka, J. Limauro, and R. A. Darnall. Heated, Humidified High-Flow Nasal Cannula Therapy: Yet Another Way to Deliver Continuous Positive Airway Pressure? *PEDIATRICS*, 121(1):82–88, 2008. ISSN 0031-4005, 1098-4275. doi: 10.1542/peds.2007-0957.

Haribalan Kumar, Callum J. T. Spence, and Merryn H. Tawhai. Modeling of pharyngeal pressure during adult nasal high flow therapy. *Respiratory Physiology & Neurobiology*, 2015. ISSN 1569-9048. doi: 10.1016/j.resp.2015.06.011.

Alan W Langer, J Hutchenson, John D Charlton, James A McCubbin, Paul A Orist, and Catherine M Stoney. On-Line Minicomputerized Measurement of Cardiopulmonary Function On a Breath-By-Breath Basis. *Psychophysiology*, 22(1):50–57, 1985. ISSN 1469-8986.

Pisani Lara, Corcione Nadia, Comellini Vittoria, Natali Filippo, Fasano Luca, and Nava Stefano. Short Term Physiological Effects of Nasal High Flow (NHF) on Respiratory Mechanics in Stable Patients with Chronic Obstructive Pulmonary Disease (COPD). In *C51. Respiratory Failure: High Flow Oxygen, Liberation, Non-invasive, And Prolonged Ventilation*, American Thoracic Society International Conference Abstracts, pages A5318–A5318. American Thoracic Society, 2016.

Joseph K Leader, Robert M Rogers, Carl R Fuhrman, Frank C Sciurba, Bin Zheng, Paul F Thompson, Joel L Weissfeld, Sara K Golla, and David Gur. Size and morphology of the trachea before and after lung volume reduction surgery. *American Journal of Roentgenology*, 183(2):315–321, 2004. ISSN 0361-803X.

Chih Fang Lee, Mohd Zulkifly Abdullah, Kamarul Arifin Ahmad, and Ibrahim Lutfi Shuaib. Standardization of Malaysian adult female nasal cavity. *Computational and mathematical methods in medicine*, 2013, 2013a. ISSN 1748-670X.

Jan Hau Lee, Kyle J. Rehder, Lee Williford, Ira M. Cheifetz, and David A. Turner. Use of high flow nasal cannula in critically ill infants, children, and adults: a critical review of the literature. *Intensive care medicine*, 39(2):247–257, 2013b.

Robert L. Levine, Marvin A. Wayne, and Charles C. Miller. End-tidal carbon dioxide and outcome of out-of-hospital cardiac arrest. *New England Journal of Medicine*, 337(5): 301–306, 1997.

Robert G. Locke, Marla R. Wolfson, Thomas H. Shaffer, S. David Rubenstein, and Jay S. Greenspan. Inadvertent administration of positive end-distending pressure during nasal cannula flow. *Pediatrics*, 91(1):135–138, 1993.

Loveridge. Breathing pattern in patients with chronic obstructive pulmonary disease. 130(5), 1984.

Salvatore Maurizio Maggiore, Francesco Antonio Idone, Rosanna Vaschetto, Rossano Festa, Andrea Cataldo, Federica Antonicelli, Luca Montini, Andrea De Gaetano, Paolo Navalesi, and Massimo Antonelli. Nasal high-flow versus Venturi mask oxygen therapy after extubation. Effects on oxygenation, comfort, and clinical outcome. *American journal of respiratory and critical care medicine*, 190(3):282–288, 2014. ISSN 1073-449X.

Brett J. Manley, Louise S. Owen, Lex W. Doyle, Chad C. Andersen, David W. Cartwright, Margo A. Pritchard, Susan M. Donath, and Peter G. Davis. High-Flow Nasal Cannulae in Very Preterm Infants after Extubation. *New England Journal of Medicine*, 369(15): 1425–1433, 2013. ISSN 0028-4793. doi: 10.1056/NEJMoa1300071.

Ted B Martonen, Liang Quan, Zongqin Zhang, and CJ Musante. Flow simulation in the human upper respiratory tract. *Cell biochemistry and biophysics*, 37(1):27, 2002. ISSN 1085-9195.

Brian McGinley, Ann Halbower, Alan R. Schwartz, Philip L. Smith, Susheel P. Patil, and Hartmut Schneider. Effect of a high-flow open nasal cannula system on obstructive sleep apnea in children. *Pediatrics*, 124(1):179–188, 2009.

Brian M. McGinley, Susheel P. Patil, Jason P. Kirkness, Philip L. Smith, Alan R. Schwartz, and Hartmut Schneider. A nasal cannula can be used to treat obstructive sleep apnea. *American journal of respiratory and critical care medicine*, 176(2):194–200, 2007.

J Mead. Contribution of compliance of airways to frequency-dependent behavior of lungs. *Journal of Applied Physiology*, 26(5):670–673, 1969. ISSN 8750-7587.

Andrea Kutinova Menclova and Rachel Susan Webb. The effects of home heating on asthma: evidence from New Zealand. *New Zealand Economic Papers*, 50(2):193–211, 2016. ISSN 0077-9954.

Florian R Menter. Two-equation eddy-viscosity turbulence models for engineering applications. *AIAA journal*, 32(8):1598–1605, 1994. ISSN 0001-1452.

Ernst Meyer. Simultaneous correction for tracer arrival delay and dispersion in CBF measurements by the H215o autoradiographic method and dynamic PET. *J Nucl Med*, 30(6): 1069–1078, 1989.

Martijn Miedema, Pauline S van der Burg, Sabine Beuger, Frans H de Jongh, Inez Frerichs, and Anton H van Kaam. Effect of nasal continuous and biphasic positive airway pressure on lung volume in preterm infants. *The Journal of pediatrics*, 162(4):691–697, 2013. ISSN 0022-3476.

Rebecca J Mieloszyk, George C Verghese, Kenneth Deitch, Brendan Cooney, Abdullah Khalid, Milciades A Mirre-Gonzalez, Thomas Heldt, and Baruch S Krauss. Automated Quantitative Analysis of Capnogram Shape for COPD–Normal and COPD–CHF Classification. *IEEE Transactions on Biomedical Engineering*, 61(12):2882–2890, 2014. ISSN 0018-9294.

Howard T. Milhorn, Richard Benton, Richard Ross, and Arthur C. Guyton. A mathematical model of the human respiratory control system. *Biophysical Journal*, 5(1):27–46, 1965.

J. Milic-Emili, E. Rocca, and E. D'Angelo. Work of breathing. In J. Milic-Emili Md, U. Lucangelo Md, A. Pesenti Md, and W. A. Zin Md, editors, *Basics of Respiratory Mechanics and Artificial Ventilation*, Topics in Anaesthesia and Critical Care, pages 165–175. Springer Milan, 1999. ISBN 978-88-470-0046-9 978-88-470-2273-7.

Winfried Möller, Gülnaz Celik, Sheng Feng, Peter Bartenstein, Gabriele Meyer, Oliver Eickelberg, Otmar Schmid, and Stanislav Tatkov. Nasal high flow clears anatomical dead space in upper airway models. *Journal of Applied Physiology*, 118(12):1525–1532, 2015. ISSN 8750-7587, 1522-1601. doi: 10.1152/japplphysiol.00934.2014.

M. J. Morris and D. J. Lane. Tidal expiratory flow patterns in airflow obstruction. *Thorax*, 36(2):135–142, 1981.

Yukiko Motojima, Masato Ito, Shuntaro Oka, Atsushi Uchiyama, Masanori Tamura, and Fumihiko Namba. Use of high-flow nasal cannula in neonates: Nationwide survey in Japan. *Pediatrics International*, 58(4):308–310, 2016. ISSN 1442-200X. doi: 10.1111/ped.12903.

Toby Mündel, Sheng Feng, Stanislav Tatkov, and Hartmut Schneider. Mechanisms of nasal high flow on ventilation during wakefulness and sleep. *Journal of Applied Physiology*, 114(8):1058–1065, 2013. ISSN 8750-7587, 1522-1601. doi: 10.1152/japplphysiol.01308.2012.

Christian Mundt, Alexander Sventitskiy, Jeffrey E Cehelsky, Andrea B Patters, Markus Tservistas, Michael C Hahn, Gerd Juhl, and John P DeVincenzo. Assessing Modeled C O 2 Retention and Rebreathing of a Facemask Designed for Efficient Delivery of Aerosols to Infants. *ISRN pediatrics*, 2012, 2012.

Joshua Nagler and Baruch Krauss. Capnographic Monitoring in Respiratory Emergencies. *Clinical Pediatric Emergency Medicine*, 10(2):82–89, 2009. ISSN 1522-8401. doi: 10.1016/j.cpem.2009.03.004.

Asthma Education National and Program Prevention. Expert Panel Report 3 (EPR-3): Guidelines for the Diagnosis and Management of Asthma-Summary Report 2007. *The Journal of allergy and clinical immunology*, 120(5 Suppl):S94, 2007. ISSN 1097-6825.

Masaji Nishimura. High-flow nasal cannula oxygen therapy in adults. *Journal of intensive care*, 3(1):15, 2015.

Shalini Ojha, Eleanor Gridley, and Jon Dorling. Use of heated humidified high-flow nasal cannula oxygen in neonates: a UK wide survey. *Acta Paediatrica*, 102(3):249–253, 2013.

Arthur B. Otis, Wallace O. Fenn, and Hermann Rahn. Mechanics of breathing in man. *Journal of applied physiology*, 2(11):592–607, 1950.

Samet Ozlugedik, Gunes Nakiboglu, Cuneyt Sert, Alaittin Elhan, Ergin Tonuk, Serdar Akyar, and Ibrahim Tekdemir. Numerical study of the aerodynamic effects of septoplasty and partial lateral turbinectomy. *The Laryngoscope*, 118(2):330–334, 2008. ISSN 1531-4995.

Paresh B. Pandit, Sherry E. Courtney, Kee H. Pyon, Judy G. Saslow, and Robert H. Habib. Work of breathing during constant-and variable-flow nasal continuous positive airway pressure in preterm neonates. *Pediatrics*, 108(3):682–685, 2001.

R. Parke, S. McGuinness, and M. Eccleston. Nasal high-flow therapy delivers low level positive airway pressure. *British Journal of Anaesthesia*, 103(6):886–890, 2009. ISSN 0007-0912, 1471-6771. doi: 10.1093/bja/aep280.

Rachael L. Parke, Michelle L. Eccleston, and Shay P. McGuinness. The effects of flow on airway pressure during nasal high-flow oxygen therapy. *Respiratory care*, 56(8): 1151–1155, 2011.

S. Parot, C. Saunier, H. Gautier, J. Milic-Emili, and P. Sadoul. Breathing pattern and hypercapnia in patients with obstructive pulmonary disease. *The American review of respiratory disease*, 121(6):985–991, 1980.

A. Patel and S. A. R. Nouraei. Transnasal Humidified Rapid-Insufflation Ventilatory Exchange (THRIVE): a physiological method of increasing apnoea time in patients with difficult airways. *Anaesthesia*, 70(3):323–329, 2015.

Amit V. Patel, Dennis Hwang, Maria J. Masdeu, Guo-Ming Chen, David M. Rapoport, and Indu Ayappa. Predictors of response to a nasal expiratory resistor device and its potential mechanisms of action for treatment of obstructive sleep apnea. *Journal of clinical sleep medicine: JCSM: official publication of the American Academy of Sleep Medicine*, 7(1): 13, 2011.

Neil Pearce and Michael J. Hensley. Epidemiologic studies of beta agonists and asthma deaths. *Epidemiologic reviews*, 20(2):173–186, 1998.

Trang M. T. Pham, Lee O'Malley, Sara Mayfield, Simon Martin, and Andreas Schibler. The effect of high flow nasal cannula therapy on the work of breathing in infants with bronchiolitis. *Pediatric pulmonology*, 2014.

Jahan Porhomayon, Ali A. El-Solh, Leili Pourafkari, Philippe Jaoude, and Nader D. Nader. Applications of Nasal High-Flow Oxygen Therapy in Critically ill Adult Patients. *Lung*, pages 1–10, 2016. ISSN 0341-2040, 1432-1750. doi: 10.1007/s00408-016-9885-0.

Harold Rea, Sue McAuley, Lata Jayaram, Jeffrey Garrett, Hans Hockey, Louanne Storey, Glenis O'Donnell, Lynne Haru, Matthew Payton, and Kevin O'Donnell. The clinical utility of long-term humidification therapy in chronic airway disease. *Respiratory medicine*, 104 (4):525–533, 2010.

Peter Reischl and Christine B. Beaucage. Time constant and transport delay determination of the gas analyzer. *Mathematical Modelling*, 7(9):1613–1620, 1986. ISSN 0270-0255. doi: 10.1016/0270-0255(86)90093-X.

Jordi Riera, Purificación Pérez, Jordi Cortés, Oriol Roca, Joan Ramon Masclans, and Jordi Rello. Effect of high-flow nasal cannula and body position on end-expiratory lung volume: a cohort study using electrical impedance tomography. *Respiratory care*, 58(4):589–596, 2013.

Peter C Rimensberger. *Pediatric and neonatal mechanical ventilation*. Springer, 2015.

JE Ritchie, AB Williams, C Gerard, and H Hockey. Evaluation of a humidified nasal high-flow oxygen system, using oxygraphy, capnography and measurement of upper airway pressures. *Anaesthesia and intensive care*, 39(6):1103, 2011. ISSN 0310-057X.

Oriol Roca, Jordi Riera, Ferran Torres, and Joan R. Masclans. High-flow oxygen therapy in acute respiratory failure. *Respiratory Care*, 55(4):408–413, 2010.

Philip Rouadi, Fuad M. Baroody, David Abbott, Edward Naureckas, Julian Solway, and Robert M. Naclerio. A technique to measure the ability of the human nose to warm and humidify air. *Journal of Applied Physiology*, 87(1):400–406, 1999.

Sarah Rubin, Anoopindar Ghuman, Timothy Deakers, Robinder Khemani, Patrick Ross, and Christopher J. Newth. Effort of breathing in children receiving high-flow nasal cannula. *Pediatric Critical Care Medicine*, 15(1):1–6, 2014.

J. G. Saslow, Z. H. Aghai, T. A. Nakhla, J. J. Hart, R. Lawrysh, G. E. Stahl, and K. H. Pyon. Work of breathing using high-flow nasal cannula in preterm infants. *Journal of Perinatology*, 26(8):476–480, 2006.

Hartmut Schneider, Karl Heinz Ruehle, K. j Franke, Ulrike Domanski, and Georg Nilius. Nasal High Flow Reduces Hypercapnia By Clearance Of Anatomical Dead Space In A COPD Patient. In *D104. CASE REPORTS: OTHER*, American Thoracic Society International Conference Abstracts, pages A5858–A5858. American Thoracic Society, 2013.

J. T. Sharp, J. P. Henry, S. K. Sweany, W. R. Meadows, and R. J. Pietras. The total work of breathing in normal and obese men. *Journal of Clinical Investigation*, 43(4):728, 1964.

C. J. T. Spence. *Experimental investigations of airflow in the human upper airways during natural and assisted breathing*. Thesis, 2011.

C. J. T. Spence, N. A. Buchmann, M. C. Jermy, and S. M. Moore. Stereoscopic PIV measurements of flow in the nasal cavity with high flow therapy. *Experiments in fluids*, 50 (4):1005–1017, 2011.

C. J. T. Spence, N. A. Buchmann, and M. C. Jermy. Unsteady flow in the nasal cavity with high flow therapy measured by stereoscopic PIV. *Experiments in Fluids*, 52(3):569–579, 2012. ISSN 0723-4864, 1432-1114. doi: 10.1007/s00348-011-1044-z.

M. Christine Stock, John Q. Schisler, and Thomas D. McSweeney. The PaCO2 rate of rise in anesthetized patients with airway obstruction. *Journal of clinical anesthesia*, 1(5): 328–332, 1989.

J. Stocks and S. Godfrey. Nasal resistance during infancy. *Respiration physiology*, 34(2): 233–246, 1978.

George D. Swanson and Duane L. Sherrill. A model evaluation of estimates of breath-to-breath alveolar gas exchange. *Journal of Applied Physiology*, 55(6):1936–1941, 1983.

Benjamin Sztrymf, Jonathan Messika, Fabrice Bertrand, Dominique Hurel, Rusel Leon, Didier Dreyfuss, and Jean-Damien Ricard. Beneficial effects of humidified high flow nasal oxygen in critical care patients: a prospective pilot study. *Intensive care medicine*, 37(11): 1780–1786, 2011.

Arjan B te Pas, Connie Wong, C Omar F Kamlin, Jennifer A Dawson, Colin J Morley, and Peter G Davis. Breathing patterns in preterm and term infants immediately after birth. *Pediatric Research*, 65(3):352–356, 2009. ISSN 0031-3998.

Brian Tiep and Mary Barnett. High flow nasal vs high flow mask oxygen delivery: tracheal gas concentrations through a head extension airway model. *Respir Care*, 47(9):1079, 2002. ISSN 0020-1324.

Martin Tobin, T. S. Chadha, G. Jenouri, S. J. Birch, H. B. Gazeroglu, and M. A. Sackner. Breathing patterns. 1. Normal subjects. *Chest Journal*, 84(2):202–205, 1983.

Martin Tobin, K. Yang, and D. Upson. Breathing pattern in asthma. *CHEST Journal*, 95(1): 1–2, 1989.

Tocris. Respiratory Disease Research, 2017.

Akira Tsuda, Frank S Henry, and James P Butler. Gas and aerosol mixing in the acinus. *Respiratory physiology & neurobiology*, 163(1):139–149, 2008. ISSN 1569-9048.

Justin M Tuggey, Monica Delmastro, and Mark W Elliott. The effect of mouth leak and humidification during nasal non-invasive ventilation. *Respiratory medicine*, 101(9):1874–1879, 2007. ISSN 0954-6111.

S. C. Van Hove, J. Storey, C. Adams, K. Dey, P. H. Geoghegan, N. Kabaliuk, S. D. Oldfield, C. J. T. Spence, M. C. Jermy, V. Suresh, and others. An Experimental and Numerical Investigation of CO2 Distribution in the Upper Airways During Nasal High Flow Therapy. *Annals of biomedical engineering*, pages 1–13, 2016.

A. F. M. Verbraak, J. M. Bogaard, J. E. W. Beneken, Ewout Hoorn, and A. Versprille. Serial lung model for simulation and parameter estimation in body plethysmography. *Medical and Biological Engineering and Computing*, 29(3):309–317, 1991.

Jeffrey J. Ward. High-flow oxygen administration by nasal cannula for adult and perinatal patients. *Respiratory care*, 58(1):98–122, 2013.

Jonathan B. Waugh and Wesley M. Granger. An evaluation of 2 new devices for nasal high-flow gas therapy. *Respiratory care*, 49(8):902–906, 2004.

Ivo Weinhold and Gunter Mlynski. Numerical simulation of airflow in the human nose. *European Archives of Oto-Rhino-Laryngology and Head & Neck*, 261(8):452–455, 2004. ISSN 0937-4477.

Jian Wen, Kiao Inthavong, Jiyuan Tu, and Simin Wang. Numerical simulations for detailed airflow dynamics in a human nasal cavity. *Respiratory physiology & neurobiology*, 161(2): 125–135, 2008. ISSN 1569-9048.

John Burnard West. *Respiratory physiology: the essentials*. Lippincott Williams & Wilkins, 2012.

David P. White. Pathogenesis of Obstructive and Central Sleep Apnea. *American Journal of Respiratory and Critical Care Medicine*, 172(11):1363–1370, 2005. ISSN 1073-449X, 1535-4970. doi: 10.1164/rccm.200412-1631SO.

DJ Wilkinson, CC Andersen, K Smith, and J Holberton. Pharyngeal pressure with high-flow nasal cannulae in premature infants. *Journal of Perinatology*, 28(1):42–47, 2008. ISSN 0743-8346.

E. M. Williams, T. Powell, M. Eriksen, P. Neill, and R. Colasanti. A pilot study quantifying the shape of tidal breathing waveforms using centroids in health and COPD. *Journal of Clinical Monitoring and Computing*, 28(1):67–74, 2013. ISSN 1387-1307, 1573-2614. doi: 10.1007/s10877-013-9497-7.

Brigham C. Willis, Alan S. Graham, Eunice Yoon, Randall C. Wetzel, and Christopher J. L. Newth. Pressure-rate products and phase angles in children on minimal support ventilation and after extubation. *Intensive Care Medicine*, 31(12):1700–1705, 2005. ISSN 0342-4642, 1432-1238. doi: 10.1007/s00134-005-2821-z.

B. You, R. Peslin, C. Duvivier, V. Dang Vu, and J. P. Grilliat. Expiratory capnography in asthma: evaluation of various shape indices. *European Respiratory Journal*, 7(2):318–323, 1994.

J Zheng, YP Wang, Z Dong, ZQ Yang, and W Sun. Nasal cavity volume and nasopharyngeal cavity volume in adults measured by acoustic rhinometry. *Lin chuang er bi yan hou ke za zhi= Journal of clinical otorhinolaryngology*, 14(11):494–495, 2000.

Mohammed Zubair, Vizy Nazira Riazuddin, Mohammed Zulkifly Abdullah, Rushdan Ismail, Ibrahim Lutfi Shuaib, Suzina Abdul Hamid, and Kamarul Arifin Ahmad. Airflow inside the nasal cavity: visualization using computational fluid dynamics. 2010.

Appendix A

A.1 Deconvolution algorithm

```
function deconv_coo= deconvolution_algorithm(coo_data)

CO_2data = coo_data(:,2);       %load CO2 data

data_time  = coo_data(:,1);     %load time data

data_length= length(CO_2data);  %define number of data points

tc = 190/1000;                  %Define time constants

non_dispersed_laplace  = CO_2data(2:data_length) + (diff(CO_2data)./diff(data_time)

non_dispersed_laplace  = cat(1,CO_2data(1),non_dispersed_laplace); %Put time and CO

deconv_coo = cat(2,data_time,non_dispersed_laplace) ;              % Deconvoluted s
end
```

A.2 Python script for mathematical model

```
# -*- coding: utf-8 -*-
"""
Created on Sun Jul 30 22:14:50 2017
"""

import matplotlib.pyplot as plt
from scipy.integrate import odeint
import numpy as np

#Function in which Equations of models are defined
def odefn(x,t,PL,dPLdt,Pm,t1,N,E,frc,R,pw,k1_i,k2_i,k1_e,k2_e):

    ,,,
    list of parameters and variables
    ================================
    PL = pleural pressure
    dPLdt = derivative of pleural pressure
    Pm = Pamt = Atmospheric or mouth pressure
    t1 = time range for simulation
    N = number of compartments
    E = elastance
    frc = functional residual capacity
    R = linear resistance
    pw = vapor partial pressure of water
    K1_i,K2_i,K1_e,K2_e = resistance coefficients for inspiration and expiration
    nhf = nasal high flow therapy
```

```
PA = alveolar pressure
'''
NHF = 0
nhf = 0.03*NHF/60 #+ 0.05*(0.08*NHF/60) #(in l/s)
PA = x[0];           #Lung Mech
fo=  x[1];           #Alveolar O2 fraction
fc=  x[2];           # Alveolar CO2 fraction
fdo= x[3:N+3];       #Dead space O2 fraction
fdc= x[N+3:2*N+3]    #Dead space CO2 fraction


#_____________________________________________________________________
#Lung Mechanics
#_____________________________________________________________________
#interpolate pleural pressure derivative
pl = np.interp(t,t1,dPLdt)
Pl_i = np.interp(t,t1,PL)
#Use resistance coefficients to estimate flow
if Pm-PA >=0 :   #If inspiration
   Coef  = [k2_i , k1_i , -(Pm-PA)] # Coefficients of 0 = K1*q +K2*q^(2)-P
   RoOT  = np.roots(Coef)           # Function to determine roots
   cl    = RoOT > 0                 # select index of positive part
   q     = np.select(cl,RoOT)       # select positive flow
else :         #If expiration
   Coef  = [k2_e , k1_e ,  (Pm-PA)]
   RoOT  = np.roots(Coef)
   cl    = RoOT > 0
   q     = -np.select(cl,RoOT)     #select positive flow and negate
```

```
#_____________________________________________________________________
#Gas exchange parameters
#_____________________________________________________________________
Vd = 0.15        #dead space volume
fo_atm =0.21      #atmospheric O2 fraction
fc_atm =0.0004    #atmospheric CO2 fracton
d_Vd = Vd/N       #unit dead space volume

#Metabolic O2 and CO2 rates
coo_met = 0.0033; O2 = 0.005
frc = 2.5
QA1 = q+coo_met-O2
VA  = (PA-(Pl_i+5.4))/E + frc
#_____________________________________________________________________
#Lung Mech ODEs
#_____________________________________________________________________

dPAdt  = QA1*E*(Pm/PA)+ pl   #Ode for alveolar pressure
dFod_dt= np.zeros(N)           #array for ode for dead space O2 fracton
dFcd_dt= np.zeros(N)           #array for ode for dead space CO2 fraction
#_____________________________________________________________________

#***********
#Apnea
#***********
#dt = 0.1
```

```
if 170 <t and t<190:  #(e.g. 10 seconds: )
   q=0
   dPAdt  = 0
   #VA     = frc #At apnea lung volume equals frc
   QA1    = 0         #coo_met-O2


#_____________________________________________________________________
#Gas Exchange ODEs
#_____________________________________________________________________
#Inspiration (Dead space units)
if q >=0 : # Inspiratory condition   #first unit is closest to mouth

   dFod_dt[0]= q*(fo_atm-fdo[0])/d_Vd  #O2 Ode for first dead space unit volume
   dFcd_dt[0]= q*(fc_atm-fdc[0])/d_Vd  #CO2 Ode for first dead space unit volum
   for g in range(1,N):
       if g <= round(0.5*N) :
          dFod_dt[g]= q*(fdo[g-1]-fdo[g])/d_Vd #O2 ode for remaining DS units
          dFcd_dt[g]= q*(fdc[g-1]-fdc[g])/d_Vd #CO2 ode for remaining DS units
       else:
          dFod_dt[g]= q*(fdo[g-1]-fdo[g])/d_Vd #O2 ode for remaining DS units
          dFcd_dt[g]= q*(fdc[g-1]-fdc[g])/d_Vd #CO2 ode for remaining DS units


   #Inspiration (Alveolar unit)
   #===========
   # Alveolar O2 ODE for inspiration
   dFodt= (q*fdo[N-1]-O2-fo*(QA1))/VA
```

```
    # Alveolar CO2 ODE for inspiration
    #-------------------------
    dFcdt= (coo_met + q*fdc[N-1]-fc*(QA1))/VA



    #Expiration (Alveolar units)
    #============
 if q<0: #expiration condition
    q=abs(q)
    q2= q+nhf
     #Alveolar CO2 ODE for expiration
    dFodt= (-O2 +q*fdo[N-1]+fo*(QA1))/VA

    dFcdt= (coo_met -q*fdc[N-1]-fc*(QA1))/VA

   #Expiration (Dead space units)
    dFod_dt[N-1]= (q)*(fo-fdo[N-1])/d_Vd
    dFcd_dt[N-1]= (q)*(fc-fdc[N-1])/d_Vd
    for g in range(N-1,0,-1):

        if g <= round(0.5*N):
           dFod_dt[g-1]= (-nhf*fdo[g-1]+q*(fdo[g]-fdo[g-1]))/d_Vd
           dFcd_dt[g-1]= (-nhf*fdc[g-1]+q*(fdc[g]-fdc[g-1]))/d_Vd
        else:
            dFod_dt[g-1]= (q2)*(fdo[g]-fdo[g-1])/d_Vd
            dFcd_dt[g-1]= (q2)*(fdc[g]-fdc[g-1])/d_Vd
```

```
    #_____________________________________________________________
     #putting ODes together
    #_____________________________________________________________
     OD= np.append([dPAdt,dFodt,dFcdt],dFod_dt)
     ODe_Sys=np.append(OD,dFcd_dt)
     return ODe_Sys  #Return system to solver
    #_____________________________________________________________


#Function to solve ODE - initial conditions defined here
def ODE_SOLVER():

     #Parameters
     Pm    =760              #Atmospheric pressure
     frc   =2.5              #Functional residual capacity
     E     =8;               # Lung elastance
     pw    = 47;             #vapor pressure of water at 37 degrees celsius
     cf    = 0.735            #cmH20 to mmHg
     k1_i  = 3.7*cf;  k2_i = 4.1*cf # Inspiratory Airway resistance coefficients
     k1_e  = 3.5*cf ; k2_e = 2.9*cf # Expiratory airway resistance coefficients
     t1    = np.arange(0,350,0.1)  # time range definition344
     dx    = t1[1]-t1[0]            #time interval

     #_____________________________________________________________________
     #Forcing function (pleural pressure)
     #_____________________________________________________________________
```

```
R     =2;                #airway resistance
w     =2*np.pi/4.3;      #Angular velocity
TV    =0.47;             #tidal volume
E1    =8                 #Elastance
PL_ini = 756.8           # Initial pleural pressure
PL    = PL_ini - R*w*(TV/2)*np.sin(w*t1)-E1*(0.52-(TV/2)*np.cos(w*t1))
#Derivative pleural pressure
dPLdt = np.gradient(PL,dx)



#-----------------------------------------------------------
#Constants and Initial conditions
#-----------------------------------------------------------
N=30 #number of dead space compartments
#initial co2 tension in dead space compartments
fdc_ini =(0.0042-0.0041)*np.random.random_sample((1,N))+0.00042
#initial O2 tension in dead space compartments
fdo_ini =(0.21-0.2)*np.random.random_sample((1,N))+0.21
y1      = np.append([Pm,0.10,0.05263],fdo_ini)
# All initial conditions put in one array
y0      = np.append(y1,fdc_ini)
# all parameters put into one array
Pmts=(PL,dPLdt,Pm,t1,N,E,frc,R,pw,k1_i,k2_i,k1_e,k2_e)



#************************************
#Solve system of ODES using odeint
```

```
sol  = odeint(odefn,y0,t1,args=Pmts)
#************************************



#_____________________________________________________________________
#RESULTS AND PLOTTING
#_____________________________________________________________________
# Extract alveolar pressure
palv = sol[:,0]
F    = np.zeros(len(palv))
tV   = np.zeros(len(palv))
Pmus = np.zeros(len(palv))
VA   = (palv-(PL+5.4))/E
Pmus = -PL+PL_ini

#Extract alveolar gas quantities
fo_alv      = sol[:,1] # Extract alveolar O2 fraction
fc_alv      = sol[:,2] # Extract alveolar CO2 fraction
PAO2    = fo_alv*(palv-pw) # Calculate alv. O2 partial pressure
PACO2   = fc_alv*(palv-pw) # Calculate alv. CO2 partial pressure

#Recomputing flow and volume as it was not returned by ODE solve
for d in range(1,len(palv)):
    if Pm-palv[d]>0 :
       Coef  = [k2_i , k1_i , -(Pm-palv[d])]
       RoOT  = np.roots(Coef)
       cl    = RoOT > 0
```

```
        q     = np.select(cl,RoOT)
        F[d]  = np.float(q)
        tV[d] = q*dx +tV[d-1]

    else :
        Coef  = [k2_e , k1_e ,  (Pm-palv[d])]
        RoOT  = np.roots(Coef)
        cl    = RoOT > 0
        q     = np.select(cl,RoOT)
        F[d]  = -np.float(q)
        tV[d] = -q*dx +tV[d-1]



#**************************************
#Figure and Plots
#**************************************
# matplotlib qt # display plots in separate Window

 t=t1 # assigning t1 to t
 plt.close('all')

 r1 = 1463; r2= 1507
 #Lung mechanics

 plt.figure(1)

 plt.subplot(1,2,1)
```

```
plt.plot(t[r1:r2],PL[r1:r2]-760,'k-')
plt.title('Forcing function (Pleural Pressure)',fontsize=16)
plt.xlabel('Time, seconds',fontsize=14)
plt.ylabel('Pressure, cmH$_2$O',fontsize=14)
plt.subplot(1,2,2)
plt.plot(t[r1:r2],palv[r1:r2]-760,'k-')
plt.title('Alveolar pressure',fontsize=16)
plt.xlabel('Time, seconds', fontsize=14)
plt.ylabel('Pressure, cmH$_2$O',fontsize=14)

# O2 plots
plt.figure(2)
plt.subplot(1,3,1)
plt.plot(t[r1:r2],F[r1:r2],'k-')
plt.title('Breathing flow',fontsize=16)
plt.xlabel('Time, seconds',fontsize=14)
plt.ylabel('Flow, L/s',fontsize=14)
plt.subplot(1,3,2)
plt.plot(t[r1:r2],VA[r1:r2],'k-')
plt.title('Tidal volume',fontsize=16)
plt.xlabel('Time, seconds', fontsize=14)
plt.ylabel('Volume, L',fontsize=14)
plt.subplot(1,3,3)
plt.plot(VA[r1:r2],Pmus[r1:r2],'k-')
plt.title('Pressure-volume loop',fontsize=16)
plt.xlabel('Volume, L', fontsize=14)
plt.ylabel('Pressure, cmH$_2$O',fontsize=14)
```

```
 #CO2 plots
plt.figure(3)
plt.subplot(1,3,1)
plt.plot(t,PAO2)
plt.ylim(0,160)
plt.title('Alveolar O$_2$ tension',fontsize=16)
plt.xlabel('Time, seconds', fontsize=14)
plt.ylabel('Alveolar O$_2$ tension, mmHg',fontsize=14)
plt.subplot(1,3,2)
plt.plot(t,(760-pw)*sol[:,2+ round(N/2)])
plt.ylim(0,200)
plt.title('Tracheal O$_2$ tension ',fontsize=16)
plt.xlabel('Time, seconds', fontsize=14)
plt.ylabel('Tracheal O$_2$ tension, mmHg',fontsize=14)
plt.subplot(1,3,3)
plt.plot(t,(760-pw)*sol[:,3])
plt.ylim(0,200)
plt.title('Nasal O$_2$ tension',fontsize=16)
plt.xlabel('Time, seconds', fontsize=14)
plt.ylabel('Nasal O$_2$ tension, mmHg',fontsize=14)


# CO2 plots


plt.figure(4)
```

```
    plt.subplot(1,2,1)
    plt.plot(t,PACO2)
    plt.ylim(0,80)
    plt.title('Alveolar CO$_2$ tension',fontsize=16)
    plt.xlabel('Time, seconds', fontsize=14)
    plt.ylabel('Alveolar CO$_2$ tension, mmHg',fontsize=14)
    plt.subplot(1,2,2)
    trach= (760-pw)*sol[:,2 +2*N -round(N/2)]
    cmax = np.max(trach)
    print(cmax)
    plt.plot(trach)
    plt.ylim(0,80)
    plt.title('Tracheal CO$_2$ tension',fontsize=16)
    plt.xlabel('Time, seconds', fontsize=14)
    plt.ylabel('Tracheal CO$_2$ tension, mmHg',fontsize=14)

    trach2= (760-pw)*sol[:,2+2*N -round(N/2)]
    a=(100/760)*trach2[1430:1483]

    a= np.transpose(a)
    a.tofile('mesh.csv',sep='\n',format='%10.5f')




ODE_SOLVER()
```